Charting the Unknown: A Hunt in the Dark

By

Gopolang Mokoka Mohlabeng

Submitted to the graduate degree program in Physics and Astronomy and the Graduate Faculty of the University of Kansas in partial fulfillment of the requirements for the degree of

Doctor of Philosophy

(Chairperson) Kyoungchul Kong

David Z. Besson

David E. Lerner

Douglas McKay

John P. Ralston

Graham W. Wilson

Date Defended: 25th of April 2017

The Dissertation Committee for **Gopolang Mokoka Mohlabeng**
certifies that this is the approved version of the following dissertation:

Charting the Unknown: A Hunt in the Dark

Chairperson Kyoungchul Kong

Date Approved: 25th of April 2017

Abstract

Astrophysical and cosmological observations have pointed strongly to the existence of dark matter in the Universe, yet its nature remains elusive. It may be hidden in a vast unknown parameter space in which exhaustively searching for a signal is not feasible. We are, therefore, compelled to consider a robust program based on a wide range of new theoretical ideas and complementary strategies for detection. The aim of this dissertation is to investigate the phenomenology of diverse dark sectors with the objective of understanding and characterizing dark matter. We do so by exploring dark matter phenomenology under three main frameworks of study: (I) the model dependent approach, (II) model independent approach and (III) considering simplified models. In each framework we focus on unexplored and well motivated dark matter scenarios as well as their prospects of detection at current and future experiments. First, we concentrate on the model dependent method where we consider minimal dark matter in the form of mixed fermionic stable states in a gauge extension of the standard model. In particular, we incorporate the fermion mixings governed by gauge invariant interactions with the heavier degrees of freedom. We find that the manner of mixing has an impact on the detectability of the dark matter at experiments. Pursuing this model dependent direction, we explore a space-time extension of the standard model which houses a vector dark matter candidate. We incorporate boundary terms arising from the topology of the model and find that these control the way dark matter may interact with baryonic matter. Next we investigate the model independent approach in which we examine a non-minimal dark sector in the form of boosted dark matter. In this study, we consider an effective field theory involving two stable fermionic states. We probe the sensitivity of this type of dark matter coming from the galactic center and the center of the Sun, and investigate its detection prospects at current and future large volume experiments. Finally, we explore an intermediate approach in the form of a simplified model. Here we

analyze a different non-minimal dark sector in which its interactions with the standard model sector are mediated primarily by the Higgs Boson. We discuss for the first time a vector and fermion dark matter preserved under the same stabilization symmetry. We find that the presence of both species in the early Universe results in rare processes contributing to the dark matter relic abundance. We conclude that connecting these three frameworks under one main dark matter program, instead of concentrating on them individually, could help us understand what we are missing, and may assist us to produce ground breaking ideas which lead to the discovery of a signal in the near future.

I would like to dedicate this dissertation to my mother, Mamotlou Maggie Mohlabeng.

Acknowledgements

I would first like to extend my deepest gratitude to my thesis advisor KC Kong. Without his guidance and belief in me, none of this work would be possible. Since my first year at KU, KC has believed that I have the ability to do good work, even when I didn't believe it myself. I am very thankful for all the work he has exposed me to and all the opportunities he has afforded me. I am thankful for the summer schools (national and international), all the conferences and workshops he has sent me to. Furthermore I am grateful for his support and encouragement, throughout my PhD and at present. KC, it really has been a pleasure and honor working with you and I have no further words to express my gratitude.

The second person I would like to extend my deepest gratitude to is John Ralston. The knowledge I have today and the confidence with which I carry out my research is due in no small part to him. I first started doing research with John and learned many aspects, which I still use till this day. His belief and patience in me, even when I didn't know much about about the subject, allowed me to learn at my own pace and do the best I could. John, thank you very much, no words can express my thanks.

I would also like to thank the rest of my PhD committee members for taking their time and being on my committee. I would like to also thank colleagues and friends in the department who contributed to a very enriching environment where we bounced ideas and discussed much physics, particularly Steven Prohyra. Furthemore, I thank everyone in the department who made my time at KU very enjoyable, particularly Kristin Rennels for helping me deal with the seemingly endless administrative problems throughout the years.

I would further like to thank Fermilab for the funding and opportunity to work with researchers at

the lab. While at fermilab, I was exposed to many different aspects of particle physics and I learned a lot. It was definitely a once in a lifetime experience. I would like to give much thanks to Paddy Fox, for all his advise and encouragement. I would like to thank Dan Hooper for all the new research he exposed me to. I would like to thank my office mates and friends in the Theory group at fermilab, who I learned tremendously from and who always encouraged physics talks during coffee time. I am also grateful for having had many excellent collaborators, including Paddy Fox, Dan Hooper, Asher Berlin, Anthony DiFranzo, Jong-Chul Park, Seongchan Park, Tom Flacke, Dong Woo Kang, Mihailo Backovic and Haider Alhazmi among many others who I worked with in other studies.

In my native language, we have a saying, "One who eats last is King". I would like to express my gratitude to Inna Stepaniuk who gave me love and support during the most stressful parts of my studies. Last, but most definitely not least I would like to thank my mother in South Africa for allowing me to follow my dreams, even if it meant I would be far from her. Without her, I would not be where I am today.

This work was supported by the National Research Foundation of South Africa, Grant No. 88614, by the dissertation fellowship at the University of Kansas and by the Fermilab Graduate Research Fellowship in Theoretical Physics.

Contents

List of Figures

List of Tables

Chapter 1

Introduction

The Standard Model (SM) of particle physics has been perhaps one of the best triumphs of modern physics. It has been outstanding in accurately explaining much of the microscopic phenomena observed to date. It is a fundamental theory of elementary particles and their interactions, and is mathematically described as a quantum field theory based on the gauge group $SU(3)_c \times SU(2)_W \times U(1)_Y$. Recently the Large Hadron Collider (LHC) observed a scalar particle resembling the Higgs Boson of the SM. The discovery of the Higgs would imply that the classification of elementary particles in the SM is now complete. However, theoretical and experimental motivations point to the SM not being the most fundamental theory of nature, but rather a low energy effective field theory that is borne of an underlying fundamental quantum field theory. These observations point to unexplained fundamental questions which seem to lie beyond our realm of understanding. Thus as a step to obtaining the full picture of nature, we must consider new physics beyond the SM (BSM). One of the most significant and intriguing issues which cannot be accommodated in the SM and serves as a huge motivation for new physics beyond the SM is the question of Dark Matter (DM). The existence of DM has been unambiguously established by multiple measurements at astrophysical and cosmological scales, yet we remain clueless to what it is. The goal of this dissertation is to explore the phenomenology of dark matter. There is a large number of possible DM scenarios and it is not feasible to investigate each one. Therefore, we consider three main frameworks of study and in each, we focus on well motivated models which provide

new DM prospects. We note that instead of focussing on one particular framework of study, we might be better served by connecting all three under a larger program of DM phenomenology. First we will introduce DM and discuss its evidence, possible nature and methods of detection.

1.1 Evidence of Dark Matter

On cosmological scales, DM has been inferred with the help of temperature and polarization anisotropies in the cosmic microwave background (CMB) radiation as well as studies of baryon acoustic oscillations and type 1a supernovae. This gives us information on the DM relic density, i.e. how much DM is left after it decoupled in the early universe [1, 2]. Observations of the baryon density and amplitudes of the temperature fluctuations in the CMB illustrate that different structure formation would have occurred in a purely baryonic universe that does not contain DM. This is further corroborated by simulations that incorporate dark matter and can reproduce the large scale structure we see today, as opposed to purely baryonic models which cannot [3].

Further evidence is obtained on galaxy cluster scales. In the early 1930s, astrophysicist Fritz Zwicky was studying the radial velocities of galaxies inside the Coma Cluster of galaxies and concluded that there was matter unaccounted for. He found that the orbital velocities of the galaxies in the Coma cluster were much larger than their expected value as estimated from the Virial theorem [1, 2]. He then realized that there must be a large amount of non-luminous matter acting as a sort of "cosmic glue" holding the cluster together.

Similarly, further studies were done of different galaxy clusters, where evidence for DM was ascertained through gravitational lensing and from studying the intra cluster gas through thermal X-ray emissions. Gravitational lensing is a process whereby light from background objects is bent around a foreground gravitating mass. One particular example of a system in which lensing was used is the Bullet Cluster of galaxies, illustrated in Fig. 1.1. The Bullet Cluster is a massive system consisting of a main cluster intersected by another smaller cluster. Lensing of the background stars and galaxies led to the mapping of the gravitational potential where two separate regions nearer to the visible galaxies appeared to be strongest. This is a strong indication of non-baryonic matter acting as a gravitational lens

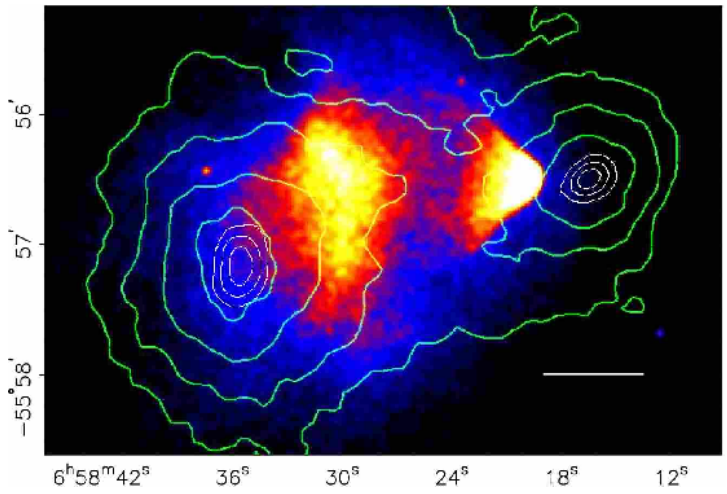

Fig. 1.1 A Chandra image of the Bullet cluster of galaxies. The overlaid green contours indicate the gravitational potential map inferred from weak gravitational lensing. The white contours indicate errors on the center of the gravitational lens (dark matter halo) at 68.3%, 95.5% and 99.7% confidence levels. Figure obtained from Refs. [4, 5].

for the background objects [2, 3, 6]. Moreover, through measurements of the temperatures of the X-ray gas (the main baryonic mass component in a cluster) in the Bullet Cluster, the mass of the baryonic material was mapped out. This is an indication of how much baryonic matter is contained in the cluster as well as how much of the non-baryonic component exists. Studies of this type were extended to many more galaxy clusters, and it was found that DM contributes roughly 85%, the intra cluster medium contributes roughly 14% and stars and galaxies only roughly 3% of the total mass of a galaxy cluster [2].

More convincing evidence of DM can be found on galactic scales. Astrophysicist Vera Rubin was able to deduce the existence of DM by studying the rotational velocities of galaxies. The types of galaxies around which DM halos are mainly found include spirals, ellipticals and dwarf spheroidals. Spiral galaxies are gravitationally bound systems in which luminous matter rotates around the galactic center on nearly circular orbits. The rotational velocities of spirals can be traced out by using optical ($H\alpha$) emissions or the 21 cm emission line from neutral Hydrogen or HI gas emissions. The simplest way to measure the gravitational effect in a spiral galaxy is in the application of Kepler's 3rd law which

leads to

$$v_r = \sqrt{\frac{G\,M(r)}{r}}. \tag{1.1}$$

Here v_r is the rotational velocity of the galaxy and G is the gravitational constant $6.67 \times 10^{-11} m^3 kg^{-1} s^{-2}$. The quantity $M(r) \equiv 4\pi \int \rho(r)\, r^2\, dr$ is the total mass enclosed in radius r and $\rho(r)$ is the mass density profile of a galactic halo [1, 3, 7]. This method of observation was applied to distances beyond which the luminous matter from the galaxy ceases and observers found that M(r) continued to increase, causing v_r to remain roughly constant. They found that if the luminous matter accounted for the total matter in the galaxy then v_r would decrease as $r^{-1/2}$ beyond the stage where M(r) is cut off. Since this additional mass adding to M(r) was not visible as there was no radiation associated with it, it was labelled "dark". Numerous galaxy rotation curves have shown this type of behavior and a particular example is illustrated in Fig. 1.2. This near constant behavior of v_r implies that there exists a dark matter halo with $M(r) \propto r$ having a spherical matter distribution with $\rho(r) \propto r^{-2}$ [3, 7]. Hence, rotational curve measurements imply that most spiral galaxies are surrounded by a DM halo, which contributes to the bulk of the mass of the galaxy. In fact, it has been suggested that without the support of a DM halo, spiral galaxies would self gravitate leading to bar instability and collapse [2, 3, 6].

DM in elliptical galaxies has been inferred by isolating the rotational velocities of the bright planetary nebulae, which are clearly distinguishable from the rest of the matter. Dwarf spheroidals are smaller and less luminous than the spirals and ellipticals. Studies of these types of galaxies have revealed that their mass density is dominated by DM. In fact, they have similar luminosities and velocity dispersions to globular clusters, however, they are much larger and have a much larger mass to light ratio indicating they are most likely DM dominated [9, 10]. Further evidence of DM on galactic scales was found in low surface brightness galaxies [6], lenticular galaxies [11] and binary galaxy systems. [12, 13].

1.2 Possible Nature of Dark Matter

The large amount of astrophysical evidence points to DM constituting roughly 80% of the matter density in the Universe. All evidence of its existence are based on its gravitational interactions with baryonic

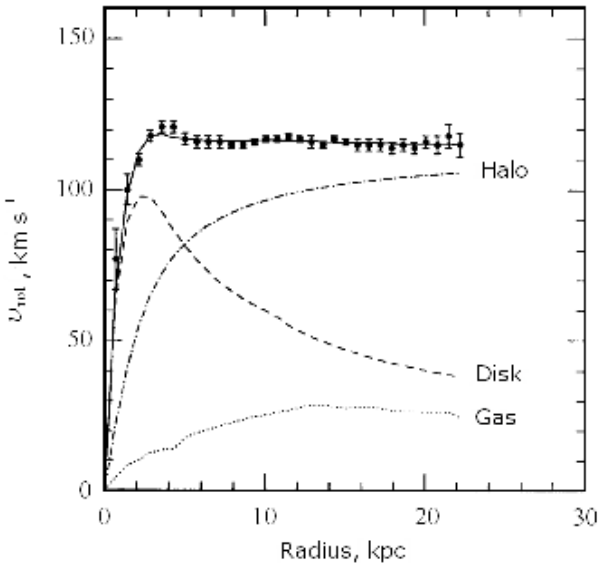

Fig. 1.2 Rotational velocity curve of the spiral galaxy NGC 6503. The dotted line is the matter contribution from the galactic gas, the dashed line is the contribution from matter in the galactic disk, mostly stars, the dot-dashed line represents the contribution from the DM halo alone. The data is obtained from Ref. [8] and the figure is from Ref. [7].

matter, indicating it must have mass. There is no evidence indicating that DM can absorb or emit any form of radiation, implying that DM must be neutral. Furthermore, measurements of the CMB, results from weak microlensing as well as the structure formation in the current Universe indicate that it's very unlikely that dark matter could be baryonic in nature. In fact, simulations of large scale structure indicate that it must be cold, i.e. non-relativistic in nature. These are some of the macroscopic properties we have been able to learn about DM so far, yet its microstructure remains a mystery. If DM is a particle, we don't know at which mass scale it lies, what its spin is, or whether it's a fundamental or composite particle. The community has constructed a myriad of possible models which can describe what DM may be made of. This section is dedicated to a discussion of the possible nature of dark matter, but we will first briefly discuss the various production mechanisms of DM in an effort to understand its possible composition.

For many years, the most favored DM candidates were those produced thermally and had masses in and around the electroweak scale ($\sim$ 10 GeV - 1 TeV). These candidates are known as weakly interacting massive particles (WIMPs) [2, 6, 14]. In the thermal production scenario, a base assumption is that in the early Universe WIMPs were produced in collisions between particles of the thermal plasma when the Universe was radiation dominated. At temperatures in the plasma much higher than the DM mass ($T > M_\chi$ [1]) the colliding SM particles in the plasma had enough energy to efficiently produce WIMP pairs. Likewise, DM particles could equally annihilate to produce SM particles, so the reactions were in equilibrium. As the Universe expanded, the temperature of the thermal bath became smaller than the DM mass. This marked a decrease in the number density of the particles involved, which meant that the SM particles could no longer produce DM due to the decrease in energy and pressure. It also meant that the annihilation rate of WIMPs decreased to a point where it was below the rate of expansion of the Universe, at which point the DM chemically froze out. Beyond this stage the number of WIMP particles in a comoving volume remained constant. This number density is referred to as the relic density [3, 6, 14]. The relic density of DM can be obtained by solving a first order differential equation known as the Boltzmann equation

$$\frac{dn_\chi}{dt} = -3Hn_\chi - \langle\sigma v\rangle(n_\chi^2 - n_{eq}^2). \tag{1.2}$$

Here n_χ is the number density of dark matter, t is the time of evolution of the DM, H is the Hubble rate of expansion, $\langle\sigma v\rangle$ is the annihilation cross-section multiplied by the velocity of the WIMPs, all averaged over the WIMP velocity. The quantity n_{eq} is the number density of the DM particles which was in thermal equilibrium with the SM particles in the thermal bath. The relic density, which is the number density of DM at freeze out [2] can be determined by solving Eq. 1.2. A rough approximation gives

$$n_f \sim (m_\chi T_f)^{3/2} e^{-m_\chi/T_f}. \tag{1.3}$$

[1] Here χ represents the dark matter particle.

[2] Freeze-out is defined as the time when the annihilation rate of DM is the same as the rate of expansion of the universe, i.e. $\Gamma_A \equiv n\langle\sigma v\rangle = H$

The quantity n_f is the number density at freeze-out, m_χ is the dark matter mass and T_f is the freeze-out temperature. It is customary to express the number density of DM in terms of the comoving number density $Y \equiv \frac{n_\chi}{s}$, with s being the entropy density of the Universe. Defining variable $x \equiv m_\chi/T$, where T is the temperature of the photons, Eq. 1.2 in terms of the comoving number density is

$$\frac{dY}{dx} = -\frac{\langle\sigma v\rangle s}{Hx}(Y^2 - Y_{eq}^2). \tag{1.4}$$

The quantity $Y_{eq} \equiv n_{eq}/s$ is the equilibrium comoving number density. The numerical solution of Eq. 1.4 is illustrated in Fig. 1.3. The solid line represents the equilibrium number density as the Universe expands, while the dashed lines illustrate the different rates of freeze-out as a function of the thermally averaged annihilation cross-section. An increase in the thermally averaged annihilation cross-section indicates a large annihilation rate of DM into SM particles and lowers the number density of DM at the time of freeze-out.

The WIMP relic density can, finally, be expressed in terms of the DM mass density $\rho_\chi = m_\chi n_\chi$ and the critical density of the Universe ρ_c, which is determined from the Friedmann equation following the derivation in Refs. [3, 6, 15]. The relic density is, therefore, approximated as

$$\Omega_\chi h^2 = \frac{\rho_\chi h^2}{\rho_c} \approx \frac{1.07 \times 10^9 GeV^{-1}}{M_{Pl}} \frac{x_f}{\sqrt{g_*}} \frac{1}{a + 3b/x_f}. \tag{1.5}$$

Here $M_{Pl} = 1.22 \times 10^{19} GeV$ is the planck mass, $x_f \equiv m_\chi/T_f$ is defined as the freeze-out temperature and g_* is the internal degrees of freedom quantifying the energy density as well as the entropy density of the Universe [15]. The present DM relic density, Eq. 1.5 can be approximated to first order as

$$\Omega_\chi h^2 \approx \frac{3 \times 10^{-27} cm^3 s^{-1}}{\langle\sigma v\rangle}. \tag{1.6}$$

For masses in the electroweak scale and weak cross-sections, Eq. 1.6 gives the right order of magnitude for the DM density as observed in experiment ($\Omega_\chi h^2 = 0.12 \pm 0.0012$) [16]. It should be noted that

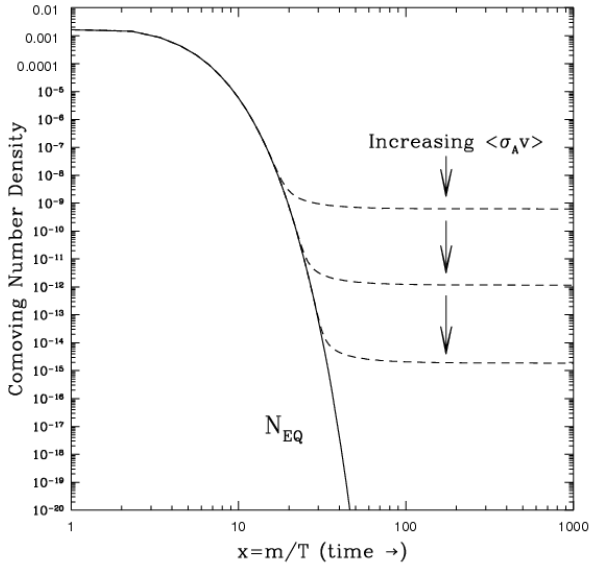

Fig. 1.3 A plot of the comoving number density Y of a thermal relic dark matter as it evolves in the early universe, with $\langle \sigma_A v \rangle = \langle \sigma v \rangle$. The figure is from Ref. [18].

this approximation though it works, is a ball park argument and can be dramatically changed in more intricate models where coannihilations, resonance effects or mass threshold effects become significant [17].

The thermal production mechanism is not the only way to create dark matter. An alternative method for production is one in which dark matter is produced non-thermally. Here, DM may be produced from one of two processes. It can be formed from the decay of some heavier dark sector state or gravitationally in the early universe, i.e., at the end of inflation [15, 19].

Other mechanisms of DM production can arise in non-standard cosmological models where the thermal evolution of the Universe may be slightly altered. As a result the dark matter relic density and speed before structure formation would also be impacted. This can result in the formation of smaller DM structures where DM particles give signals that differ drastically from the signatures expected from DM in the standard cosmology. These types of mechanisms can be obtained for example from low temperature reheating models [20, 21].

The most preferred candidate of DM has been by far the WIMP, since through its production mechanism we are able to naturally satisfy the observed value of the DM relic abundance. There are many BSM theories which incorporate DM, while explaining other fundamental problems not addressed by the SM. Supersymmetry (SUSY) [22] has been the most popular of these BSM scenarios for many decades. The Minimal Supersymmetric extension of the Standard Model (MSSM) has been one of the most prominent theories in the search for DM. Here the DM candidate is the lightest SUSY particle, or LSP known as the Neutralino [23]. It is stabilized by a symmetry known as R-Parity and its mass is of order 10 - 1000 GeV. It is theorized to be produced thermally, making it the perfect WIMP candidate. In SUSY there can be further variations or extensions of the MSSM in which there are other DM candidates, such as the gravitino or axino. These particles would be very light, in orders of few to hundred keV and can be produced non-thermally [24, 25]. Likewise, another set of models which have been widely considered and harbor possible DM candidates are models with extra spatial dimensions. Perhaps the most discussed of these in the literature, in terms of DM, have been models of universal extra dimensions (UED). The DM candidate here is the lightest Kaluza-Klein particle (LKP). When the SM is extended by one extra spatial dimension, the LKP is known as the Kaluza-Klein (KK) photon [26–28]. The LKP is stabilized by a symmetry which emerges from the geometry of the model and is known as KK parity. The mass of KK dark matter is of order 1 TeV. In models with two extra spatial dimensions, the LKP is a particle called the Spinless photon [29, 30].

Many other models have been of interest. In recent years, particular attention has been paid to simple extensions of the SM in which the dark sector and the SM are connected through the kinetic mixing of dark gauge bosons with the SM gauge bosons [31]. These have been very well motivated as they allow for a low mass dark photon which can explain some of the experimental anomalies seen in precision measurements such as the proton radius puzzle and the muon g-2 discrepancy. Other scenarios have emerged in the form of Higgs portals. These are scenarios in which dark matter interacts with the SM primarily through the Higgs boson. In these types of model we not only explore the DM phenomenology, but also obtain an insight to how the Higgs might interact with the dark sector. Other possible candidates include axions [32] and sterile neutrinos [33] which would be produced non-thermally in

the early universe. The scenarios discussed above assume that dark matter is a fundamental particle, yet it may be possible that dark matter is, instead, composite [34]. We further note that the scenarios discussed above need not be mutually exclusive. In principle the different models may overlap, resulting in two or more stable states contributing to the total DM relic abundance of the Universe. These types of intricate models constitute multi-component dark matter and their phenomenology has been given much attention in recent years. They have been explored at particle physics levels [35–42] and in astrophysics as a solution to the small scale structure problems [43]. Knowing what the possible nature of DM is gives us an idea on how to search for it. The treatment of DM as a particle has provided the particle physics community with various strategies for its detection.

1.3 Dark Matter Detection

The possible particle nature of dark matter provides strong implications for its detection. In principle there are four pillars on which dark matter detection is based:

- Astrophysical signatures
- Indirect detection
- Direct detection
- Collider signatures

Astrophysical signatures, discussed above, are essential because this is how we know DM exists. The relic density sets precedence as it provides information on the amount of DM in the current Universe. Thus it is the first constraint considered when studying a particular DM species. Models in which annihilation into the SM does not occur efficiently in the early Universe will produce too much DM. This shows up in the determination of the relic abundance, when the theoretical quantity is larger than the value observed. DM in such models is said to over-close the Universe. On the contrary, one can have too much annihilation such that by the time of freeze-out, there is very little dark matter left. The relic abundance here is much smaller than the observed value leaving room to consider another DM species

to fill up the DM abundance. Such scenarios form the basis of the multicomponent DM hypothesis. In all models where the DM species is assumed to form 100% of the DM density in the current Universe, the value of the relic abundance must match the observed value. This is the most important constraint for each of the models considered. The relic abundance constraint doesn't give us any information about the actual microscopic nature of DM, it just tells us how much DM there is. Fortunately, the other three methods have the ability to help us discern the composition of DM.

Firstly, the method of DM indirect detection is based on the idea that if DM annihilated in the early universe before decoupling, then it must also annihilate at present times through the process $\chi\chi \to SMSM$. There is a large spectrum of SM final states to consider. For example, DM can annihilate to mono-energetic photons (a process that is loop induced) resulting in a striking signal in gamma-ray telescopes. Alternatively, it can annihilate to other SM particles which upon decaying can result in a smooth, defuse distribution in the gamma-ray spectrum. Photons from DM annihilation may also produce signals at other energies such as in X-rays, which are typically at lower energies than gamma-rays implying that the mass of the annihilating DM particles must be lower. A further mode of annihilation is into electrons and positrons. A number of experiments have observed an excess in their measured positron fraction and an appealing explanation for this is DM annihilations [14, 44]. What's more, electrons and positrons from DM annihilations can radiate synchrotron photons in the presence of a strong magnetic field, and the radiation can be detected at radio telescopes.

A particularly interesting channel of annihilation is into neutrinos. Signatures of these may be seen from sources as close as the Sun. If DM is captured in the core of the Sun, it can annihilate into neutrinos which, unlike their SM counterparts, are very weakly interacting and are able to escape the Sun without much interaction. The neutrinos can then travel to the Earth where they can be detected using very large experiments. In these detectors a neutrino can scatter off an electron leaving a Cherenkov radiation signal. This can be observed in experiments such as Super-Kamiokande (SK) and Hyper-Kamiokande (HK). These solar neutrinos from DM annihilations can also scatter off of electrons or protons leaving discernible tracks in liquid argon type detectors such as the Deep Underground Neutrino Experiment

(DUNE). A further method of detection is to scatter in ice producing radiation that can be detected by very large experiments such as IceCube, which is imbedded in the ice and is sensitive to these signals [14].

The second method is the direct detection of DM. The astrophysical evidence pointing to our galaxy being surrounded by a dark matter halo allows us to look for dark matter directly on the Earth. Through the process $\chi SM \rightarrow \chi SM$, we can look for galactic DM scattering with nuclei in underground laboratories. As the solar system moves through the galaxy, the Earth (in its frame of reference) is struck by a DM "wind". These DM particles can then reach an experiment deep underground [1] and scatter off a nucleus, causing it to recoil. We can measure the recoil energy of this nucleus and kinematically determine the properties of the initial particle.

To date no direct detection experiment has observed a convincing DM signature. They continue to set very competitive limits as they gather more data. Many experiments have been running so far, including DAMA/LIBRA, XENON 10, XENON 100 and CDMS among many others [45]. The most competitive limits in the spin-independent (SI) analyses have come from the LUX collaboration [46] followed by the PandaX team [47]. In the spin dependent (SD) analysis, the most competitive limits have so far been set by the PICO collaboration [48]. As more and more experiments continue to set limits with smaller and smaller cross-sections, SI DM-nucleon cross-sections start to reach an area of the parameter space swamped by coherent neutrino-nucleon interactions. At this point, it will become difficult to distinguish a DM signal from that of neutrinos [49]. If we continue to not find a clear signal for DM, new methods of detection would be necessary. In the late 80's the method of directional dark matter detection was proposed by D. Spergel [50]. This method takes advantage of the motion of the solar system around the galactic center. In fact, directional detection shares the same concept as direct detection, where the recoil energy of a nucleus is measured after scattering with a DM particle. However, in directional detection experiments, the angle of recoil is also taken into account. If this angle is measured it will provide a lot of information about the direction from which the DM particle is

[1] The experiments are placed deep underground to get rid of very large seasonal backgrounds.

coming. Additionally, the recoil angle may also be correlated with the velocity distribution of DM in our galaxy, a quantity that carries much uncertainty. Therefore, it seems highly plausible that information on the recoil angle may provide us further information on the behavior of DM in our galaxy. There are also some studies which suggest that directional detection could discern DM in the region of coherent neutrino-nucleus scattering [51].

The absence of a DM direct detection signal not only gives us more general information about DM, but also helps us improve our detectors and search strategies for conducting better searches in the future.

Finally, DM production at particle colliders is based on the idea that we are working in a controlled environment. At high enough energies, we can produce DM from the following reaction $SMSM \rightarrow \chi\chi$. The current running accelerator is the LHC which collides protons at center of mass energy $\sqrt{s} = 13$ TeV. DM particles produced in a collider would themselves not generate any signal, but only register as missing transverse energy $\not{E}_T$. Though a collider is a controlled environment, the detection of DM is still challenging. DM at colliders may be produced directly or indirectly. The former involves the produced DM accompanying some radiation, which could be a photon or jet depending on the type of collider. For instance, at a proton collider the signal would look like a jet plus missing momentum while in an electron-positron collider it would show up as a photon plus missing momentum. This type of production, however, is fraught with backgrounds, making it hard to distinguish a clear DM signal. The latter involves producing some heavy dark sector state which cascade decays into SM and DM. This may be the best way to produce DM at colliders as it suffers less from backgrounds, though the interpretation of the data is quite challenging.

Utilizing each detection strategy individually may not be the best plan of action in the search for DM. Each method has advantages and disadvantages, implying that the best method of search is to combine all three methods in a complementary manner.

1.4 Outline

A basic requirement for finding dark matter is knowing where to look. It is crucial to consider all aspects that have the potential to provide important information on DM. Yet, the large amount of possible DM candidates and the unknown mass scale at which it might lie make studying it a challenging prospect. It is impossible to perform exhaustive dedicated searches on the entire model space in which there are varying degrees of complexity. Therefore, we need to consider new approaches of investigation through which we utilize all the tools available at our disposal. The effectiveness of our DM searches might be addressed by combining frameworks of study with the most experimentally and theoretically motivated DM scenarios, especially those with the ability to provide unusually distinct signatures in our experiments. With the lack of a distinct signal at experiments, we are limited to either ruling out or highlighting parts of the parameter space, essentially pointing out the characteristics that DM cannot have.

The primary goal of this dissertation is to explore the frameworks through which we can study dark matter. The main purpose of this is to attempt to understand and characterize its properties without having to perform exhaustive searches in the seemingly infinite parameter space. We utilize the results from experiments to set bounds on the DM models in each framework we consider.

Firstly, we consider the top-down or model dependent framework. In this scheme, models are typically constructed to address a fundamental question not answered in the SM while containing a mechanism that produces stable or semi-stable DM particles. In such scenarios other degrees of freedom are taken into account and frequently the bounds on the possible behavior of the DM are set based on some critical assumptions. Secondly, we focus on bottom-up or model independent approaches in which theories are constructed for the purpose of addressing the data or specific instances where a distinct signal may arise. An example is DM effective field theories. These are generally non-renormalizable theories where the cutoff scale of the theory is unknown. Fortunately few assumptions enter here. However, the behavior of the DM is usually generic and it is typically difficult to gain insight on the underlying theory as well as the scale at which the DM might lie. Finally, we investigate a “middle ground”, arising in the form of simplified models. This scheme commonly involves a simple extension of the SM in which

other degrees of freedom which do not contribute to the DM phenomenology are typically ignored, allowing for a minimal way in which to study DM.

In this dissertation, we will study various DM scenarios based on the frameworks discussed above. Of course we cannot consider all possible dark matter models available in these frameworks. Therefore, in each framework we explore strongly theoretically and experimentally motivated examples. We find that these provide not only great phenomenological prospects for studying DM, but also opportunities for characterizing DM using complementary search strategies.

On the model dependent front, extensions of the SM may be completed in various ways: extending the gauge symmetry, the space-time symmetry or the flavor symmetry, among others. Each direction is very well motivated and may harbor rich phenomenology. For purposes of this dissertation, we only consider gauge and spacetime extensions, which are presented in Chapters 2 and 3 respectively. In Chapter 2, we consider a Left-right (LR) extension of the SM, based on Ref. [52]. Here the SM gauge symmetry is extended to $SU(3)_c \times SU(2)_L \times SU(2)_R \times U(1)_{B-L}$. The theoretical motivation of these models was originally to understand parity violation in the SM, i.e. the idea that the SM contains only left handed and no right handed fermion doublets. The attractiveness of LR models was further extended to solving the CP violation problem in the strong sector and to explaining the masses of SM neutrinos. The latter comes from the fact that heavy right handed neutrinos naturally arise in LR models. Furthermore, the existence of a remnant global symmetry which arises in the breaking of the $SU(2)_R \times U(1)_{B-L}$ ensures the stability of a DM candidate. The results of previously studied DM cases in this model motivated us to investigate DM which naturally arises in the form of various mixed fermionic states. These multiplets interact with the extended gauge and Higgs sector in a renormalizable and gauge invariant manner. We found that our models showed certain advantages over the pure multiplet states considered before, especially in terms of the relic abundance and direct detection searches. Additionally, we allow for heavy gauge bosons to decay into the dark sector such that there is a unification of the left and right gauge couplings.

In Chapter 3, we investigate an alternative extension of the SM, i.e. extending the space-time sym-

metry. This results in a completely new theoretical direction which comes with its own phenomenology. A well known example of a space-time extension of the SM is supersymmetry. In this dissertation we will limit our scope to non-supersymmetric extensions of the SM. We explore instead models with extra spatial dimensions. In these types of scenarios, the usual (3+1)-dimensional space-time is extended to include additional dimensions. They are very well motivated for new physics beyond the SM and were introduced as a way to understand the gauge hierarchy problem[53, 54]. Here we focus on flat or "universal" extra dimensions (UED) which incorporate only one extra dimension where the SM particles are allowed to propagate. DM in the context of minimal UED has been extensively studied in the literature. Therefore, in Chapter 3, we consider a next to minimal UED (based on Ref. [55]) where we introduce boundary terms in the electroweak gauge boson sector. Inclusion of the boundary terms affords us a unique opportunity to utilize various methods to study the manner in which DM may behave in this model. We, therefore, explore the DM phenomenology at direct detection experiments and take into account resonance searches as well as precision electroweak measurements at the LHC. Placing all constraints together, we found that we are able to strongly constrain the boundary terms, while placing an upper bound on the radius of the extra dimensions.

Moving on to the bottom-up or model independent formalism, we utilize a higher dimension operator to study a novel DM scenario which has a very promising potential to provide a so-called "smoking gun" signal. This DM strategy is discussed in Chapter 4 and is an extension of work done in Refs. [56, 57]. It was partially motivated by the notion that the DM scenarios discussed in Chapters 2 and 3 need not be mutually exclusive. This is to say DM need not be composed of only one component. The dark sector may be somewhat more complicated than our naive expectations. This idea which incorporates multiple DM states is in fact very well motivated at the particle physics level and in astrophysics. The concept of multiple DM particles may imply difficulty in the search for DM, since there are even more unknowns. On the other hand, it may pave a way to even richer phenomenology with even better opportunities and tools to study the dark sector. Interestingly there exists the scenario of boosted dark matter which we discuss in great detail in Chapter 4. In this formalism we study two DM states, one

of which is heavy and is assumed to form a large part of the DM relic density of the Universe. The other is very light and forms a very small percentage of the relic abundance in the current Universe. The intricacies of this dark sector come about from the assumption that the heavier state is completely secluded and only interacts with the SM through the lighter state. Furthermore, the annihilations of the heavier DM state result in boosted light DM states which can be detected at experiments on the Earth. We investigate the flux of boosted DM when the heavier state accumulates at the galactic center and in the center of the Sun. We explore the possibilities of this potentially powerful signal at large volume experiments on the Earth and find that certain detector types will be more sensitive for this type of signal than others. Here we are particularly interested in the type of signal rather than the theory, therefore, we assume a dimension 6 four-fermion operator whose cutoff scale is set by the correct DM thermal relic abundance. In principle the DM need not be fermions, but can also be vectors or scalars and specific models are left for the future. In this rich phenomenology, we have the unique opportunity to detect a DM signal that would not be mimicked by any other known signature.

Finally, we discuss DM in the simplified model framework. It has been illustrated in the literature that these types of models can provide a natural and minimal way of studying theory with experimental data. Typically, simplified models involve a new particle acting as DM with some mediator particle responsible for the interactions between the DM and the SM. By doing so, one limits the number of parameters entering into the physics and can, therefore, efficiently map the DM experimental results onto the theory. Some of the most widely discussed simplified models in the literature are Higgs portals. Higgs portals are very well motivated theoretically through the low dimensional gauge and Lorentz invariant operator $H^\dagger H$. Due to this bilinear operator the Higgs can serve as a unique window into new physics beyond the SM. Motivated by a possibility that DM could be multicomponent in nature, in Chapter 5, we consider a simplified model with two dark matter particles. This work is based on Ref. [58]. The DM naturally arises from an ultraviolet complete theory where it interacts with the SM degrees of freedom primarily through the SM Higgs boson. Motivated also by the secluded nature of the dark sector in Chapter 4, we realize a vector DM which is naturally stabilized in the presence of a dark

charge conjugation symmetry. The vector interacts only at 1 loop level with the SM through another stable fermion state which is also stabilized by this charge conjugation. We investigate the evolution of both particles in the early Universe and their contribution to the relic abundance. We further examine the possibilities at direct detection experiments. However, current direct detection experiments set their limits assuming only one DM component. It is difficult to consider additional particles when setting such limits as there are many more assumptions to make with many uncertainties. We, therefore, rescale the cross-sections reported in direct detection experiments and obtain conservative constraints on our DM parameters. On a further note, it would be particularly interesting to see how experimental results would be impacted if experiments could perform searches assuming multicomponent dark matter. This is an intriguing problem that would require input from both theorists and experimentalists to solve and might well lead to ground breaking discoveries. On the collider side, since the DM interacts primarily through the Higgs Boson, we consider constraints from searches for invisible Higgs decays at the LHC. We further point out that this is the first study incorporating a multicomponent DM model with a vector and fermion which are stabilized under the same symmetry. We discuss our conclusions at the end.

Part I

Model Dependent Framework

The best way of fully understanding the nature of dark matter is by characterizing it in a complete theory. In this way we get to determine properties such as its mass, its spin as well as how it became stable. Building the correct dark matter model is a challenging prospect as there are many unknowns that need to be taken into account. Our best option seems to be to start with what we know and experimentally have confirmed. The standard model is a well known theory and can serve as a basis on which we study new physics. This may be realized in many ways, for instance, two of the prominent methods are to extend the SM gauge symmetry or its space-time symmetry. In this part of the dissertation we will concentrate on model dependent methods of studying dark matter, focusing on novel phenomenologies that arise in gauge and space-time extensions of the SM respectively.

We first focus on extending the gauge symmetry of the SM, which is described by $SU(3)_c \times SU(2)_W \times U(1)_Y$. We do so by considering a model described by $SU(3)_c \times SU(2)_L \times SU(2)_R \times U(1)_{B-L}$ in Chapter 2. This is known as the left-right extension of the SM and was developed primarily to understand some fundamental questions which could not be explained by the SM. These include, parity violation in the SM (why the SM only accommodates left-handed fermion doublets and not right handed ones.) and SM neutrino masses. These fundamental questions may be answered by the presence of heavier states arising in the extended gauge, Higgs and fermion sectors. These heavy states may include dark matter which can be searched for either in direct detection, indirect detection experiments or at colliders. We study three dark matter scenarios that arise when heavy right handed fermions are able to mix with the heavy Higgs bosons. We focus on the phenomenology of these dark matter scenarios by first studying their contribution to the observed DM relic abundance and then assessing their bounds from direct detection experiments. To do this we first discuss the overall model, outlining all the interactions between the different particles. Then we discuss the interaction of the dark matter with the heavier particles in each DM scenario. We then calculate the relic abundance as well as direct detection cross-sections. This information is then matched to the observed relic abundance as well as the direct detection bounds from the current experiments and projections for the future experiments. In order to obtain our figures we make certain assumptions for the parameters involved, which we dis-

cuss in the main text. We found that the Singlet-Bidoublet DM model was the most constrained by the current most competitive direct detection experiment, but had a lot of hope for detection in next generation experiments. We further found that for the DM masses we considered, we were able to evade the bounds from current indirect detection experiments. The bounds on these models are heavily dependent on the initial assumptions and choices of parameters. Yet the results we show are also quite important as the constrained regions in the parameter spaces we illustrate, tell us what dark matter is not.

Extending the gauge symmetry of the SM is not the only manner in which we may obtain new physics. For Chapter 2, we focus on a space-time extension of the SM. The SM lives in a (1+3)-dimensional universe, where the 1 represents the time coordinate and the 3 represents the (x,y,z) space coordinates. We may consider new physics effects by extending the SM space-time by an arbitrary amount. Indeed there are many ways to do this and each one contains its own complexities and contribution to new physics. One way to extend the space-time symmetry of the SM is by one extra space dimension. These types of scenarios are called extra dimension models. A variation of these models comes in the form of Universal Extra Dimensions (UED) in which the SM particles are allowed to propagate along the extra dimension and in turn give rise to new particles at higher energy scales. In models of Minimal UED, the lightest of these new particles is stable and is the dark matter particle. In this section we will focus on a Next-to-Minimal UED model in which we incorporate boundary localized Kinetic terms (BLKTs). The BLKT's have an effect on the dark matter phenomenology and including them in the electroweak sector introduces a new vector dark matter candidate which is a mixture of the extra-dimensional weak gauge boson and the extra-dimensional hypercharge gauge boson.

In order to study the DM phenomenology in this scenario, we first describe the model and the origin of the BLKT's. We then consider the various experimental bounds that can tell us which part of our model is viable. We first investigate the constraints from precision electroweak measurements, which we use to place bounds on the inverse radius of the extra dimension. Then we study the bounds from LHC dilepton resonance searches, by calculating the cross-sections for the production of a level 2 KK

resonance and subsequent decay into two leptons at the LHC. We match this cross-section to what has been reported by the experimental groups at the LHC and turn this into bounds on the BLKT parameter space. We subsequently move on to calculate the relic abundance and the direct detection rates, matching onto the observed relic abundance and current experimental direct detection rates respectively. These help us to place complementary bounds on the BLKT parameter space. We also use our calculated rates to study projections for the upcoming next generation direct detection experiments. For different values of the inverse radius, we found that our DM completely evades current direct detection experiments while having much hope for detection in future experiments. We also find that relic abundance and dilepton resonance searches provide the most stringent constraints, thus excluding a large part of the parameter space and again giving us information on what DM is not.

In this part of the dissertation we present two independent extensions of the SM, which give rise to different phenomenologies. The constraints we obtain depend on the parameters we choose and on the assumptions we introduce, thus potentially biasing us to certain conclusions. However if a DM signal is confirmed a full model such as those presented here is needed to fully characterize DM and tell us how it may interact with other new physics.

Chapter 2

Gauge Extension of the Standard Model

The ATLAS collaboration has recently reported an excess of events consistent with those arising from an approximately 2 TeV resonance decaying to a pair of Standard Model (SM) gauge bosons. If interpreted as a WZ final state, this excess has a local significance of 3.4σ, or 2.5σ after taking into account an appropriate trials factor [59]. The possibility that this excess could be associated with new physics is strengthened by the results of Run 1 dijet searches at CMS [60] and ATLAS [61], each of which report a modest excess (2.2 and 1.0σ, respectively) at a similar mass of approximately 1.8 TeV. In addition, the CMS collaboration reports 2.1 and 1.5σ excesses in their searches for leptonically-tagged resonances decaying to HW [62] or to gauge bosons [63], respectively, both at approximately 1.8 TeV.

These anomalies have renewed interest in models with a new charged gauge boson, W', with a mass of approximately 1.8 to 2 TeV, including those predicted within the context of left-right symmetric models [64–68]. Such scenarios have long been perceived as theoretically attractive [69–75], and can emerge naturally within the context of Grand Unified Theories based on $SO(10)$ or E_6 [76–78]. At low energies, left-right symmetric models are described by the gauge group $SU(3)_c \times SU(2)_L \times SU(2)_R \times U(1)_{B-L}$, and thus include new massive gauge bosons, W' and Z', that couple to right-handed fermions, including right-handed neutrinos. To be phenomenologically viable, left-right symmetric models also require an extended Higgs sector, and often include additional fermionic particle content. It has been suggested that the modest excess of same-sign dilepton events with multiple b-jets observed at ATLAS [79] could

be explained by the Higgs sector of such a model, while a left-right symmetric model with TeV-scale right-handed neutrinos could account for the CMS excess of e^+e^- events that include a pair of jets with an invariant mass of $\sim$2 TeV [80]. Although the first 13 TeV data from the LHC have not been definitive [81–84], the ongoing run at the LHC is expected to reach the sensitivity required to conclusively test these models over the coming year [64].

There are a number of potentially viable dark matter candidates that one can identify within the context of left-right symmetric models [65, 85–88], and their supersymmetric extensions [89–91]. We limit our scope to non-supersymmetric models, considering a wide range of dark matter candidates contained within various $SU(2)_{L,R}$ fermion multiplets and their mixtures. In some respects, this follows the previous work of Heeck and Patra, who considered dark matter candidates that are members of left-right fermion triplets or quintuplets [85]. More recently, Garcia-Cely and Heeck extended this approach by considering those candidates found within fermion bidoublets or bitriplets, or scalar doublets or 7-plets [86]. In this study, we build upon this earlier work by considering dark matter candidates found within the fermion multiplets of a left-right symmetric model, but without restricting ourselves to pure states. In particular, we find that fermion singlet-triplet, singlet-bidoublet, and triplet-bidoublet mixtures each constitute phenomenologically viable dark matter candidates. Furthermore, we show that such states are automatically cosmologically stable, without the need for any additional parity or symmetry. In contrast to pure states, mixed dark matter in left-right symmetric models can undergo significant scattering with nuclei, potentially falling within the reach of direct detection experiments such as LUX, LUX-ZEPLIN (LZ), and XENON1T. Additionally, whereas the mass splitting between the neutral and charged particles of the dark sector is fixed when considering pure states, this splitting can be adjusted more freely in mixed models, allowing us, for example, to turn on or off the effects of coannihilation in the early universe.

Although we focus this study on the parameter space motivated by the diboson excess ($m_{W'} \sim 2$ TeV, $g_R \sim 0.5$), we note that dark matter within the context of left-right symmetric models would remain interesting even in the absence of such a putative signal. With this in mind, we have presented many of our results in a way that can be straightforwardly applied to other scenarios within the larger

parameter space of left-right symmetric models.

The remainder of this chapter is structured as follows. In Sec. 2.1, we discuss the Higgs and gauge sectors of left-right symmetric models, respectively, describing their particle content and interactions. In Sec. 2.2, we consider three scenarios in which the dark matter is a mixture of fermions found in $SU(2)$ singlets, bidoublets and triplets, in each case finding regions of parameter space that predict an acceptable thermal relic abundance and that are consistent with the constraints from direct detection experiments.

2.1 The Field Content of the Model

The spontaneous symmetry breaking of $SU(2)_L \times SU(2)_R \times U(1)_{B-L}$ down to $U(1)_{EM}$ requires an extended Higgs sector (for a review, see Ref. [92]). In particular, the minimal content of a left-right symmetric model includes a complex scalar triplet with quantum numbers $\Delta_R : (\mathbf{1},\mathbf{3},2)$, and a complex scalar bidoublet with quantum numbers $\phi : (\mathbf{2},\mathbf{2},0)$.

The electric charge of a given state is defined in relation to its weak isospin and $B-L$ quantum numbers:

$$Q = T_{3L} + T_{3R} + \frac{B-L}{2}\,. \tag{2.1}$$

This can be generalized further for triplets and bidoublets, respectively, according to the following:

$$\begin{aligned} Q\mathbf{T} &= \left[\frac{1}{2}\sigma_3, \mathbf{T}\right] + \frac{B-L}{2}\mathbf{T}, \\ Q\mathbf{B} &= \left[\frac{1}{2}\sigma_3, \mathbf{B}\right] + \frac{B-L}{2}\mathbf{B}, \end{aligned} \tag{2.2}$$

where $\mathbf{T}$ and $\mathbf{B}$ are 2×2 matrices in which a generic triplet or bidoublet can be embedded. The matrix $\mathbf{T}$ is further constrained to be traceless.

The charge conjugates of a triplet and a bidoublet, which we will use in Sec. 2.2, are defined as:

$$\tilde{\mathbf{T}} \equiv \sigma^2 \mathbf{T}^* \sigma^2 = -\mathbf{T}^\dagger,$$
$$\tilde{\mathbf{B}} \equiv \sigma^2 \mathbf{B}^* \sigma^2 \quad . \tag{2.3}$$

The right-handed Higgs triplet, Δ_R, breaks $SU(2)_L \times SU(2)_R \times U(1)_{B-L}$ down to $SU(2)_L \times U(1)_Y$ after acquiring a vacuum expectation value (VEV), v_R. Subsequently, the Higgs bidoublet, ϕ, breaks $SU(2)_L \times U(1)_Y$ down to $U(1)_{EM}$. The low-energy Higgs potential of this model corresponds to a restricted form of a two-Higgs doublet model (2HDM) [93]. Working in unitary gauge and the alignment limit (in which the lightest Higgs is SM-like), we parametrize these Higgs bosons as follows:

$$\Delta_R = \begin{pmatrix} \frac{g_R}{\sqrt{2}\, g_L} \frac{m_W}{m_{W'}} \, c_{2\beta} H^+ & \Delta^{++} \\ v_R + \frac{1}{\sqrt{2}} \Delta^0 & -\frac{g_R}{\sqrt{2}\, g_L} \frac{m_W}{m_{W'}} \, c_{2\beta} H^+ \end{pmatrix}, \tag{2.4}$$

$$\phi = \begin{pmatrix} c_\beta v + \frac{1}{\sqrt{2}}(c_\beta h + s_\beta H + i s_\beta A) & c_\beta H^+ \\ s_\beta H^- & s_\beta v + \frac{1}{\sqrt{2}}(s_\beta h - c_\beta H + i c_\beta A) \end{pmatrix},$$

where h, H, A, and $H^\pm$ represent the Higgs bosons found within a generic 2HDM, while Δ^0 and Δ^{++} denote the physical right-handed neutral and doubly charged scalars, respectively. The quantities g_R and g_L are the gauge couplings associated with $SU(2)_R$ and $SU(2)_L$, respectively, while $v = 174$ GeV is the SM Higgs VEV. $c_{N\beta}$, $s_{N\beta}$ are the cosine and sine of $N \times \beta$, where $\tan\beta$ is the ratio of the two neutral VEVs of ϕ, analogous to that of a 2HDM and N is an integer. To match the observed rate and mass of the diboson excess, we require $v_R \sim 3-4$ TeV and $g_R \sim 0.5$ [94]. In addition, matching to the observed $W' \to WZ$ rate also requires $0.5 \lesssim \tan\beta \lesssim 2$. The masses of H,A, and $H^\pm$ naturally take on a common value that can lie anywhere between the weak scale and v_R.

The only renormalizable gauge invariant interactions between SM quarks and the extended Higgs

sector are given by:

$$-\mathscr{L} \supset \overline{Q}_L \left(y\, \phi + \tilde{y}\, \tilde{\phi} \right) Q_R + \text{h.c.}\,, \tag{2.5}$$

which after electroweak symmetry breaking (EWSB), gives rise to the following quark mass terms:

$$-\mathscr{L} \supset \left(y\, c_\beta + \tilde{y}\, s_\beta \right) v\, \overline{u} u + \left(y\, s_\beta + \tilde{y}\, c_\beta \right) v\, \overline{d} d\,. \tag{2.6}$$

A modest tuning of these parameters is required to explain the hierarchy between the top and bottom quark masses. For $\tan\beta = 0.5$ or 2, the Yukawa couplings must be tuned at approximately the 2% level (allowing for a cancellation between $y s_\beta$ and $\tilde{y} c_\beta$).

Similar terms can be written for the lepton sector, but with an additional coupling to the triplet Higgs:

$$-\mathscr{L} \supset y_M\, \overline{(L_R)^c}\, i\sigma^2 \Delta_R\, L_R + \text{h.c.}\,. \tag{2.7}$$

After EWSB, this term gives a Majorana mass to the right-handed neutrinos and also introduces an interaction of the form $\Delta^{++}\, \overline{(l_R)^c}\, l_R$.

Expanding Eq. (2.5) in terms of the physical Higgs states, we can write the heavy Higgs interactions with SM fermions as follows:

$$\begin{aligned}
\mathscr{L} \supset\; & \frac{m_d - m_u s_{2\beta}}{\sqrt{2}\, v c_{2\beta}}\, H\, \overline{u} u + \frac{m_u - m_d s_{2\beta}}{\sqrt{2}\, v c_{2\beta}}\, H\, \overline{d} d - \frac{m_l t_{2\beta}}{\sqrt{2}\, v}\, H\, \overline{l} l \\
& + \frac{m_d - m_u s_{2\beta}}{\sqrt{2}\, v c_{2\beta}}\, A\, \overline{u}\, i\gamma^5 u - \frac{m_u - m_d s_{2\beta}}{\sqrt{2}\, v c_{2\beta}}\, A\, \overline{d}\, i\gamma^5 d + \frac{m_l t_{2\beta}}{\sqrt{2}\, v}\, A\, \overline{l}\, i\gamma^5 l \\
& + \left\{ \frac{1}{v\, c_{2\beta}}\, H^+\, \overline{u} \left[-\left(m_u - m_d s_{2\beta} \right) P_R + \left(m_d - m_u s_{2\beta} \right) P_L \right] d + \frac{m_l t_{2\beta}}{v}\, H^+\, \overline{\nu}\, P_R\, l + \text{h.c.} \right\}.
\end{aligned} \tag{2.8}$$

The renormalizable interaction in Eq. (2.5) couples both Higgs doublets within ϕ to up-type and down-type quarks, and can lead to flavor changing couplings through tree-level exchange of the heavy neutral Higgs bosons. For heavy Higgses above a few TeV in mass, however, these flavor constraints can be avoided [95]. Alternatively, the Yukawa couplings of the quarks can be made to be those of a

Type II 2HDM if the renormalizable couplings are small and instead the quarks acquire a mass through higher dimensional operators involving the triplet Higgs [93]. We will consider Higgs couplings as in Eq. (2.5) and assume that all flavor constraints are satisfied.

The gauge bosons acquire masses from the VEVs of the Higgs triplet, Δ_R, and bidoublet, ϕ. Defining $W^{\pm\mu}_{L,R} \equiv \frac{1}{\sqrt{2}}\left(W^{1\mu}_{L,R} \mp i W^{2\mu}_{L,R}\right)$, the mass matrices for these states are given as follows:

$$\mathscr{L} \supset \begin{pmatrix} W_L^{+\mu} & W_R^{+\mu} \end{pmatrix} \begin{pmatrix} \frac{1}{2}\, g_L^2\, v^2 & -\frac{1}{2}\, g_L\, g_R\, s_{2\beta}\, v^2 \\ & \\ -\frac{1}{2}\, g_L g_R\, s_{2\beta}\, v^2 & g_R^2\, \left(v_R^2 + \frac{1}{2} v^2\right) \end{pmatrix} \begin{pmatrix} W_{L\mu}^- \\ \\ W_{R\mu}^- \end{pmatrix}, \tag{2.9}$$

and

$$\mathscr{L} \supset \frac{1}{2} \begin{pmatrix} W_{L\mu}^3 & W_{R\mu}^3 & B_\mu \end{pmatrix} \begin{pmatrix} \frac{1}{2}\, g_L^2\, v^2 & -\frac{1}{2}\, g_L\, g_R\, v^2 & 0 \\ & & \\ -\frac{1}{2}\, g_L\, g_R\, v^2 & \frac{1}{2}\, g_R^2\, v^2 + 2\, g_R^2\, v_R^2 & -2\, g_{B-L}\, g_R\, v_R^2 \\ & & \\ 0 & -2\, g_{B-L}\, g_R\, v_R^2 & 2\, g_{B-L}^2\, v_R^2 \end{pmatrix} \begin{pmatrix} W_{L\mu}^3 \\ \\ W_{R\mu}^3 \\ \\ B_\mu \end{pmatrix}, \tag{2.10}$$

where g_{B-L} and B_μ are the $U(1)_{B-L}$ gauge coupling and field.

Diagonalizing the $W^{\pm}_{L,R}$ mass matrix in the $v_R \gg v$ limit yields two charged gauge bosons of mass $m_W = g_L v/\sqrt{2}$ and $m_{W'} = g_R v_R$. The mixing matrix between these states is given by:

$$\begin{pmatrix} W_{L\mu}^{\pm} \\ \\ W_{R\mu}^{\pm} \end{pmatrix} = \begin{pmatrix} \cos\theta_+ & -\sin\theta_+ \\ & \\ \sin\theta_+ & \cos\theta_+ \end{pmatrix} \begin{pmatrix} W_\mu^{\pm} \\ \\ W_\mu^{\prime\pm} \end{pmatrix}, \tag{2.11}$$

such that

$$\sin\theta_+ \equiv \frac{g_R}{g_L} \left(\frac{m_W}{m_{W'}}\right)^2 s_{2\beta}\ . \tag{2.12}$$

Here g_L is equivalent to the weak SM gauge coupling, g.

Diagonalizing the W_L^3, W_R^3, B mass matrix yields three neutral gauge bosons with the following masses (again, in the $v_R \gg v$ limit):

$$m_A^2 = 0\,, \quad m_Z^2 = \left(g_L^2 + \frac{g_R^2 g_{B-L}^2}{g_R^2 + g_{B-L}^2}\right)\frac{v^2}{2}\,, \quad m_{Z'}^2 = 2\left(g_R^2 + g_{B-L}^2\right)v_R^2. \tag{2.13}$$

Comparing the expression for m_Z to that found in the SM, $m_Z^2 = \left(g_L^2 + g'^2\right)\frac{v^2}{2}$, we arrive at the following *definition* for the SM hypercharge gauge coupling:

$$g' \equiv \frac{g_R\, g_{B-L}}{\sqrt{g_R^2 + g_{B-L}^2}}\,. \tag{2.14}$$

Consistency with the SM requires $g_L \approx 0.65$ while fixing to the diboson rate requires $g_R \approx 0.45 - 0.6$. Together, these in turn imply $g_{B-L} \approx 0.45 - 0.6$.

The mass eigenstates, keeping leading order terms in v/v_R, are given by:

$$\begin{pmatrix} W_{L\mu}^3 \\ W_{R\mu}^3 \\ B_\mu \end{pmatrix} = \begin{pmatrix} s_w & c_w & -\frac{g_R}{2g_L}c_R^3\left(\frac{m_W}{m_{W'}}\right)^2 \\ c_w s_R & -s_w s_R & c_R \\ c_w c_R & -s_w c_R & -s_R \end{pmatrix} \begin{pmatrix} A_\mu \\ Z_\mu \\ Z'_\mu \end{pmatrix}\,, \tag{2.15}$$

where we have defined

$$s_w \equiv \sin\theta_w \equiv \frac{g'}{\sqrt{g_L^2 + g'^2}}\,, \quad c_w \equiv \cos\theta_w\,, \quad s_R \equiv \sin\theta_R \equiv \frac{g'}{g_R}\,, \quad c_R \equiv \cos\theta_R\,. \tag{2.16}$$

Expressions for the couplings of the Z' and W' to SM fermions, the cubic self-interaction terms involving non-SM gauge bosons, and the non-SM cubic gauge-Higgs interactions terms can be found in the appendix of Ref. [52]. In what follows, we fix the parameters of the new physics to values that fit the excess in the diboson, and related, channels. In particular, we take the $SU(2)_R$ gauge coupling $g_R = 0.45$ and $M_{W'} = 1.9$ TeV, which leads to $M_{Z'} = 4.4$ TeV. We take the ratio of the VEVs in the bidoublet scalar to be $\tan\beta = 2$, and we assume that the physical scalars in the Higgs triplet are sufficiently heavy such

$SU(2)$ Fields	Mixing Possible?
singlet-doublet	×
singlet-triplet	✓
singlet-bidoublet	✓
doublet-triplet	×
doublet-bidoublet	×
triplet-bidoublet	✓

Table 2.1 Whether or not mixing is possible through renormalizable Yukawa couplings of fermion multiplets to the bidoublet and triplet Higgs bosons. Combinations that include multiplets larger than those listed are not able to mix.

that they take no part in the dynamics. Although it has been shown [94] that if some of the right-handed neutrinos have mass around 1.4–1.7 TeV then their 3-body decay to ejj can explain a CMS excess in e^+e^-jj final state [96], we choose here, for simplicity, to decouple these states. Keeping them in the mass range necessary to explain the e^+e^-jj excess would increase the W' and Z' widths by less than 10%, which has a small effect on the dark matter relic abundance calculation.

2.2 The Dark Matter Sector

Previous studies of dark matter in (non-supersymmetric) left-right symmetric models have focused on dark matter composed of pure multiplets. For example, the authors of Ref. [85] considered dark matter candidates that are members of a left-right fermion triplet or quintuplet, while Ref. [86] extended this to include those states found within a fermion bidoublet or bitriplet, or a scalar doublet or 7-plet. Such candidates can closely resemble what is sometimes referred to as "minimal dark matter" [44, 97–99]. In this study, we extend the analysis to a wider range of scenarios by considering models in which the dark matter candidate is not necessarily in a pure state, but may instead be a fermion that is a mixture of two or more multiplets, similar to neutralinos in supersymmetry. For implementation of this class of models in regards to the recently reported 750 GeV diphoton excess, see e.g., Ref. [100].

Although we restrict our analysis to fermionic dark matter (motivated, in part, by supersymmetric completions of left-right symmetric models [101]), we consider arbitrary combinations of fermion multiplets. Mixing between the fermions is induced through the coupling to a bidoublet or triplet Higgs, ϕ

Field	Charges	Spin
S	$(\mathbf{1},\mathbf{1},0)$	1/2
T_1	$(\mathbf{1},\mathbf{3},2)$	1/2
T_2	$(\mathbf{1},\mathbf{3},-2)$	1/2

Table 2.2 The $SU(2)_L$, $SU(2)_R$, and $B-L$ charge assignments in the singlet-triplet model. All fields are colorless.

and Δ_R. At the renormalizable level, gauge invariance allows only a finite set of possible combinations, which involves only singlets, $SU(2)$ doublets, bidoublets, and $SU(2)_R$ triplets. There are no combinations that include a higher multiplet. In Table 2.1 we list all possible combinations of distinct fermion representations that can mix via renormalizable Yukawa couplings to the bidoublet and triplet Higgses.

In light of these considerations, we restrict our analysis to the following three mixed cases: singlet-triplet, singlet-bidoublet, and triplet-bidoublet dark matter. In the following three subsections, we will discuss each of these cases in turn.

2.2.1 The Singlet-Triplet Model

In this scenario, we introduce three Weyl fermions: a singlet, S, and two triplets, $T_{1,2}$, with charge assignments as given in Table 2.2. The triplets are each given $B-L$ charge so that they can couple to the triplet Higgs, Δ_R. Two triplets are needed for anomaly cancellation, which also allows a bare triplet mass term. Note that the presence of $SU(2)_R$ triplets without corresponding $SU(2)_L$ triplets breaks the $L \leftrightarrow R$ symmetry that is invoked in many left-right symmetric models [85, 86, 92].

The triplets can be parametrized as:

$$T_1 = \begin{pmatrix} t_1^+/\sqrt{2} & t_1^{++} \\ t_1^0 & -t_1^+/\sqrt{2} \end{pmatrix}, \quad T_2 = \begin{pmatrix} t_2^-/\sqrt{2} & t_2^0 \\ t_2^{--} & -t_2^-/\sqrt{2} \end{pmatrix}, \tag{2.17}$$

where the 0 and $\pm$ superscripts are labels assigned with the foresight that these components will make up neutral or electrically charged fermions, accordingly (see Eq. 2.2). The factors of $\sqrt{2}$ are fixed in order to guarantee canonical normalization of the kinetic terms. The most general renormalizable

Lagrangian for the dark sector is given by:

$$\begin{aligned}\mathscr{L} \supset\ & S^\dagger i\overline{\sigma}^\mu \partial_\mu S + \mathrm{tr}(T_1^\dagger i\overline{\sigma}^\mu D_\mu T_1) + \mathrm{tr}(T_2^\dagger i\overline{\sigma}^\mu D_\mu T_2) \\ & - \left[\frac{1}{2} M_S S^2 + M_T\ \mathrm{tr}(T_1 T_2) + \lambda_1\ S\ \mathrm{tr}(T_1 \Delta_R^\dagger) + \lambda_2\ S\ \mathrm{tr}(T_2 \Delta_R) + \mathrm{h.c.}\right], \end{aligned} \tag{2.18}$$

where 2-component Weyl spinor indices are implied, and traces refer to sums over $SU(2)_R$ indices. M_S and M_T are the bare singlet and triplet masses, respectively, and $\lambda_{1,2}$ are dimensionless Yukawa couplings. After Δ_R acquires a VEV, these couplings generate mass terms for three Majorana fermions and two Dirac fermions,

$$-\mathscr{L} \supset \frac{1}{2}\begin{pmatrix} S & t_1^0 & t_2^0 \end{pmatrix} \begin{pmatrix} M_S & \lambda_1\ v_R & \lambda_2\ v_R \\ \lambda_1\ v_R & 0 & M_T \\ \lambda_2\ v_R & M_T & 0 \end{pmatrix} \begin{pmatrix} S \\ t_1^0 \\ t_2^0 \end{pmatrix} + M_T t_1^+ t_2^- + M_T t_1^{++} t_2^{--} + \mathrm{h.c.}\ , \tag{2.19}$$

where S and $t_{1,2}^0$ denote the singlet and neutral triplet components, respectively. The electrically charged states are Dirac fermions of mass M_T :

$$\chi^+ \equiv \begin{pmatrix} t_1^+ \\ (t_2^-)^\dagger \end{pmatrix} \quad \text{and} \quad \chi^{++} \equiv \begin{pmatrix} t_1^{++} \\ (t_2^{--})^\dagger \end{pmatrix}\ . \tag{2.20}$$

Diagonalizing the neutral mass matrix yields the following decomposition:

$$\begin{aligned} S &= N_S^1\ \chi_1 + N_S^2\ \chi_2 + N_S^3\ \chi_3 \\ t_1^0 &= N_{t_1}^1\ \chi_1 + N_{t_1}^2\ \chi_2 + N_{t_1}^3\ \chi_3 \\ t_2^0 &= N_{t_2}^1\ \chi_1 + N_{t_2}^2\ \chi_2 + N_{t_2}^3\ \chi_3\ . \end{aligned} \tag{2.21}$$

Bearing in mind field redefinitions that fix wrong-sign mass terms such as $\chi \to i\chi$, the mixing angles in Eq. (2.21) are promoted to complex numbers. Moving to 4-component notation, we define the Majorana

spinors as follows:

$$\chi_i^{(\text{4-comp.})} \equiv \begin{pmatrix} \chi_i \\ \chi_i^\dagger \end{pmatrix}. \tag{2.22}$$

Throughout the remainder of this study, we will drop the superscripts for all 4-component spinors.

To calculate the thermal relic abundance of dark matter, we utilize the publicly available programs `FeynRules` and `MicrOMEGAs` and cross-check using `MadDM`, for a short description of these please see the appendix. In Fig. 2.1, we present examples of the parameter space in which an abundance compatible with the measured cosmological dark matter density is obtained. We present these results in terms of the singlet and triplet masses, M_S and M_T, and for various choices of the following parameters:

$$\begin{aligned} y_{\text{ST}} &\equiv \sqrt{\lambda_1^2 + \lambda_2^2}\,, \\ \tan\theta_{\text{ST}} &\equiv \lambda_1/\lambda_2 \quad , \end{aligned} \tag{2.23}$$

where λ_1 and λ_2 are the Yukawa couplings introduced in Eq. (2.18).

The process of thermal freeze-out is largely governed by the masses of χ_1 and $\chi^\pm$. In particular, the desired relic abundance is obtained near the W' or Z' resonances, corresponding to $m_{\chi_1} \approx m_{W'}/2 \approx 1$ TeV or $m_{\chi_1} \approx m_{Z'}/2 \approx 2$ TeV, respectively. In the left frame of Fig. 2.1, $|\tan\theta_{\text{ST}}| \sim 1$, in which case there is an enhanced parity symmetry acting on the triplets $T_{1,2}$. As a result, the singlet, S, mixes with only one linear combination of t_1^0 and t_2^0, while the other remains degenerate with the charged states. For sufficiently small values of the triplet mass, $M_T \lesssim M_S$, the lightest neutral and charged fermions in the dark sector are approximately degenerate, leading to efficient coannihilations in the early universe through the s-channel exchange of a W'. Alternatively, in the right frame of this figure, $|\tan\theta_{\text{ST}}| \gg 1$, and there is a significant mass splitting between the neutral and charged states, suppressing the role of coannihilations. In each frame, we have adopted $g_R = 0.45$, $m_{W'} = 1.9$ TeV, and $\tan\beta = 2$, motivated by the observed characteristics of the diboson excess. We note that if both the neutral component of the Higgs triplet, Δ_0, and the right-handed neutrinos, ν_R, are relatively light, dark matter annihilations to a $\nu_R\nu_R$ final state could play a significant role in the determination of the relic abundance. Throughout

our study, however, we will assume that these states are heavy and neglect their contribution.

In this model, the elastic scattering of dark matter with nuclei is dominated by Z' exchange. The cross section for this process is spin-dependent, and of the following magnitude:

$$\sigma_{\rm SD} \approx 2 \times 10^{-45}\,{\rm cm}^2 \times \left(\frac{g^{(1)}_{Z'}}{0.1}\right)^2 \left(\frac{4\ {\rm TeV}}{m_{Z'}}\right)^4, \tag{2.24}$$

where $g^{(1)}_{Z'}$ is the dark matter's coupling to the Z' (see the appendix in Ref. [52]). Even for relatively large values of this coupling (corresponding to a large value of $|N^1_{t_1}|^2 - |N^1_{t_2}|^2$), the predicted cross section is well below the reach of current and planned experiments, and likely below the so-called "neutrino floor" [49].

Also shown in Fig. 2.1, are the regions of parameter space in which the W' has a large branching fraction to the dark sector. This is motivated by the fact that the rate associated with the diboson excess naively requires $g_R \approx 0.4 - 0.6$, which is in contrast to some theoretical expectations favoring $g_R = g_L \approx 0.65$. Decays of the W' to particles in the dark sector could plausibly accommodate such an equality. We estimate that this would require a branching fraction of several tens of percents. However, given the rough nature of this estimate, in Fig. 2.1 (as well as in Figs. 2.2 and 2.3), we show, for illustration, regions of parameter space where ${\rm BR}(W' \to \text{dark sector}) \gtrsim 10\%$.

In order to ensure a viable dark matter candidate, it is imperative that the lightest dark sector state is electrically neutral. In the decoupled limit, $M_T \ll M_S$, the lightest neutral and charged states are nearly degenerate at tree-level, suggesting that radiative corrections are potentially important. In Ref. [52], the full set of one-loop corrections to the dark sector masses are calculated and it is found that $m_{\chi^\pm}, m_{\chi^{\pm\pm}} > m_{\chi_1}$ throughout the entirety of the parameter space shown in Fig. 2.1. Alternatively, for $M_S \gtrsim 50$ TeV $\gg M_T$, radiative corrections lead to $m_{\chi^\pm}, m_{\chi^{\pm\pm}} < m_{\chi_1}$ when $\tan\theta_{\rm ST} = -1.5$ and the remaining parameters are chosen as in Fig. 2.1.

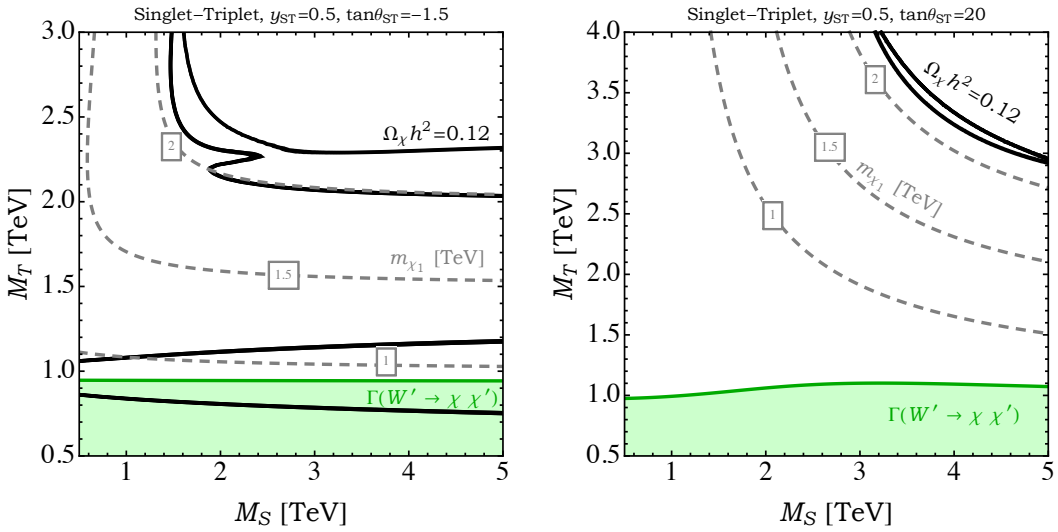

Fig. 2.1 Phenomenology of singlet-triplet dark matter. Along the solid black contours, the thermal relic abundance is in agreement with the measured cosmological dark matter density ($\Omega_\chi h^2 = 0.12$). Also shown as dashed grey lines are contours of constant dark matter mass (as labeled). In this model, thermal freeze-out is dominated by resonant annihilation through the Z' or resonant coannihilation through the W'. In each frame, we have adopted $g_R = 0.45$ and $m_{W'} = 1.9$ TeV in order to match the rate and energy of the diboson excess, and $\tan\beta = 2$ to accommodate the required $W' \to WZ$ branching fraction. The green shaded regions are those in which the W' decays to particles residing within the dark matter sector with a branching fraction greater than 10%. This is not a constraint, but rather a part of the parameter space in which we may have Left-right symmetry, i.e. $g_L = g_R$. Assuming the singlet-triplet DM constitutes all the dark matter in the Universe, the black solid contours indicate the parts of the parameter space where we must lie.

2.2.2 The Singlet-Bidoublet Model

In this section, we introduce two Weyl fermions: a singlet, S, and a bidoublet, B, with charge assignments as given in Table 2.3. The bidoublet is parametrized as follows:

$$B = \begin{pmatrix} b_1^0 & -b_2^+ \\ b_1^- & b_2^0 \end{pmatrix}, \tag{2.25}$$

where the 0 and $\pm$ superscripts are labels chosen with the foresight that these fermions will make up neutral or electrically charged fermions, accordingly (see Eq. 2.2). The most general renormalizable

Field	Charges	Spin
S	$(\mathbf{1},\mathbf{1},0)$	1/2
B	$(\mathbf{2},\mathbf{2},0)$	1/2

Table 2.3 The $SU(2)_L$, $SU(2)_R$, and $B-L$ charge assignments in the singlet-bidoublet model. All fields are colorless.

Lagrangian for the dark sector is given by:

$$\begin{aligned}\mathscr{L} \supset\ & S^\dagger i\overline{\sigma}^\mu \partial_\mu S + \mathrm{tr}(B^\dagger i\overline{\sigma}^\mu D_\mu B) \\ & - \left[\frac{1}{2}M_S S^2 + \frac{1}{2}M_B\ \mathrm{tr}(B\tilde{B}^\dagger) + \lambda\ S\ \mathrm{tr}(B\phi^\dagger) + \tilde{\lambda}\ S\ \mathrm{tr}(B\tilde{\phi}^\dagger) + \mathrm{h.c.}\right],\end{aligned} \tag{2.26}$$

where 2-component Weyl spinor indices are implied, and traces refer to sums over $SU(2)$ indices. M_S and M_B denote the bare singlet and bidoublet masses, respectively, and λ and $\tilde{\lambda}$ are dimensionless Yukawa couplings. After EWSB, the dark sector fermion masses are described by,

$$-\mathscr{L} \supset \frac{1}{2}\begin{pmatrix} S & b_1^0 & b_2^0 \end{pmatrix}\begin{pmatrix} M_S & v(\lambda c_\beta + \tilde{\lambda} s_\beta) & v(\lambda s_\beta + \tilde{\lambda} c_\beta) \\ v(\lambda c_\beta + \tilde{\lambda} s_\beta) & 0 & M_B \\ v(\lambda s_\beta + \tilde{\lambda} c_\beta) & M_B & 0 \end{pmatrix}\begin{pmatrix} S \\ b_1^0 \\ b_2^0 \end{pmatrix} + M_B b_1^- b_2^+ + \mathrm{h.c.}\,. \tag{2.27}$$

Whereas S and the neutral bidoublet components, $b_{1,2}^0$, mix to form three Majorana fermions, the charged components constitute a single charged Dirac fermion of mass M_B:

$$\chi^+ \equiv \begin{pmatrix} b_2^+ \\ (b_1^-)^\dagger \end{pmatrix}. \tag{2.28}$$

As before, we diagonalize the neutral mass matrix by decomposing the neutral gauge eigenstates in

terms of the mass eigenstates as,

$$\begin{aligned} S &= N_S^1\ \chi_1 + N_S^2\ \chi_2 + N_S^3\ \chi_3 \\ b_1^0 &= N_{b_1}^1\ \chi_1 + N_{b_1}^2\ \chi_2 + N_{b_1}^3\ \chi_3 \\ b_2^0 &= N_{b_2}^1\ \chi_1 + N_{b_2}^2\ \chi_2 + N_{b_2}^3\ \chi_3\ , \end{aligned} \tag{2.29}$$

and we again adopt 4-component notation for the Majorana spinors. Ref. [52] provides expressions describing the interactions between the singlet-bidoublet dark sector and gauge or Higgs bosons.

In Fig. 2.2, we explore some of the phenomenological features of this model, presenting our results in terms of M_B, M_S, m_A $(= m_H, m_{H^\pm})$, and the parameters:

$$\begin{aligned} y_{\text{SB}} &\equiv \sqrt{\lambda^2 + \tilde{\lambda}^2}, \\ \tan\theta_{\text{SB}} &\equiv \lambda\ /\ \tilde{\lambda} \quad , \end{aligned} \tag{2.30}$$

where λ and $\tilde{\lambda}$ are the Yukawa couplings as defined in Eq. (2.26).

Dark matter freeze-out is largely dictated by annihilations and coannihilations through the s-channel exchange of a Z' or W' gauge boson. Additional annihilation channels become active if the heavy Higgs bosons have masses that are comparable to m_{χ_1}, in which case a region of parameter space analogous to the A-funnel in the MSSM is found near $m_{\chi_1} \approx m_A/2$. This is related to our choice of Yukawa structure in Eq. (2.8). In regions of parameter space with a light and mostly singlet dark matter candidate and a relatively light pseudoscalar Higgs, it may be possible to generate the Galactic Center gamma-ray excess [102–107] in this model, similar to as in the models described in Refs. [108, 109]. Furthermore, depending on the sign of $\tan\theta$, singlet mixing allows for enhanced annihilations through heavy scalars when $m_{\chi_1} \sim M_S \sim M_B$. If, on the other hand, the heavy Higgses are decoupled, proper freeze-out favors regions where χ_1 is predominantly bidoublet-like, and annihilations involving heavy gauge bosons lead to the correct relic density near the W' and Z' resonances.

For simplicity, we have ignored trilinear Higgs interactions involving one or more heavy scalars

since they depend explicitly on the ~ 10 parameters of the general Higgs potential. As a result, we have purposely neglected annihilation processes such as $\chi\chi \to A \to Ah$ in the evaluation of the dark matter relic density. However, since we do not consider dark matter masses much greater than a few TeV, we do not expect these interactions to dominate in any of the parameter space shown.

Elastic scattering between dark matter and nuclei is dominated by SM Higgs exchange, leading to a spin-independent cross section that may be within the reach of current or future direct detection experiments. The cross section for this process is spin-independent, and of the following magnitude:

$$\sigma_{\rm SI} \approx 2 \times 10^{-44}\,{\rm cm}^2 \times \left(\frac{\lambda_h^{(1)}}{0.1}\right)^2 , \tag{2.31}$$

where $\lambda_h^{(1)}$ is the dark matter couplings to the light Higgs (see the appendix of Ref. [52]). In Fig. 2.2, the shaded red regions are currently excluded by the constraints from LUX [110], whereas the shaded blue regions fall within the projected reach of LZ [111]. In calculating the dark matter coupling to nucleons, we have taken the scalar nucleon form factors as listed in Sec. 4 of Ref. [112].

Dark matter-nucleon scattering is suppressed for negative values of $\tan\theta_{\rm SB}$. The dark matter-Higgs coupling scales as,

$$\lambda_h^{(1)} \propto (1+\sin 2\beta \sin 2\theta_{\rm SB}) m_{\chi_1} + (\sin 2\beta + \sin 2\theta_{\rm SB}) M_B \ . \tag{2.32}$$

Note that there is a suppression of $\lambda_h^{(1)}$ if $\tan\beta$ and $\tan\theta_{\rm SB}$ are of opposite sign, as can be seen in the right-hand plots of Fig. 2.2. Furthermore, in this regime, there may be a direct detection blind spot (corresponding to a vanishing elastic scattering cross section) for non-trivial mixing when $\lambda_h^{(1)} = 0$, or equivalently

$$m_{\chi_1} = -\frac{\sin 2\beta + \sin 2\theta_{\rm SB}}{1+\sin 2\beta \sin 2\theta_{\rm SB}} M_B \ . \tag{2.33}$$

In the limit that $M_B \ll M_S$, the lightest neutral and charged states are nearly degenerate at tree-level. In this case, it is important to investigate whether radiative corrections guarantee that the lightest dark sector state is electrically neutral, crucial for any dark matter candidate. At the one-loop level,

$m_{\chi^\pm} > m_{\chi_1}$ throughout the parameter space shown in Fig. 2.2. However, in the case that $M_B = 500$ GeV, $y_{\rm SB} = 0.5$, and $\tan\theta_{\rm SB} = -2$, we find that $m_{\chi^\pm} < m_{\chi_1}$ for singlet masses as large as $M_S \gtrsim 50$ TeV.

2.2.3 The Triplet-Bidoublet Model

In this model, we introduce two Weyl fermions: a triplet, T, and a bidoublet, B, with charges as shown in Table 2.4. The triplet and bidoublet are parametrized as:

$$T = \begin{pmatrix} t^0/\sqrt{2} & t_2^+ \\ t_1^- & -t^0/\sqrt{2} \end{pmatrix}, \quad B = \begin{pmatrix} b_1^0 & -b_2^+ \\ b_1^- & b_2^0 \end{pmatrix}, \tag{2.34}$$

where the 0 and $\pm$ superscripts are labels assigned with the foresight that these fermions will make up neutral or electrically charged fermions, accordingly (see Eq. 2.2), and the factors of $\sqrt{2}$ are fixed in order to guarantee canonical normalization of the kinetic terms. The most general renormalizable Lagrangian for the dark sector is given by:

$$\begin{aligned} \mathscr{L} \;&\supset\; \mathrm{tr}(T^\dagger i\overline{\sigma}^\mu D_\mu T) + \mathrm{tr}(B^\dagger i\overline{\sigma}^\mu D_\mu B) \\ &-\; \left[\frac{1}{2}M_T\ \mathrm{tr}(T^2) + \frac{1}{2}M_B\ \mathrm{tr}(B\tilde{B}^\dagger) + \lambda\ \mathrm{tr}(BT\phi^\dagger) + \tilde{\lambda}\ \mathrm{tr}(BT\tilde{\phi}^\dagger) + \mathrm{h.c.}\right], \end{aligned} \tag{2.35}$$

where 2-component Weyl spinor indices are implied, and traces refer to sums over $SU(2)$ indices. M_T and M_B are bare triplet and bidoublet masses, respectively, and λ and $\tilde{\lambda}$ are dimensionless Yukawa couplings. After EWSB, the neutral and charged fermions mix according to the following mass matrices:

$$\begin{aligned} -\mathscr{L} \;&\supset\; \frac{1}{2}\begin{pmatrix} t^0 & b_1^0 & b_2^0 \end{pmatrix} \begin{pmatrix} M_T & v(\lambda c_\beta + \tilde{\lambda} s_\beta)/\sqrt{2} & -v(\lambda s_\beta + \tilde{\lambda} c_\beta)/\sqrt{2} \\ v(\lambda c_\beta + \tilde{\lambda} s_\beta)/\sqrt{2} & 0 & M_B \\ -v(\lambda s_\beta + \tilde{\lambda} c_\beta)/\sqrt{2} & M_B & 0 \end{pmatrix} \begin{pmatrix} t^0 \\ b_1^0 \\ b_2^0 \end{pmatrix} \\ &+\; \begin{pmatrix} t_2^+ & b_2^+ \end{pmatrix} \begin{pmatrix} M_T & v(\lambda s_\beta + \tilde{\lambda} c_\beta) \\ -v(\lambda c_\beta + \tilde{\lambda} s_\beta) & M_B \end{pmatrix} \begin{pmatrix} t_1^- \\ b_1^- \end{pmatrix} + \mathrm{h.c.}\,. \end{aligned} \tag{2.36}$$

Field	Charges	Spin
T	$(\mathbf{1},\mathbf{3},0)$	1/2
B	$(\mathbf{2},\mathbf{2},0)$	1/2

Table 2.4 The $SU(2)_L$, $SU(2)_R$, and $B-L$ charge assignments in the triplet-bidoublet model. All fields are colorless.

The neutral triplet, t^0, and the neutral bidoublet components, $b^0_{1,2}$, mix to form three Majorana fermions, while the charged components mix to form two charged Dirac fermions. Diagonalizing the neutral mass matrix yields the following decomposition:

$$\begin{aligned} t^0 &= N_t^1\ \chi_1 + N_t^2\ \chi_2 + N_t^3\ \chi_3 \\ b_1^0 &= N_{b_1}^1\ \chi_1 + N_{b_1}^2\ \chi_2 + N_{b_1}^3\ \chi_3 \\ b_2^0 &= N_{b_2}^1\ \chi_1 + N_{b_2}^2\ \chi_2 + N_{b_2}^3\ \chi_3\ . \end{aligned} \tag{2.37}$$

Bearing in mind field redefinitions that fix wrong-sign mass terms such as $\chi \to i\chi$, the mixing angles in Eq. (2.37) are promoted to complex numbers. Similarly, for the charged states:

$$\begin{aligned} t_1^- &= U_{11}\ \chi_1^- + U_{12}\ \chi_2^- \\ b_1^- &= U_{21}\ \chi_1^- + U_{22}\ \chi_2^- \\ t_2^+ &= V_{11}\ \chi_1^+ + V_{12}\ \chi_2^+ \\ b_2^+ &= V_{21}\ \chi_1^+ + V_{22}\ \chi_2^+\ . \end{aligned} \tag{2.38}$$

Above, U_{ij} and V_{ij} are orthogonal matrices that are constructed from the eigenvectors of $\mathbf{M}^\dagger\mathbf{M}$ and $\mathbf{M}\mathbf{M}^\dagger$, respectively, where $\mathbf{M}$ is the charged mass matrix of Eq. (2.36). Once again, we adopt 4-component notation for the Majorana and Dirac spinors. Ref. [52] provides expressions describing the interactions between the triplet-bidoublet dark sector and gauge or Higgs bosons.

In Fig. 2.3, we present some of the phenomenological features of this model, describing the param-

eter space in terms of M_B, M_T, m_A ($= m_H, m_{H^\pm}$), and the following:

$$y_{\text{TB}} \equiv \sqrt{\lambda^2 + \tilde{\lambda}^2}, \qquad (2.39)$$
$$\tan\theta_{\text{TB}} \equiv \lambda \,/\, \tilde{\lambda} \quad ,$$

where λ and $\tilde{\lambda}$ are the Yukawa couplings as defined in Eq. (2.35).

Similar to the singlet-bidoublet case described in the previous subsection, dark matter freeze-out is governed primarily by annihilation either through s-channel W' or Z' exchange. The elastic scattering between dark matter and nuclei is also dominated by SM Higgs exchange, with a cross section that is the same as given in Eq. (2.31) (but using the expression for $\lambda_h^{(1)}$ found in the appendix of Ref. [52]). At present, the limits from LUX [110] exclude only a very small portion of the otherwise viable parameter space in this model (red shaded), although the future reach of experiments such as LZ is projected to be much more expansive (shaded blue). Note that heavy Higgs exchange destructively interferes with SM Higgs exchange and slightly suppresses the direct detection rate when $M_B \approx M_T$, which is most noticeable for $\tan\theta_{\text{TB}} > 0$. The dark matter coupling to the SM Higgs scales as

$$\lambda_h^{(1)} \propto (1 + \sin 2\beta \sin 2\theta_{\text{TB}}) m_{\chi_1} - (\sin 2\beta + \sin 2\theta_{\text{TB}}) M_B. \qquad (2.40)$$

In the limit that $M_B \gg M_T \sim m_{\chi_1}$, $\lambda_h^{(1)} \propto s_{2\beta} + s_{2\theta_{\text{TB}}}$ and no blind spot exists. In contrast, cancellations are possible when $M_T \gg M_B \sim m_{\chi_1}$, which implies $\lambda_h^{(1)} \propto (1 - s_{2\beta})(1 - s_{2\theta_{\text{TB}}})$. The latter case explains the lack of sensitivity for LZ when $M_T \gg M_B$ and $\tan\theta_{\text{TB}} > 0$ in Fig. 2.3.

Any viable dark matter candidate must be electrically neutral. Throughout the parameter space of Fig. 2.3, however, the lightest neutral and charged states are nearly degenerate at tree-level, implying that radiative corrections are potentially relevant. Using the one-loop corrections to the dark sector masses, we investigate whether this leads to $m_{\chi_1^\pm} < m_{\chi_1}$. Setting the $\overline{\text{MS}}$ renormalization scale to $\mu = 1$ TeV, we find that $m_{\chi_1^\pm} > m_{\chi_1}$ in the regions shown in Fig. 2.3. Alternatively, for larger degrees of decoupling, $M_T \ll M_B \gtrsim \mathcal{O}(10)$ TeV or $M_B \ll M_T \gtrsim \mathcal{O}(10)$ TeV, radiative corrections lead to $m_{\chi_1^\pm} < m_{\chi_1}$ when the remaining parameters are set to the values given in Fig. 2.3.

2.2.4 Indirect Detection

Constraints from searches for the annihilation products of dark matter are not particularly stringent in the class of models presented here. Gamma-ray observations of dwarf galaxies [113] and the Galactic Center [114] are currently only sensitive to thermal relics with masses below $\sim$100 GeV. Although measurements of the cosmic ray anti-proton spectrum can provide a competitive constraint over a similar mass range [115–117], interpretations of cosmic ray data currently involve significant astrophysical uncertainties.

In some of the parameter space considered here, the low-velocity dark matter annihilation cross section may experience non-negligible Sommerfeld enhancements, most notably boosting the annihilation rate to distinctive $\gamma\gamma$ and γZ final states. More specifically, if the dark matter is largely bidoublet-like, Sommerfeld enhancements can result from the couplings to the $W^{\pm}$, similar to the case of a Higgsino-like neutralino. Even with this enhancement, however, the predicted gamma-ray signal remains beyond the reach of current or next generation telescopes. Note that in none of the models discussed here does the dark matter experience a large Sommerfeld enhancement of the type predicted for a wino-like neutralino [118, 119] (as none of the models include a $SU(2)_L$ triplet).

2.2.5 Mechanism for Dark Matter Stability

Throughout this study, we have implicitly defined Lagrangians above the scale $v_R \sim 3-4$ TeV, which breaks $SU(2)_L \times SU(2)_R \times U(1)_{B-L}$ down to $SU(2)_L \times U(1)_Y$. Furthermore, the examples in Secs. 2.2.1-2.2.3 all possess an accidental parity symmetry, under which the fermions of the dark sector are odd. This can be understood from the fact that v_R breaks $U(1)_{B-L}$ down to a non-trivial $\mathbb{Z}_2$ subgroup, and as a result, the lightest new fermion with even $B-L$ is automatically stable [85].

However, above the scale v_R, this stabilizing symmetry need not be respected. In particular, new physics not contained in a minimal left-right symmetric model may generate interactions that allow for the lightest parity-odd fermion to decay. In this section, we outline a simple argument demonstrating that any new physics that respects $B-L$ and Lorentz invariance will not generate such processes as long as the $B-L$ charge of the dark matter multiplet is chosen appropriately.

We begin by assuming that the multiplet, X, is some fermionic dark matter gauge eigenstate, similar to the ones described in Sec. 2.2, with $B-L$ charge Q. The neutral component of X (χ) is assumed to be the cosmological dark matter. Gauge and Lorentz invariance dictate that χ may decay only through an operator of the form

$$O = X \times (\text{any \# of bosons}) \times (\text{odd \# of SM fermions}) \ . \tag{2.41}$$

Next, we let the quantity "(odd # of SM fermions)" consist of n_l SM lepton fields (each with $B-L = \pm 1$) and n_q SM quarks (each with $B-L = \pm 1/3$), and imagine that some subset of the lepton and/or quark fields cancel in $B-L$. We will denote the number of uncanceled leptons/quarks by $n'_{l,q}$. This cancellation can only take place among an even number of fields, and hence there are still an odd number of uncanceled SM fermions in the product. Furthermore, at or below the scale v_R, all the bosons of a left-right model are evenly charged under $B-L$. These two insights imply the following system of equations:

$$\begin{aligned} n'_l + n'_q &= 2n+1 \quad (\text{odd \# of SM fermions}) \\ Q + 2m + n'_l + \frac{1}{3}n'_q &= 0 \quad (B-L \text{ invariant}), \end{aligned} \tag{2.42}$$

where m and n are some integers. Solving for $n'_{l,q}$ yields:

$$\begin{aligned} n'_l &= \frac{-1}{2}(1+3Q+6m+2n) \\ n'_q &= \frac{3}{2}(1+2(m+n)+Q) \ . \end{aligned} \tag{2.43}$$

$n'_{l,q}$ are integers by definition, and hence the second line above implies that χ may only decay if $3Q$ is an odd integer. Therefore, we have shown that the lightest neutral component, χ, of a dark matter multiplet, X, is exactly stable, if X does *not* possess a $B-L$ charge of $Q = \pm(1,3,5,\ldots)/3$.

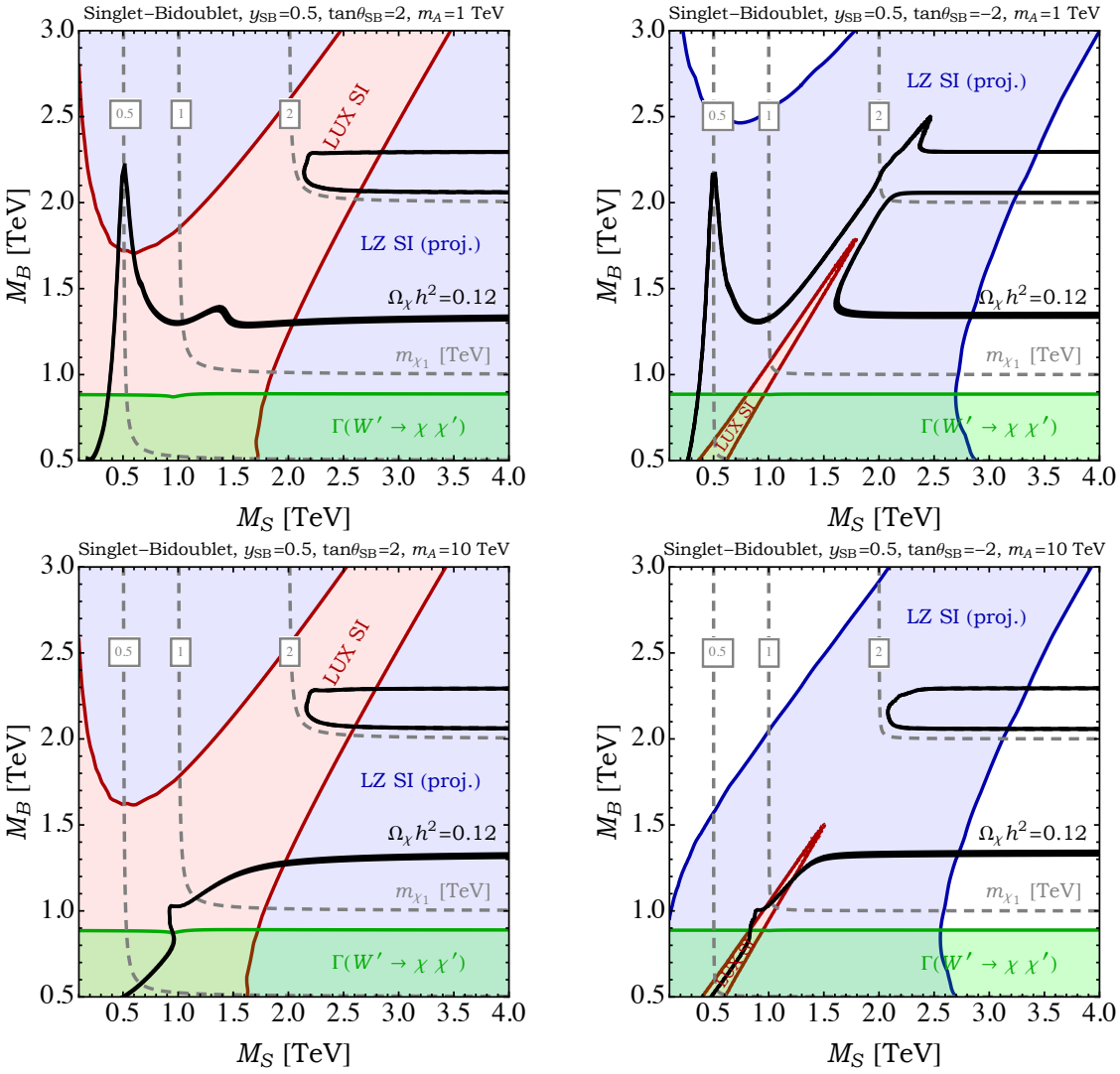

Fig. 2.2 Phenomenology of singlet-bidoublet dark matter. Along the solid black contours, the thermal relic abundance is in agreement with the measured cosmological dark matter density ($\Omega_\chi h^2 = 0.12$). Also shown as dashed grey lines are contours of constant dark matter mass (as labeled). In each frame, we have adopted $g_R = 0.45$ and $m_{W'} = 1.9$ TeV in order to match the rate and energy of the diboson excess, and $\tan\beta = 2$ to accommodate the required $W' \to WZ$ branching fraction. The red shaded regions are currently excluded by LUX, whereas the blue regions are predicted to fall within the reach of LZ. The green shaded regions are those in which the W' decays to particles residing within the dark matter sector with a branching fraction greater than 10%. In the figures on the left (both top and bottom), the ratio of the yukawas, $\tan\theta_{SB} = 2$ resulting in a larger cross-section, thus a large part of the parameter space is strongly constrained by the current LUX experiment and only a smaller part has the potential to be observed at the Future LZ. Only the parameter space on the black lines and in the blue shaded region will potentially be observed at LZ. The right figures represent a smaller scattering cross-section, thus a large part of the parameter space will evade current and future experiments.

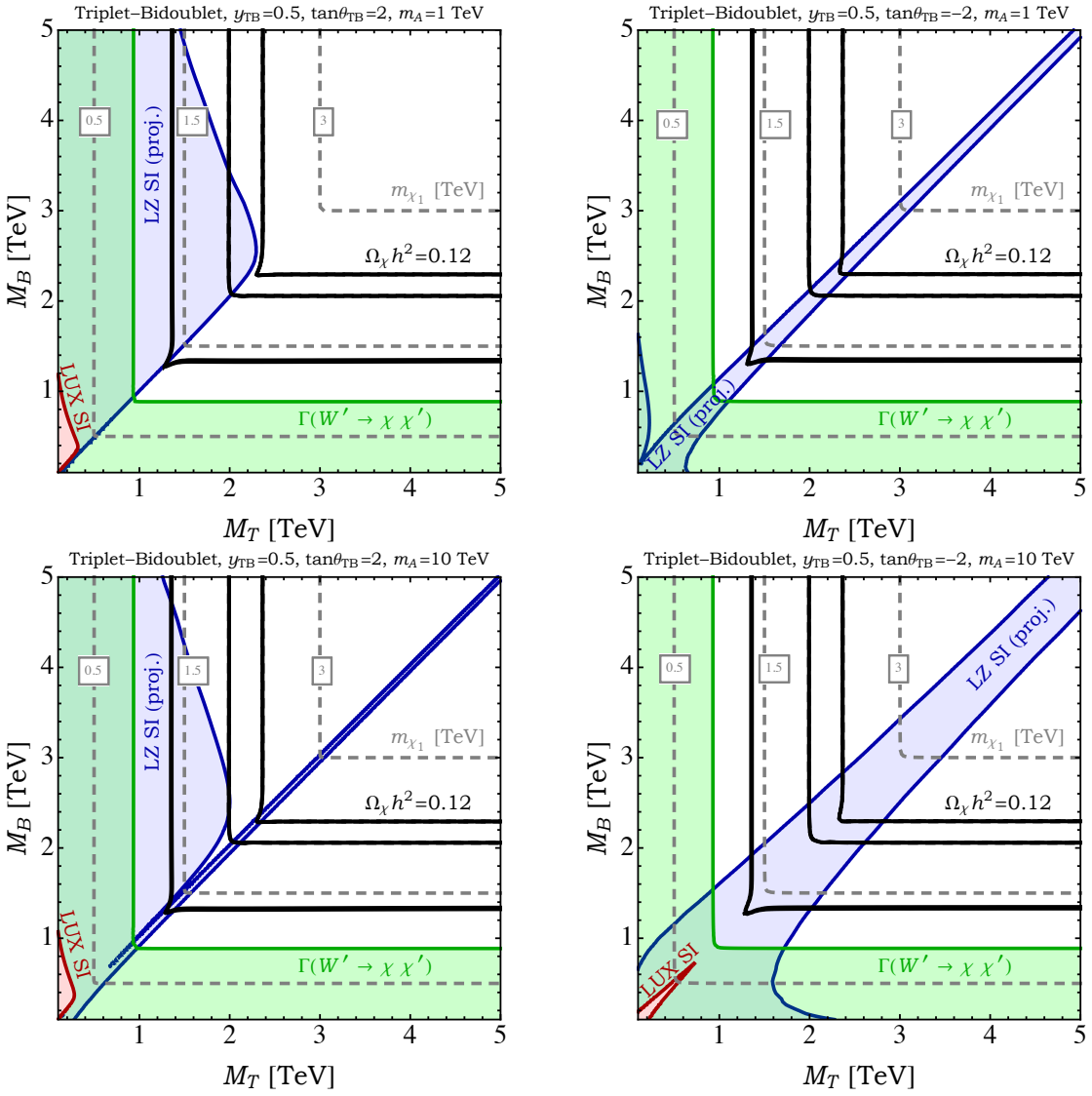

Fig. 2.3 Phenomenology of triplet-bidoublet dark matter. Along the solid black contours, the thermal relic abundance is in agreement with the measured cosmological dark matter density ($\Omega_\chi h^2 = 0.12$). Also shown as dashed grey lines are contours of constant dark matter mass (as labeled). In each frame, we have adopted $g_R = 0.45$ and $m_{W'} = 1.9$ TeV in order to match the rate and energy of the diboson excess, and $\tan\beta = 2$ to accommodate the required $W' \to WZ$ branching fraction. The red shaded regions are currently excluded by LUX, whereas the blue regions are predicted to fall within the reach of LZ. The green shaded regions are those in which the W' decays to particles residing within the dark matter sector with a branching fraction greater than 10%. For the figures on the left, i.e. with $\tan\theta_{TB} = 2$, destructive interference between the contribution of the SM Higgs and heavy CP-even Higgs result in smaller scattering cross-section, thus evading the projected sensitivity of LZ. In the figures on the right, there is constructive interference between the two Higgses, especially when the triplet and bidoublet have maximal mixing. This results in a larger cross-section in this region, meaning that LZ will be sensitive to this region. For this model, the allowed DM parameter space is the area on the black solid lines, outside the red region.

Chapter 3

Space-Time Extension of the Standard Model

A promising DM candidate is found in the minimal supersymmetric extension of the SM (MSSM) where the lightest supersymmetric particle, the neutralino, is the DM candidate. The full properties of DM sensitively depend on the detailed composition of the neutralino. For instance a neutralino may be formed dominantly of electroweakinos or Higgsinos or their mixtures, in certain proportions. In fact the singlet-triplet, singlet-bidoublet and triplet-bidoublet mixtures presented in the chapter 2 in many ways are phenomenologically analogous to bino-wino, bino-Higgsino, and wino-Higgsino dark matter in the MSSM, respectively. These two sets of DM scenarios result from models which are simple extensions of the SM. One is a gauge extension (as presented in chapter 2) while the other is a spatial extension (the MSSM).

Motivated by this abundant phenomenology, we consider in this chapter a model which has a somewhat one-to-one correspondence with the MSSM. However, we will focus on a non-SUSY extension in the form of Kaluza-Klein (KK) DM, arising in flat extra dimensions. A minimal KK DM has been discussed in universal extra dimension (UED) models [120] based on a TeV scale extra dimension [121] where the entire standard model (SM) particle content is assumed to be realized as the zero KK modes

of scalar, fermion, and gauge fields (with the SM field quantum numbers) which propagate on a space-time $\mathscr{M}_4 \times X$, where $\mathscr{M}_4$ is 4-dimensional Minkowski space and X is a compact flat space of extra dimension(s). In 4+1 dimensions, chiral zero mode fermions can be obtained when the extra dimensional space is taken to be the orbifold $S^1/\mathbb{Z}_2$ (or equivalently the interval $[-L,L]$ where $L = \pi R/2$ with the compactification radius R) which we focus on in this study.[1] In UED, all the SM fields are accompanied by their KK excitations with a mass gap of the order of the inverse compactification radius $1/R$. One of the attractive features of UED is KK parity conservation. KK parity is the reflection symmetry about the mid point of the extra dimension. It represents a geometric $\mathbb{Z}_2$ symmetry which is stable against quantum corrections and is thereby conserved if imposed at tree level [122, 123]. KK parity protects the lightest KK particle (LKP) from decay [27, 28, 124–126]. In minimal UED (MUED) [123], the first KK excitation of the photon[2] with a mass $M_1 = 1/R$ is the LKP.[3] The phenomenology of KK DM [26, 132–135] becomes much richer when bulk mass terms for fermions [136–141] and the boundary localized kinetic terms (BLKTs) [142–144] are allowed as in non-minimal UED (NMUED) [145–153]. We note that the boundary localized terms and the bulk mass terms are compatible with the Lorentz symmetry and the gauge symmetries of the model so that such terms should be included in the generic effective field theory action [146].

The presence of BLKTs for electroweak gauge bosons modifies the composition of the LKP, which appears as a mixture of KK excitations of the hyper-charge gauge boson, $B^{(1)}$ and the neutral component of the weak gauge boson $W_3^{(1)}$ [146]. This is different from MSSM, since no KK Higgs component is involved due to different spin of the KK partners of the KK Higgs as compared to KK gauge bosons. Several studies have considered the KK photon and the KK Z boson LKP separately as DM candidates [154–157]. Here, we consider generic mixing in electroweak KK DM sector and study various phenomenological aspects of KK DM in a more general framework of NMUED [4]. In MUED all the

[1] Fermions on $\mathscr{M}_4 \times S_1$ are vectorlike. However by orbifolding, half of the spinor degrees of freedom are projected out due to the boundary conditions imposed at the orbifold fixed points which results in a chiral zero mode for each fermion field after KK decomposition.

[2] Actually the LKP photon ($\gamma^{(1)}$) is very close to the KK excitation of the hypercharge gauge boson ($B^{(1)}$), because the weak mixing angle for the KK states are suppressed by a small factor $(m_W^2/m_{KK}^2) \ll 1$ [123].

[3] See Refs.[127, 128] for reviews on universal extra dimensions as well as Refs. [129–131] for the most recent LHC bounds on MUED.

[4] In this chapter we focus on DM in 5D models compactified on $S_1/\mathbb{Z}_2$. For DM in different compactifications and its

BLKTs are chosen to vanish at the cutoff scale and quantities at electroweak scale are obtained by renormalization group equations. In this study, we take the BLKTs as free parameters at the compactification scale instead. As a result, mixings and mass spectra are modified as compared to MUED.

This chapter is structured as follows: In section 3.1, we present the model of electroweak boson KK DM allowing BLKTs in NMUED and examine KK spectra and mixings among KK states. In section 3.2, we discuss current collider and precision measurement bounds on the given setup focusing on the effects of allowed four-Fermi operators, as well as collider constraints from the LHC. In section 3.3, we study the impact of BLKTs on the relic abundance of electroweak KK DM and on the direct detection rates taking the latest bounds into account.

3.1 Theoretical Framework

In this section we set up the model Lagrangian and discuss the KK decomposition of the electroweak KK bosons in the presence of BLKTs. We focus on mixings among KK weak gauge bosons. We will follow notations as in a recent review, Ref. [149].

3.1.1 Model Lagrangian

When we embed the SM in a five dimensional space $\mathscr{M}_4 \times [-L,L]$, the UED action is given in the following form:

$$S_5 = \int d^4x \int_{-L}^{L} dy \, [\mathscr{L}_V + \mathscr{L}_\Psi + \mathscr{L}_H + \mathscr{L}_{\rm Yuk}] \,, \tag{3.1}$$

where $y = \pm L$ are the orbifold fixed points, which are the boundaries of the fifth dimension. The kinetic energy of the gauge bosons and fermions propagating in $5D$ bulk are $\mathscr{L}_V$ and $\mathscr{L}_\Psi$. The Lagrangian for the Higgs boson and the Yukawa interactions with fermions are $\mathscr{L}_H$ and $\mathscr{L}_{\rm Yuk}$, respectively. The

phenomenology, see Refs. [29, 30, 158–164].

explicit form of each term is given as follows:

$$\mathscr{L}_V = \sum_{\mathscr{A}}^{G,W,B} -\frac{1}{4}\mathscr{A}^{MN}\cdot\mathscr{A}_{MN}\,, \tag{3.2}$$

$$\mathscr{L}_\Psi = \sum_{\Psi}^{Q,U,D,L,E} i\overline{\Psi}D_M\Gamma^M\Psi\,, \tag{3.3}$$

$$\mathscr{L}_H = \left(D_\mu H\right)^\dagger D^\mu H + \mu_5^2|H|^2 - \lambda_5|H|^4\,, \tag{3.4}$$

$$\mathscr{L}_{\text{Yuk}} = \lambda_5^E\overline{L}HE + \lambda_5^D\overline{Q}HD + \lambda_5^U\overline{Q}\tilde{H}D + \text{h.c.}\,, \tag{3.5}$$

where $\mathscr{A}$ denotes the five dimensional gauge bosons in the SM gauge group, i.e., the gluon (G), weak gauge bosons (W) and the hypercharge gauge boson (B). $D_M = \partial_M + i\hat{g}_3\lambda\cdot G_M + i\hat{g}_2\tau\cdot W_M + i\hat{g}_1 Y B_M$ is the gauge covariant derivatives, where the $\hat{g}_i$'s are the five dimensional couplings of the SM, and λ's and τ's are the generators of $\mathrm{SU}(3)_\mathrm{c}$ and $\mathrm{SU}(2)_\mathrm{W}$, respectively. The fermions, $\Psi = L,E,Q,D,U$ are Dirac spinors containing both chiralities in the KK decomposition as $\Psi(x,y) = \sum_n \psi_L^n(x)f_L^n(y) + \psi_R^n(x)f_R^n(y)$ where $\psi_{L/R}^n(x)$ is the n-th KK excitation mode with left-(right-) chirality, respectively and $f_{L/R}^n(y)$ is the corresponding KK basis function in the fifth dimension. The model is 5D Lorentz symmetric and the SM gauge symmetries are assumed as the internal symmetries. One should notice that the constructed Lagrangian is invariant under the inversion ($y \to -y$), such that the model respects the Kaluza-Klein parity (KK-parity). From the kinetic terms one can read out the mass dimensions of the fields and the coupling constants: $[\mathscr{A}] = [H] = \text{Mass}^{3/2}$, $[\Psi] = \text{Mass}^2$, $[\mu_5] = \text{Mass}$, $[\lambda_5^\Psi] = \text{Mass}^{-1/2}$ and $[\hat{g}_i] = \text{Mass}^{-1/2}$. The KK basis functions are dimensionful as $[f_{L/R}^n] = \text{Mass}^{1/2}$ and the KK modes are regarded as the conventional fields in 4D, $[\psi_{L/R}^n] = \text{Mass}^{3/2}$.

Notably, the 4D spacetime symmetry and the gauge symmetries of the model allow additional boundary localized operators. Even if the absence of such operators is assumed at tree level, they are induced by radiative corrections [122, 123], which shows that these operators cannot be forbidden by an underlying symmetry and their coefficients should thus be considered as additional parameters of the model which can only be calculated from the (so far unknown) UV completion of the model. If the

UV completion respects KK-parity, the boundary terms on the two orbifold fixed points are related.[1] In this study, we focus on the boundary localized terms for the electroweak gauge bosons respecting the KK-parity, the lightest combination of which would serve as dark matter:

$$S_{bdy} = \int d^4x \int_{-L}^{L} dy \left(-\frac{r_W}{4} W_{\mu\nu} \cdot W^{\mu\nu} - \frac{r_B}{4} B_{\mu\nu} B^{\mu\nu}, \right) \left[\delta(y-L) + \delta(y+L) \right], \tag{3.6}$$

where r_W and r_B are parameters describing the strength of the boundary localized terms and their mass dimensions are $[r_W] = [r_B] = \text{Mass}^{-1}$.

The boundary localized operators for the Higgs would affect the electroweak symmetry breaking in general but the KK state of the Higgs boson would not mix with electroweak gauge bosons because of the different spins. This makes a clear distinction from the MSSM where a neutralino is a mixture of higgsinos and electroweakinos.

The boundary localized terms modify the KK mass spectra and the KK wave functions of the electroweak gauge bosons, as will be worked out in detail in the next section. This in turn has important implications for the dark matter phenomenology: *(i)* Due to the modified masses of the electroweak gauge bosons at the first KK level, the UED dark matter candidate now becomes a linear combination of the $B^{(1)}$ and the $W^{3(1)}$ with the mixing angles determined by r_W, r_B, and R^{-1}, *(ii)* due to the modified wave functions, the couplings amongst the electroweak gauge bosons and the fermions (which follow from the overlap integrals of wave functions) are modified. Therefore the parameter space (r_W, r_B, R^{-1}) will be constrained by various tests such as electroweak precision measurement and collider searches.

In this study, we only focus on the boundary terms for electroweak gauge bosons. Therefore, our results by no means cover the entire NMUED parameter space, but rather show the main effects of changing the LKP from a $B^{(1)}$ to a $W^{3(1)}$ dark matter candidate, and its correlated implications for collider searches and precision bounds.

[1] Apart from KK parity conserving boundary terms, UED models can also contain KK parity odd fermion masses in the bulk whilst preserving KK parity in all interactions [136]. For studies of UED models with KK parity violating boundary terms *c.f. e.g.* [165–167].

3.1.2 Kaluza Klein Decomposition

KK masses and wave functions for the KK fermions, the KK gluon and the KK Higgs are given by the standard UED results (no boundary terms for these)

$$f^e(y) = \begin{cases} f^e_0 &= \sqrt{\frac{1}{2L}}\,, \\ f^e_{2n} &= \sqrt{\frac{1}{L}}\cos\frac{2ny}{R}\,, \quad , \\ f^e_{2n+1} &= \sqrt{\frac{1}{L}}\sin\frac{(2n+1)y}{R} \end{cases} \tag{3.7}$$

$$f^o(y) = \begin{cases} f^o_{2n+1} &= \sqrt{\frac{1}{L}}\cos\frac{(2n+1)y}{R}\,, \\ f^o_{2n} &= \sqrt{\frac{1}{L}}\sin\frac{2ny}{R}\,, \end{cases} \tag{3.8}$$

where f^e denote the KK wave functions of the $\mathbb{Z}_2$ even fields $G_\mu, Q_L, U_R, D_R, L_L, E_R, h$, and f^o denote the KK wave functions of the $\mathbb{Z}_2$ odd fields $G_5, Q_R, U_L, D_L, L_R, E_L$. The wave functions satisfy the normalization condition $\int_{-L}^{L} dy f^*_n f_m = \delta_{mn}$, and the masses are determined by $m^2_{\Phi^{(n)}} = (n/R)^2 + m^2_{\Phi^{(0)}}$, with the zero mode mass $m^2_{\Phi^{(0)}}$, given by the Higgs mechanism. Note that $[f^{e/o}] = \text{Mass}^{1/2} = \text{Length}^{-1/2}$, which is consistent with the Kronecker-delta normalization for orthonormal basis.

For the electroweak gauge bosons the boundary kinetic terms modify the wave functions. The KK decomposition of electroweak gauge bosons in the presence of boundary kinetic terms have been performed in Ref. [146]. Treating electroweak symmetry breaking as a perturbation, the gauge fields are decomposed as

$$W_\mu(x,y) = \sum_{n=0}^{\infty} W^{(n)}_\mu(x) f^W_n(y)\,, \tag{3.9}$$

$$B_\mu(x,y) = \sum_{n=0}^{\infty} B^{(n)}_\mu(x) f^B_n(y)\ , \tag{3.10}$$

where

$$f_n^{W/B}(y) = \begin{cases} \mathscr{N}_0^{W/B} & \text{if } n = 0, \\ \mathscr{N}_n^{W/B} \sin(k_n^{W/B} y) & \text{if } n = odd, \\ \mathscr{N}_n^{W/B} \cos(k_n^{W/B} y) & \text{if } n = even, \end{cases} \tag{3.11}$$

with the normalization factors

$$\mathscr{N}_n^{W/B} = \begin{cases} \frac{1}{\sqrt{2L(1+\frac{r_{W/B}}{L})}} & \text{if } n = 0, \\ \frac{1}{\sqrt{L+r_{W/B}\sin^2(k_n^{W/B}L)}} & \text{if } n = odd, \\ \frac{1}{\sqrt{L+r_{W/B}\cos^2(k_n^{W/B}L)}} & \text{if } n = even. \end{cases} \tag{3.12}$$

The wave numbers k_n are determined by

$$\begin{aligned} \cot(k_n^{W/B}L) &= r_{W/B}k_n^{W/B} \qquad \text{if } n = odd, \\ \tan(k_n^{W/B}L) &= -r_{W/B}k_n^{W/B} \qquad \text{if } n = even\,. \end{aligned} \tag{3.13}$$

Furthermore the wave functions satisfy the orthogonality relations

$$\int_{-L}^{L} dy f_m^{W/B} f_n^{W/B} \left[1 + r_{W/B}\left(\delta(y+L) + \delta(y-L)\right)\right] = \delta_{mn}. \tag{3.14}$$

Again $[f_n^{W/B}] = \text{Mass}^{1/2} = \text{Length}^{-1/2}$, which is consistent with our normalization conditions.

Finally, the effective 4D action of the electroweak gauge bosons is obtained after integrating over y:

$$
\begin{aligned}
S_{4D} \ni \int d^4x \quad & \left\{ \sum_n \left[-\frac{1}{4}\sum_n B^{(n)\mu\nu} B^{(n)}_{\mu\nu} - \frac{\left(k^B_n\right)^2}{2} B^{(n)\mu} B^{(n)}_{\mu} \right.\right. \\
& \left. -\frac{1}{4}\sum_n W^{(n)a\mu\nu} \cdot W^{(n)a}_{\mu\nu} - \frac{\left(k^W_n\right)^2}{2} W^{(n)a\mu} W^{(n)a}_{\mu} \right] \\
& + \sum_{m,n} \left[-\frac{\hat{g}_1^2 v^2}{8} \mathscr{F}^{BB}_{mn} B^{(m)\mu} B^{(n)}_{\mu} - \frac{\hat{g}_1 \hat{g}_2 v^2}{8} \mathscr{F}^{WB}_{mn} B^{(m)\mu} W^{(n)3}_{\mu} \right. \\
& \left.\left. -\frac{\hat{g}_2^2 v^2}{8} \mathscr{F}^{WW}_{mn} W^{(m)a\mu} W^{(n)a}_{\mu} \right] \right\},
\end{aligned}
\tag{3.15}
$$

where $\hat{g}_{1,2}$ and v are the 5D $\mathrm{U}(1)_Y$ and $\mathrm{SU}(2)_W$ gauge couplings and the vacuum expectation value. The mixing parameters are defined as

$$
\begin{aligned}
\mathscr{F}^{BB}_{mn} &= \int_{-L}^{L} \frac{dy}{2L} f^B_m(y) f^B_n(y), \\
\mathscr{F}^{BW}_{mn} &= \int_{-L}^{L} \frac{dy}{2L} f^B_m(y) f^W_n(y), \\
\mathscr{F}^{WW}_{mn} &= \int_{-L}^{L} \frac{dy}{2L} f^W_m(y) f^W_n(y),
\end{aligned}
\tag{3.16}
$$

where the normalization factor, $1/(2L)$, comes from the normalization factor of the zero mode Higgs vacuum expectation value. The resultant mass dimensions of the mixing parameters are $[\mathscr{F}^{VV'}_{mn}] = \text{Mass}$ for $V(V') = B$ or W. It should be noted that $\mathscr{F}^{BB}_{mn}$ and $\mathscr{F}^{WW}_{mn}$ are not orthogonal in our basis as they are orthogonal with respect to the scalar product as in Eq. (3.14) which includes the boundary parameters. The electroweak symmetry breaking terms having v^2 thus induce KK-mode-mixing in the basis we are using. Note that KK parity is still conserved so that even and odd modes do not mix.

We can separately analyze the mass matrices for KK even modes and odd modes. The matrix for even modes is relevant for tree level modifications of zero mode couplings as well as the couplings of the zero modes and the second (and higher even) KK modes. These are particularly important in Z'-like new gauge boson searches since the production and decay of $Z' = Z_2$ would be decided by the matrix. It is also important to consider 4-fermion operators among zero mode fermions, which are induced by even KK mode exchange. They can be probed by precision measurements, which will be analyzed in

section 3.2. The mass matrix for KK odd modes is particularly relevant for the DM physics since the nature and the structure of the couplings of the LKP (the lightest odd mode) is determined by the mass matrix.

3.1.3 Mass Matrices and Mixing Angles of KK Gauge Bosons

The mass matrix of the even-numbered neutral mass matrix in the $B^{(2n)}$ - $W^{3(2n)}$ basis reads

$$M^2_{n,e} = \begin{pmatrix} \frac{\hat{g_1}^2 v^2}{4}\mathscr{F}^{BB}_{00} & \frac{\hat{g_1}\hat{g_2}v^2}{4}\mathscr{F}^{BW}_{00} & \frac{\hat{g_1}^2 v^2}{4}\mathscr{F}^{BB}_{02} & \frac{\hat{g_1}\hat{g_2}v^2}{4}\mathscr{F}^{BW}_{02} & \cdots \\ \frac{\hat{g_1}\hat{g_2}v^2}{4}\mathscr{F}^{BW}_{00} & \frac{\hat{g_2}^2 v^2}{4}\mathscr{F}^{WW}_{00} & \frac{\hat{g_1}\hat{g_2}v^2}{4}\mathscr{F}^{BW}_{02} & \frac{\hat{g_2}^2 v^2}{4}\mathscr{F}^{WW}_{02} & \cdots \\ \frac{\hat{g_1}^2 v^2}{4}\mathscr{F}^{BB}_{20} & \frac{\hat{g_1}\hat{g_2}v^2}{4}\mathscr{F}^{BW}_{20} & \left(k^B_2\right)^2 + \frac{\hat{g_1}^2 v^2}{4}\mathscr{F}^{BB}_{22} & \frac{\hat{g_1}\hat{g_2}v^2}{4}\mathscr{F}^{BW}_{22} & \cdots \\ \frac{\hat{g_1}\hat{g_2}v^2}{4}\mathscr{F}^{BW}_{20} & \frac{\hat{g_2}^2 v^2}{4}\mathscr{F}^{WW}_{20} & \frac{\hat{g_1}\hat{g_2}v^2}{4}\mathscr{F}^{BW}_{22} & \left(k^W_2\right)^2 + \frac{\hat{g_2}^2 v^2}{4}\mathscr{F}^{WW}_{22} & \cdots \\ \vdots & \vdots & \vdots & \vdots & \ddots \end{pmatrix}. \tag{3.17}$$

We can further simplify the mass matrix by using the fact that the zero mode wave functions are flat. First, let us define

$$g_{1,2} = \hat{g}_{1,2}\mathscr{N}_0^{B,W}, \tag{3.18}$$

and the "normalized" and dimensionless overlap integrals

$$\tilde{\mathscr{F}}^{BB}_{mn} \equiv \frac{\mathscr{F}^{BB}_{mn}}{(\mathscr{N}_0^B)^2}\ ,\ \tilde{\mathscr{F}}^{WW}_{mn} \equiv \frac{\mathscr{F}^{WW}_{mn}}{(\mathscr{N}_0^W)^2}\ ,\ \tilde{\mathscr{F}}^{BW}_{mn} \equiv \frac{\mathscr{F}^{BW}_{mn}}{\mathscr{N}_0^B\mathscr{N}_0^W}. \tag{3.19}$$

Then the mass matrix can be rewritten as

$$M^2_{n,e} = \begin{pmatrix} \frac{g_1^2 v^2}{4} & \frac{g_1 g_2 v^2}{4} & \frac{g_1^2 v^2}{4}\tilde{\mathscr{F}}^{BB}_{02} & \frac{g_1 g_2 v^2}{4}\tilde{\mathscr{F}}^{BW}_{02} & \cdots \\ \frac{g_1 g_2 v^2}{4} & \frac{g_2^2 v^2}{4} & \frac{g_1 g_2 v^2}{4}\tilde{\mathscr{F}}^{BW}_{02} & \frac{g_2^2 v^2}{4}\tilde{\mathscr{F}}^{WW}_{02} & \cdots \\ \frac{g_1^2 v^2}{4}\tilde{\mathscr{F}}^{BB}_{20} & \frac{g_1 g_2 v^2}{4}\tilde{\mathscr{F}}^{BW}_{20} & \left(k^B_2\right)^2 + \frac{g_1^2 v^2}{4}\tilde{\mathscr{F}}^{BB}_{22} & \frac{g_1 g_2 v^2}{4}\tilde{\mathscr{F}}^{BW}_{22} & \cdots \\ \frac{g_1 g_2 v^2}{4}\tilde{\mathscr{F}}^{BW}_{20} & \frac{g_2^2 v^2}{4}\tilde{\mathscr{F}}^{WW}_{20} & \frac{g_1 g_2 v^2}{4}\tilde{\mathscr{F}}^{BW}_{22} & \left(k^W_2\right)^2 + \frac{g_2^2 v^2}{4}\tilde{\mathscr{F}}^{WW}_{22} & \cdots \\ \vdots & \vdots & \vdots & \vdots & \ddots \end{pmatrix}. \tag{3.20}$$

Now, performing a field rotation on the zero modes

$$U^\dagger = \begin{pmatrix} \cos\theta & \sin\theta & 0 \\ -\sin\theta & \cos\theta & 0 \\ 0 & 0 & \mathbb{1} \end{pmatrix}, \tag{3.21}$$

with $\tan\theta = g_1/g_2$, one obtains

$$UM^2_{n,e}U^\dagger = \begin{pmatrix} 0 & 0 & 0 & 0 & \dots \\ 0 & \frac{(g_1^2+g_2^2)v^2}{4} & \frac{g_1\sqrt{g_1^2+g_2^2}v^2}{4}\tilde{\mathscr{F}}^{BW}_{02} & \frac{g_2\sqrt{g_1^2+g_2^2}v^2}{4}\tilde{\mathscr{F}}^{WW}_{02} & \dots \\ 0 & \frac{g_1\sqrt{g_1^2+g_2^2}v^2}{4}\tilde{\mathscr{F}}^{BW}_{20} & \left(k_2^B\right)^2 + \frac{g_1^2v^2}{4}\tilde{\mathscr{F}}^{BB}_{22} & \frac{g_1g_2v^2}{4}\tilde{\mathscr{F}}^{BW}_{22} & \dots \\ 0 & \frac{g_2\sqrt{g_1^2+g_2^2}v^2}{4}\tilde{\mathscr{F}}^{WW}_{20} & \frac{g_1g_2v^2}{4}\tilde{\mathscr{F}}^{BW}_{22} & \left(k_2^W\right)^2 + \frac{g_2^2v^2}{4}\tilde{\mathscr{F}}^{WW}_{22} & \dots \\ \vdots & \vdots & \vdots & \vdots & \ddots \end{pmatrix}. \tag{3.22}$$

In this basis, the masslessness of the photon is explicitly seen. As it is a linear combination of $B^{(0)}$ and $W_3^{(0)}$, both of which in this basis have flat wave functions, the photon wave function is also flat as expected for a massless particle. At the same time we see that the zero mode of Z (and W as well) mixes with the even KK modes of the B and the W_3 in general.

In our phenomenological study for dark matter physics, the most relevant mass matrix is the mass matrix for the first KK excitation of neutral gauge bosons. The lightest odd state would be the candidate of the DM:

$$M^2_{n,odd} = \begin{pmatrix} \left(k_1^B\right)^2 + \frac{\hat{g_1}^2\hat{v}^2}{4}\mathscr{F}^{BB}_{11} & \frac{\hat{g_1}\hat{g_2}\hat{v}^2}{4}\mathscr{F}^{BW}_{11} & \dots \\ \frac{\hat{g_1}\hat{g_2}\hat{v}^2}{4}\mathscr{F}^{BW}_{11} & \left(k_1^W\right)^2 + \frac{\hat{g_2}^2\hat{v}^2}{4}\mathscr{F}^{WW}_{11} & \dots \\ \vdots & \vdots & \ddots \end{pmatrix}. \tag{3.23}$$

In the limit of vanishing boundary terms, $\mathscr{F}^{VV}_{nn}$ approaches the unity ($\mathscr{F}^{VV}_{nn} \to 1$ for $r_W \to 0$ and $r_B \to 0$). In addition to the terms from electroweak symmetry breaking, the boundary parameters play important roles here. They affect not only the overlap integrals $\mathscr{F}^{VV'}_{11}$ but also the value of the wave number k_1^B and k_1^W.

The contours of the two lightest electroweak KK gauge boson masses is shown in the left panel of

Fig. 3.1. We present the contour in the (r_B, r_W) plane for $R^{-1} = 1\,\text{TeV}$ as an example. The red solid contour lines are for the lighter level one mass eigenstate $A_1^{(1)}$ while the blue dashed contours are for the heavier $A_2^{(1)}$ state. When a boundary parameter (r_W or r_B) increases, the corresponding electroweak gauge boson becomes lighter. Thus the actual composition of the lightest mass eigenstate sensitively depends on the boundary parameters. In the right panel of Fig. 3.1 we present the level 1 KK Weinberg angle $\sin^2\theta_W^{(1)}$ as a function of r_W/r_B for $R^{-1} = 1\,\text{TeV}$ assuming $r_B/L = 0.5$.

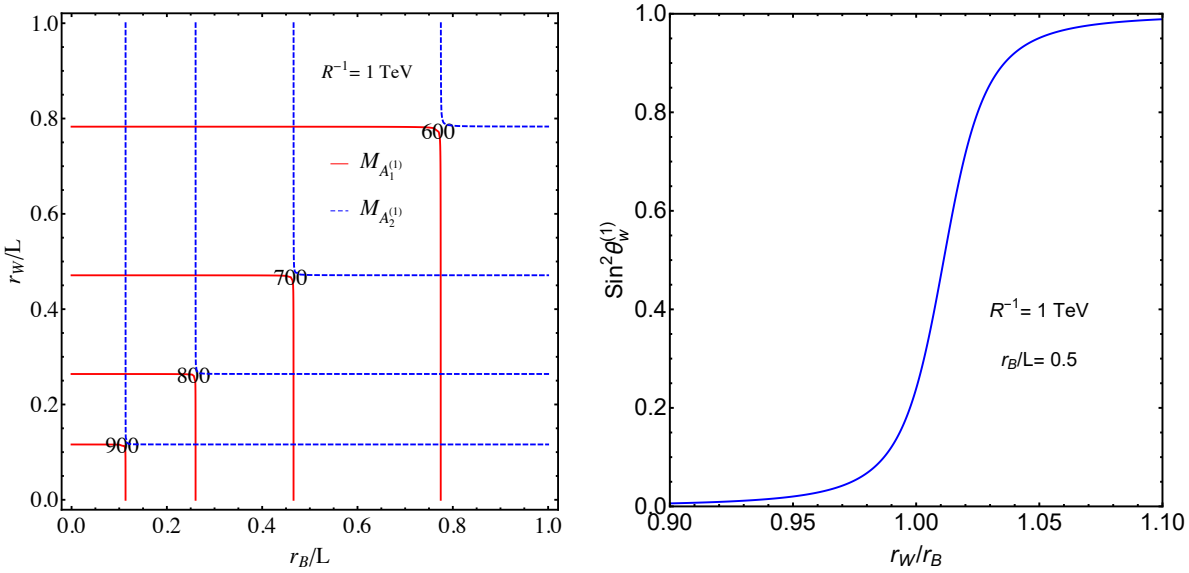

Fig. 3.1 Left: Contours of constant mass for the level 1 electroweak KK bosons $A_1^{(1)}$ and $A_2^{(1)}$. The contours were made assuming R^{-1} = 1 TeV, and they show the mass dependence on the boundary terms r_B and r_W. Right: The level 1 KK Weinberg angle $\sin^2\theta_W^{(1)}$ for R^{-1} = 1 TeV and $r_B/L = 0.5$. This illustrates how the KK Weinberg angle changes with the boundary terms.

We may classify the whole parameter space by three distinctive regions:

1. For $k_1^B \ll k_1^W$ (which occurs if $r_B \gg r_W$), the (11)-element of $M_{n,odd}^2$ is smaller than the (22)-element, but still much larger than the off-diagonal elements. The lightest eigenstate is almost purely $B^{(1)}$ and we have the "standard" MUED dark matter candidate.

2. For $k_1^B \gg k_1^W$ (which occurs if $r_B \ll r_W$), the (22)-element is smaller than the (11)-element, but still much larger than the off-diagonal elements. The lightest eigenstate is almost purely $W_3^{(1)}$ and we have what is normally referred to as a KK Z DM candidate, which is almost mass degenerate

with the $W_3^{(1)}$.[1]

3. For $k_1^B = k_1^W$ (which occurs if $r_B = r_W$), the contribution from the $\left(k_1^{B/W}\right)^2$ on the diagonal entries are identical, and as this part is proportional to the unit matrix, it does not contribute to the mixing angle. Then, the KK Weinberg angle is identical to the zero mode (and therefore the SM) Weinberg angle. In this case we have a mixture between the $B^{(1)}$ and the $W_3^{(1)}$ resulting in electroweak type KK gauge bosons, the lightest of which we call $A_1^{(1)}$ and is the DM candidate.

A notable feature here is that the Weinberg angle is almost always $\theta^{(1)} \approx 0$ or $\pi/2$ except the region of degenerate $r_W/r_B \approx 1$ where the transition takes place (see Fig. 3.1.) This feature is easily understood as the off-diagonal entries are relatively small ($\lesssim \mathcal{O}(v^2)$) compared to the diagonal entries ($\sim \mathcal{O}(1/R^2)$) so that a small difference in r_B and r_W easily induce an abrupt transition of the LKP from $W_3^{(1)}$-like to $B^{(1)}$-like or vice versa.

The mass spectrum and the properties of the mixing angle of the level 2 KK bosons are analogous to those for the first KK bosons as shown in Fig. 3.2 (left) where we present the contours for the mass eigenstates $A_1^{(2)}$ (the lighter 2nd KK EW boson) and $A_2^{(2)}$ (the heavier 2nd KK EW boson), respectively for a fixed compactification scale $R^{-1} = 1$ TeV. The Weinberg angle of the level 2 bosons, $\sin^2\theta_W^{(2)}$, is depicted in Fig. 3.2 (b). We can still observe the similar sharp transition near $r_W/r_B \approx 1$ as is expected from the similar underlying physics in the case for the level 1 EW bosons. We will discuss the detailed phenomenological implications in Sec. 3.2.2.

3.1.4 Coupling Between KK Bosons and Fermions

The couplings between KK gauge bosons and fermions are determined by a product of the corresponding SM coupling and the wave function overlap integral of the interacting particles ($\mathscr{A}^{(\ell)} - \psi^{(m)} - \psi^{(n)}$):

$$g_{\mathscr{A}^{(\ell)}\psi^{(m)}\psi^{(n)}} = g_{\mathscr{A}}\tilde{\mathscr{F}}^{\mathscr{A}}_{\ell mn} \tag{3.24}$$

$$\tilde{\mathscr{F}}^{\mathscr{A}}_{\ell mn} \equiv \frac{1}{\mathscr{N}_0^{\mathscr{A}}}\int_{-L}^{L} dy\, f_\ell^{\mathscr{A}}(y) f_m^{\psi}(y) f_n^{\psi}(y), \tag{3.25}$$

[1] The $W^{\pm(1)}$ mass always lies in between the masses of the two neutral eigenstates, such that the LKP is always neutral.

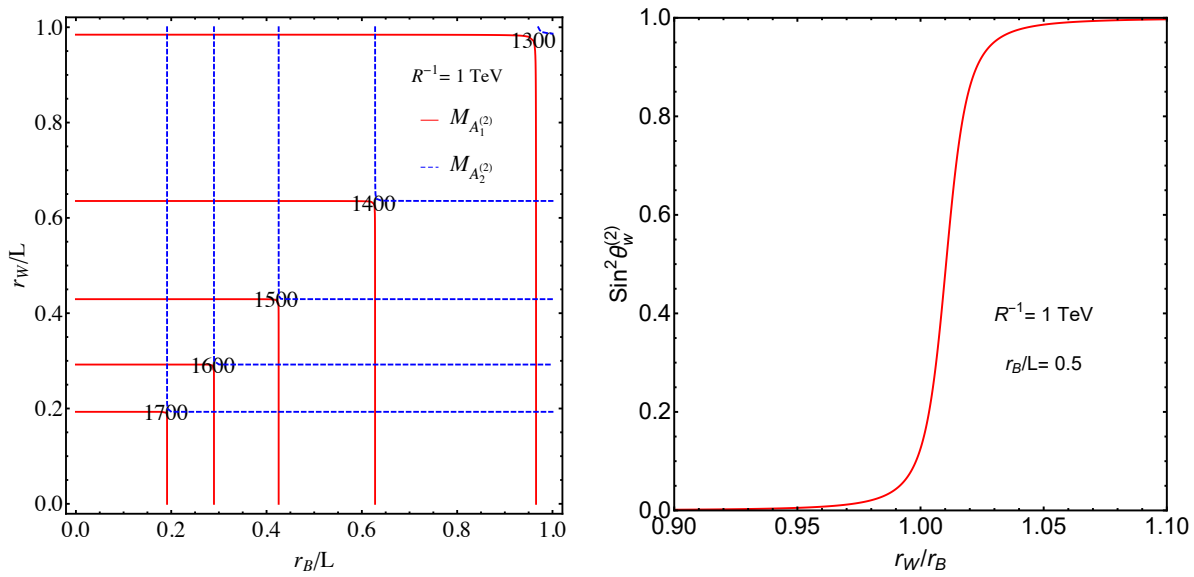

Fig. 3.2 Left: Contours of constant level 2 gauge boson masses for $R^{-1} = 1$ TeV. The red contours show the mass of the lighter eigenstate $A_1^{(2)}$ and the blue contour represents mass of heavier eigenstate $A_2^{(2)}$. Right: The level 2 KK Weinberg angle $\sin^2\theta_W^{(2)}$ for R^{-1} = 1 TeV and $r_B/L = 0.5$.

where $g_{\mathscr{A}}$ denotes g_1 or g_2, $\mathscr{N}_0^{\mathscr{A}}$ is normalization factor and $\tilde{\mathscr{F}}$ are the normalized overlap integrals in Eq. (3.18), which essentially describe the relative strength of the coupling constant with respect to the SM one. All KK number conserving interactions satisfy a 'sum-rule' $|\ell \pm m \pm n| = 0$. However, there are KK number violating interactions which only satisfy the rule from the KK parity conservation: $\ell + m + n \in \mathbb{Z}_{even}$.

Among those couplings, we are first interested in the KK number conserving interactions e.g., $\mathscr{A}^{(1)}\overline{\psi}^{(1)}\psi^{(0)}$. This interaction is particularly important in dark matter physics since the dark matter is identified as a level 1 EW gauge boson and it interacts with the SM fermion and its first KK excitation mode with the effective coupling constant

$$g_{\mathscr{A}^{(1)}\psi^{(1)}\psi^{(0)}} = g_{\mathscr{A}}\tilde{\mathscr{F}}^{\mathscr{A}}_{110}. \tag{3.26}$$

In Fig. 3.3 (left) we plot the effective couplings $g_{B^{(1)}\psi^{(1)}\psi^{(0)}}$ and $g_{W^{(1)}\psi^{(1)}\psi^{(0)}}$ with respect to the SM gauge couplings varying BLKT parameters r_B and r_W in the parameter range $(0, L)$. The (110) couplings

are reduced when the BLKTs get large.

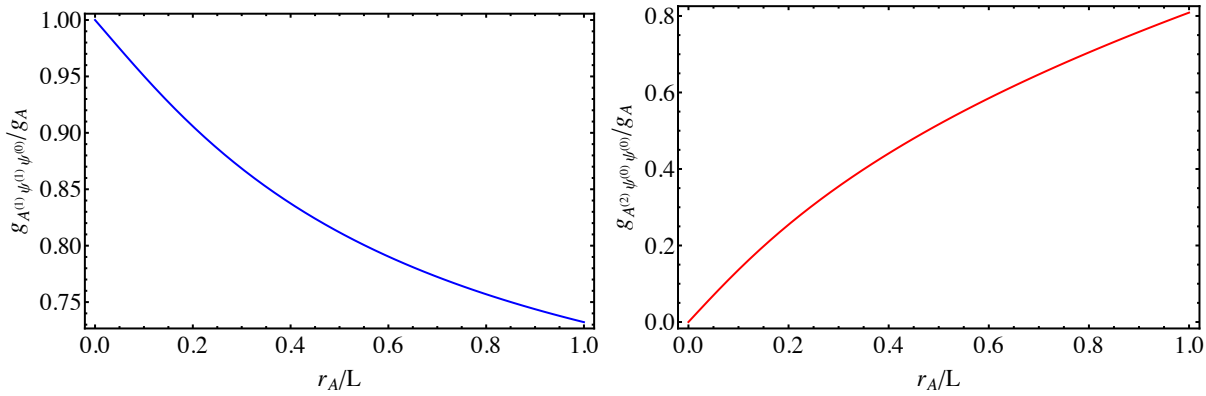

Fig. 3.3 Couplings of KK gauge bosons to fermions, normalized with respect to the Standard Model gauge couplings, as a function of the boundary parameter $r_{\mathscr{A}}$. Left: The KK number conserving coupling of a $U(1)_Y$ or $SU(2)$ first KK mode gauge boson to a first KK mode fermion and a Standard Model fermion ($\tilde{\mathscr{F}}^{\mathscr{A}}_{110}$ as defined in Eq. (3.26)). Right: The KK number violating interaction of a $U(1)_Y$ or $SU(2)$ second KK mode gauge boson to Standard Model fermions ($\tilde{\mathscr{F}}^{\mathscr{A}}_{200}$ as defined in Eq. (3.27)). Here A represents either B or W, depending on the gauge interaction.

There are also KK number violating but KK-parity conserving interactions induced by the couplings, e.g. :

$$g_{\mathscr{A}^{(2n)}\psi^{(0)}\psi^{(0)}} = g_{\mathscr{A}}\tilde{\mathscr{F}}^{\mathscr{A}}_{(2n)00}, \tag{3.27}$$

which are absent (at tree level) when the boundary terms vanish.

The non-vanishing couplings could be probed by the precision electroweak precision measurements and collider experiments: the even mode KK bosons mediate four fermion interactions via t-channel as well as s-channel diagrams. The induced four Fermi operators are subject to the on-going and future precision measurements. More directly, when BLKTs are sizable, the second level KK gauge bosons are to be produced in high energy collisions with sizable cross sections and they may appear as new heavy Z'-like resonances at the LHC. This is subject to resonance searches.

Before studying the phenomenological implications of BLKTs we wish to comment on the parameter choice in our scenario discussed here, as compared to the minimal UED scenario. In MUED, all boundary terms are assumed to be identical to zero at a cutoff scale Λ: $r_{W/B}(\mu = \Lambda) = 0$ and induced at

low scale through renormalization group (RG) running from Λ [123]. On the other hand, in the scenario we study in this chapter, we explicitly consider BLKTs as parameters at low scales, such as the first KK mode resonance scale, i.e., $r_{W/B} = r_{W/B}(\mu = k_1^{W/B})$ for DM phenomenology, such that we can directly compare our analysis with the low energy observables. As we are mostly interested in the lightest KK electroweak gauge bosons as a DM candidate in our study, we only consider the effects of $r_{W/B}$ but one may straightforwardly generalize our study by taking the non-vanishing BLKTs for fermions or the Higgs fields, which we reserve for the future.

3.2 Bounds from Collider Searches

In this section we consider experimental constraints on the BLKTs using electroweak precision data, namely from four Fermi-operators as well as results from resonance searches at the LHC.

3.2.1 Electroweak Precision Measurements

Electroweak precision tests (EWPT) provide stringent constraints on low scale KK masses [168–170]. In the presence of BLKTs, in particular, the KK electroweak (EW) gauge bosons would have tree level couplings with the SM fermions through KK-number violating but KK-parity conserving couplings so that they contribute to the four Fermi contact operators below the KK scale [171, 172]. It is convenient to parameterize the four Fermi operators following Ref. [173]:

$$\mathscr{L}_{eff} \supset \sum_{f1,f2} \sum_{A,B=L,R} \eta^{s}_{f_1 f_2,AB} \frac{4\pi}{(\Lambda^{s}_{f1f2,AB})^2} \overline{f}_{1,A} \gamma^{\mu} f_{1,A} \overline{f}_{2,B} \gamma_{\mu} f_{2,B}, \tag{3.28}$$

where $f_{1,2}$ are fermions (leptons or quarks), $\eta^s_{f1f2,AB} = \pm 1$ and $s = \pm$ are parameters for specific interaction patterns. The effective cutoff scale is given as

$$\begin{aligned}\frac{4\pi}{\Lambda^2_{eq,AB}}\eta_{eq,AB} &= 4\pi N_c\left[\sum_{n=1}^{\infty}(\tilde{\mathscr{F}}^B_{2n00})^2\frac{3}{5}\frac{\alpha_1 Y_{eA}Y_{qB}}{Q^2-M^2_{B^{(2n)}}}+\sum_{n=1}^{\infty}(\tilde{\mathscr{F}}^W_{2n00})^2\frac{\alpha_2 T^3_{eA}T^3_{qB}}{Q^2-M^2_{W_3^{(2n)}}}\right]\\ &\approx -12\pi\left[\sum_{n=1}^{\infty}(\tilde{\mathscr{F}}^B_{2n00})^2\frac{3}{5}\frac{\alpha_1 Y_{eA}Y_{qB}}{M^2_{B^{(2n)}}}+\sum_{n=1}^{\infty}(\tilde{\mathscr{F}}^W_{2n00})^2\frac{\alpha_2 T^3_{eA}T^3_{qB}}{M^2_{W_3^{(2n)}}}\right].\end{aligned} \tag{3.29}$$

The effective couplings are weighted by the factor $\tilde{\mathscr{F}}^{\mathscr{A}}_{2n00}$ which is the integrated wave function overlaps from $\mathscr{A}^{(2n)}\overline{\psi}^{(0)}\psi^{(0)}$ couplings in Eq. (3.27) with a color factor $N_c = 3$. The quantum numbers Y's and T's are the hypercharges and isospins of the interacting fermions (electron and quarks) and we take the one-loop improved values

$$\begin{aligned}\alpha_1(\mu) &= \frac{5}{3}\frac{g^2_Y(\mu)}{4\pi} = \frac{\alpha_1(m_z)}{1-\frac{b_1}{4\pi}\alpha_1(m_Z)\log\frac{\mu^2}{m_Z^2}},\\ \alpha_2(\mu) &= \frac{g^2_{ew}(\mu)}{4\pi} = \frac{\alpha_2(m_Z)}{1-\frac{b_2}{4\pi}\alpha_2(m_Z)\log\frac{\mu^2}{m_Z^2}},\end{aligned} \tag{3.30}$$

where $\alpha_1(m_Z)\approx 0.017, \alpha_2(m_Z)\approx 0.034$, and $(b_1,b_2) = (41/10,-19/6)$ below the compactification scale.

Equipped with the effective parameterization of four Fermi operators, we are now ready to compare with the experimental results. We take the updated results in PDG 2016 [172] as the reference values of experimental bounds. We summarize the relevant results in Table 3.1. The most stringent bound arises from the $e_Le_Lq_Lq_L$ interaction. Fig. 3.4 shows the bounds on R^{-1} in the $(r_W/L, r_B/L)$ plane. The most important ones are the results from *eeuu* and *eedd*. We draw the contours for various values of

Table 3.1 Four Fermi contact interaction bounds in TeV from PDG (2016) [172]

TeV	*eeee*	*ee*$\mu\mu$	*ee*$\tau\tau$	$\ell\ell\ell\ell$	*qqqq*	*eeuu*	*eedd*
Λ^+_{LL}	>8.3	>8.5	>7.9	>9.1	>9.0	>23.3	>11.1
Λ^-_{LL}	>10.3	>9.5	>7.2	>10.3	>12.0	>12.5	>26.4

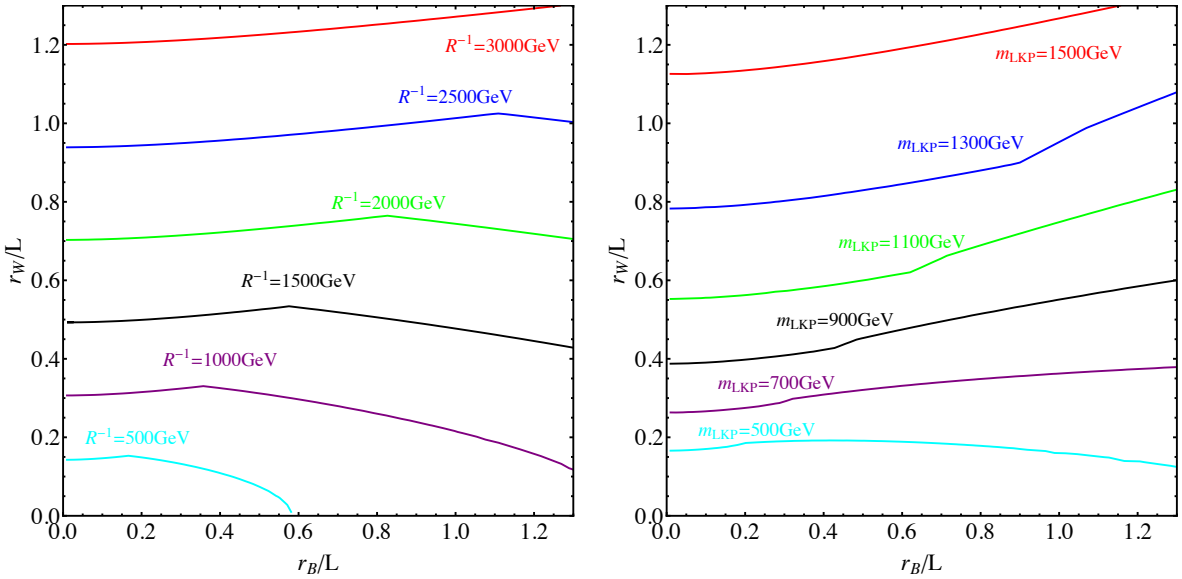

Fig. 3.4 Bounds on R^{-1} from four-Fermi contact interactions in r_B/L and r_W/L space. Left: Contours of minimally allowed values of R^{-1}. Right: Contours of minimally allowed values of m_{LKP}.

$R^{-1} \in (500, 3000)$ GeV (left) and the LKP mass, $m_{LKP} \in (500, 1500)$ GeV (right). The region above the line with a given R^{-1} (or m_{LKP}) is ruled out (thus the region below the line is allowed) because the effective couplings are too large. As expected, a larger parameter space is allowed for a large R^{-1} (and m_{LKP}) because of large suppression factors ($\sim 1/m_{LKP}^2$) in the effective operators. We notice that the bounds are more sensitive to the boundary parameter r_W rather than r_B mainly due to the large weak coupling compared to the hypercharge coupling. For example, above $m_{LKP} \approx 700$ (1100) GeV, essentially no stringent bound is found on r_B/L but only a restricted region $r_W/L \lesssim 0.3-0.4$ $(0.6-0.8)$ is allowed.

3.2.2 Dilepton Resonance Searches

The resonance searches at colliders are an effective way of probing BLKTs since the KK number violating interactions, e.g., $g_{\mathscr{A}^{(2)}\psi^{(0)}\psi^{(0)}}$ in Eq. (3.27), allow the single production of the second KK gauge bosons at particle collisions. When the 2nd EW gauge bosons are produced in high energy collisions, they decay to the SM particles which can be observed as a resonance. The production cross sections and the decay widths are all determined by the KK number violating couplings in Eq. (3.27). Here

we focus in particular on dilepton resonances because the Standard Model background is very low and the expected production cross sections are sizable. The dijet final state has a larger cross section in NMUED, but it is accompanied by a huge QCD background.

To determine the relevant couplings for mass eigenstates $A^{(2)}_{1,2}$ to the standard model fermions, we need to diagonalize the mass matrix in Eq. (3.22). The mass matrix at the second KK mode level reads

$$M^2_{n,2} = \begin{pmatrix} (k_2^B)^2 + \frac{g_1^2 v^2}{4}\tilde{\mathscr{F}}^{BB}_{22} & \frac{g_1 g_2 v^2}{4}\tilde{\mathscr{F}}^{BW}_{22} \\ \frac{g_1 g_2 v^2}{4}\tilde{\mathscr{F}}^{BW}_{22} & (k_2^W)^2 + \frac{g_2^2 v^2}{4}\tilde{\mathscr{F}}^{WW}_{22} \end{pmatrix}, \tag{3.31}$$

where $k_2^{B,W}$ follow from the mass quantization condition in Eq. (3.14). Wave function overlaps for $\mathscr{A}(\mathscr{A}') = B$ or W defined in Eq. (3.19) are

$$\begin{aligned} \tilde{\mathscr{F}}^{\mathscr{A}\mathscr{A}'}_{22} = & \sqrt{\frac{1+r_{\mathscr{A}}/L}{1+\frac{r_{\mathscr{A}}}{L}\cos^2(k_2^{\mathscr{A}}L)}}\sqrt{\frac{1+r_{\mathscr{A}'}/L}{1+\frac{r_{\mathscr{A}'}}{L}\cos^2(k_2^{\mathscr{A}'}L)}} \\ & \times\left[\frac{\sin((k_2^{\mathscr{A}}+k_2^{\mathscr{A}'})L)}{(k_2^{\mathscr{A}}+k_2^{\mathscr{A}'})L} + \frac{\sin((k_2^{\mathscr{A}}-k_2^{\mathscr{A}'})L)}{(k_2^{\mathscr{A}}-k_2^{\mathscr{A}'})L}\right]. \end{aligned} \tag{3.32}$$

For $\mathscr{A} = \mathscr{A}'$, the second term in the square parenthesis becomes 1:

$$\tilde{\mathscr{F}}^{WW}_{22} = \frac{1+r_W/L}{\frac{r_W}{L}\cos^2(k_2^W L)}\left[\frac{\sin(2k_2^W L)}{2k_2^W L}+1\right], \tag{3.33}$$

$$\tilde{\mathscr{F}}^{BB}_{22} = \frac{1+r_B/L}{1+\frac{r_B}{L}\cos^2(k_2^B L)}\left[1+\frac{\sin(2k_2^B L)}{2k_2^B L}\right]. \tag{3.34}$$

The mass matrix is diagonalized by a rotation by an angle $\theta_W^{(2)}$, the weak rotation angle for the 2nd level KK gauge bosons:

$$\begin{pmatrix} A_1^{(2)} \\ A_2^{(2)} \end{pmatrix} = U_n^{(2)}\begin{pmatrix} B^{(2)} \\ W_3^{(2)} \end{pmatrix} = \begin{pmatrix} \cos(\theta_W^{(2)}) & \sin(\theta_W^{(2)}) \\ -\sin(\theta_W^{(2)}) & \cos(\theta_W^{(2)}) \end{pmatrix}\begin{pmatrix} B^{(2)} \\ W_3^{(2)} \end{pmatrix}. \tag{3.35}$$

Interaction of the mass eigenstates and zero mode fermions are obtained from interaction of gauge

eigenstates ($W^{(2)}_{\pm,3}$ and $B^{(2)}$), which follows from the covariant derivative,

$$\begin{aligned}\mathscr{L} \supset \int dy \overline{\Psi} i \not{D} \Psi \quad \supset \quad & -g_{W^{(2)}\psi^{(0)}\psi^{(0)}} \overline{\psi}^{(0)} W_3^{(2)} T^3_{\psi_L} P_L \psi^{(0)} \\ & -g_{B^{(2)}\psi^{(0)}\psi^{(0)}} \overline{\psi}^{(0)} B^{(2)} (Y_{\psi_L} P_L + Y_{\psi_R} P_R) \psi^{(0)} \\ = \quad & -g_{W^{(2)}\psi^{(0)}\psi^{(0)}} \overline{\psi}^{(0)} \left(\sin(\theta_W^{(2)}) A_1^{(2)} + \cos(\theta_W^{(2)}) A_2^{(2)} \right) T^3_{\psi_L} P_L \psi^{(0)} \\ & -g_{B^{(2)}\psi^{(0)}\psi^{(0)}} \overline{\psi}^{(0)} \left(\cos(\theta_W^{(2)}) A_1^{(2)} - \sin(\theta_W^{(2)}) A_2^{(2)} \right) (Y_{\psi_L} P_L + Y_{\psi_R} P_R) \psi^{(0)},\end{aligned} \tag{3.36}$$

where

$$g_{W^{(2)}\psi^{(0)}\psi^{(0)}} = g_2 \int_{-L}^{L} \frac{dy}{2L} \frac{f_2^W(y)}{\mathscr{N}_0^W} = g_2 \sqrt{\frac{2(1+r_W/L)}{1+\frac{r_W}{L}\cos^2(k_2^W L)}} \frac{\sin(k_2^W L)}{k_2^W L}, \tag{3.37}$$

$$g_{B^{(2)}\psi^{(0)}\psi^{(0)}} = g_1 \int_{-L}^{L} \frac{dy}{2L} \frac{f_2^B(y)}{\mathscr{N}_0^B} = g_1 \sqrt{\frac{2(1+r_B/L)}{1+\frac{r_B}{L}\cos^2(k_2^B L)}} \frac{\sin(k_2^B L)}{k_2^B L}. \tag{3.38}$$

The ATLAS and CMS collaborations have searched for heavy narrow dilepton resonances at 13 TeV with 13.3 fb^{-1} (ATLAS) [174] and 13.0 fb^{-1}(CMS) [175] data, respectively. The experimental bounds are set in the combination of the production cross section of the heavy resonance particle and the branching fraction to dileptons, $\sigma \times BR(\ell\bar{\ell})$. The bounds are similar in both experiments. Here we use the ATLAS results, which are based on a slightly larger set of data. Since the relevant production cross sections and the branching fractions are given by three parameters $r_B/L, r_W/L$ and R^{-1}, we find the allowed parameter space in $(r_B/L, r_W/L)$ for various values of R^{-1}. In the left panel of Fig. 3.5 we show the ATLAS upper limit on $\sigma \times BR$ in the mass range $(1000, 5000)$ GeV and the expectations for the lighter level-2 KK gauge boson $A_1^{(2)}$ decaying to leptons. With a large compactification scale R^{-1}, a heavy dilepton resonance is expected so that a large parameter space in $(r_B/L, r_W/L)$ is allowed as shown in the right panel. For $R^{-1} = 2.4$ TeV, roughly $r_{\mathscr{A}}/L \lesssim 0.4$ is allowed for $\mathscr{A} = W, B$ but a smaller $R^{-1} = 1.5$ TeV for instance is compatible only with a smaller range $r_{\mathscr{A}} \lesssim 0.2$ or so. When comparing the results presented in Fig. 3.5 and Fig. 3.4, the LHC bound from the dilepton search is by far more stringent than the results from four-Fermi contact interactions. For the calculation of signal cross sections at leading order ($pp \to \mathscr{A} \to \ell\bar{\ell}$), we have used `CalcHEP` and `MG5_aMC@NLO` (Please see

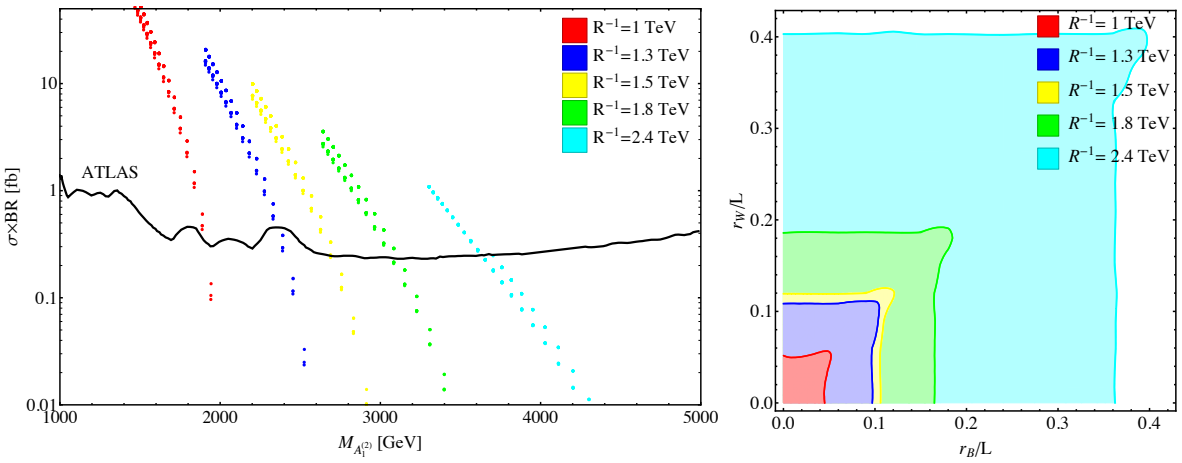

Fig. 3.5 Constraints from the 13 TeV ATLAS dilepton resonance search with 13.3 fb^{-1} luminosity [174], and bounds on the NMUED parameter space. Left: Constraints on the cross section times branching ratio to two leptons by ATLAS as a function of the resonance mass (black, solid). The model predictions for $A_1^{(2)}$ (lighter) resonance signals with $R^{-1} = 1, 1.3, 1.5, 1.8, 2.4$ TeV in the parameter window $(r_B/L \in (0,1), r_W/L \in (0,1))$ are given by scatter plots. Low values of r_B/L and r_W/L correspond to low cross sections. Right: Bounds on the NMUED parameter space from dilepton searches in the r_W/L vs. r_B/L plane. The red shaded region shows the allowed parameter space assuming $R^{-1} = 1$ TeV, corresponding to the values in red below the black line, in the left figure. The blue region is for $R^{-1} = 1.3$ TeV, the yellow region for $R^{-1} = 1.5$ TeV, the green region for $R^{-1} = 1.8$ TeV and the larger cyan region is for $R^{-1} = 2.4$ TeV.

Appendix for more information) with masses and couplings defined above.

While a dedicated study with double narrow resonance may provide more stringent bounds, we include the lighter level-2 KK gauge boson, $A_1^{(2)}$, in our analysis, since current ATLAS/CMS analysis assumes a single resonance in the dilepton channel. We assume that level-2 KK gauge bosons dominantly decay into SM fermion final states, and the decay width is computed automatically while scanning over $(r_B/L, r_W/L)$ for a given R^{-1}. Similar or slightly weaker bounds are obtained with the heavier KK gauge boson, $A_2^{(2)}$.

3.3 Phenomenology of Electroweak KK DM

Conventionally the KK photon has been regarded as a dark matter candidate in the literature. Here we focus on an LKP formed from a mixture of the first KK excitation of the hypercharge gauge boson

and the neutral component of the $SU(2)_W$ gauge boson. We have illustrated that when BLKTs are involved, mixing can show interesting features. In this section, we examine the phenomenology of the mixed LKP, dubbed as electroweak KK dark matter, while considering existing bounds on the BLKTs as discussed in the previous sections.

3.3.1 Relic Abundance

In section 3.1, we investigated the mass spectra and couplings of the KK electroweak gauge bosons in the presence of BLKTs. The masses, couplings and mixing angles sensitively depend on the BLKT parameters r_B and r_W. Therefore the annihilation cross-sections and the relic density ($\sim 1/\langle\sigma v\rangle$) are affected as well. The relevant interactions are

$$\mathscr{A}^{(1)}\psi^{(1)}\psi^{(0)} \quad \text{KK boson-KK fermion-SM fermion}, \tag{3.39}$$

$$\mathscr{A}^{(1)}\mathscr{A}^{(1)}H^{(0)}H^{(0)} \quad \text{KK boson-KK boson-Higgs-Higgs}, \tag{3.40}$$

$$\mathscr{A}^{(1)}\mathscr{A}^{(1)}\mathscr{A}^{(0)} \quad \text{KK boson-KK-boson-SM boson}, \tag{3.41}$$

where $\mathscr{A}$ collectively stands for the mass eigenstate of the KK electroweak gauge boson A_1 or A_2. As it is clearly seen in the left panel of Fig. 3.3, the couplings monotonically decrease as a function of BLKT parameters.

We compute the relevant couplings and identify DM candidate from the mass eigenstates, and then rescale MUED couplings for annihilation cross sections in Ref. [26]. KK fermions and KK Higgs masses are set to $\sqrt{\left(\frac{1}{R}\right)^2 + m_{SM}^2}$, since we include no boundary terms for them. For $r_W \sim r_B$, $A_1^{(1)}$ and $A_2^{(1)}$ are degenerate and therefore coannihilation processes are important. Since the mass of $W^{(1)\pm}$ is always between those of the two neutral gauge bosons, we include coannihilation processes with $A_2^{(1)}$, and $W^{(1)\pm}$ in addition to self-annihilation of $A_1^{(1)}$.

Our results are shown in Fig. 3.6, on the left figure as a function of the DM mass for various values of $(r_B/L, r_W/L)$. The red curve presents the relic density of the conventional DM candidate in MUED, which is the hypercharge gauge boson [27, 154]. In this case, the dominant annihilation final states are

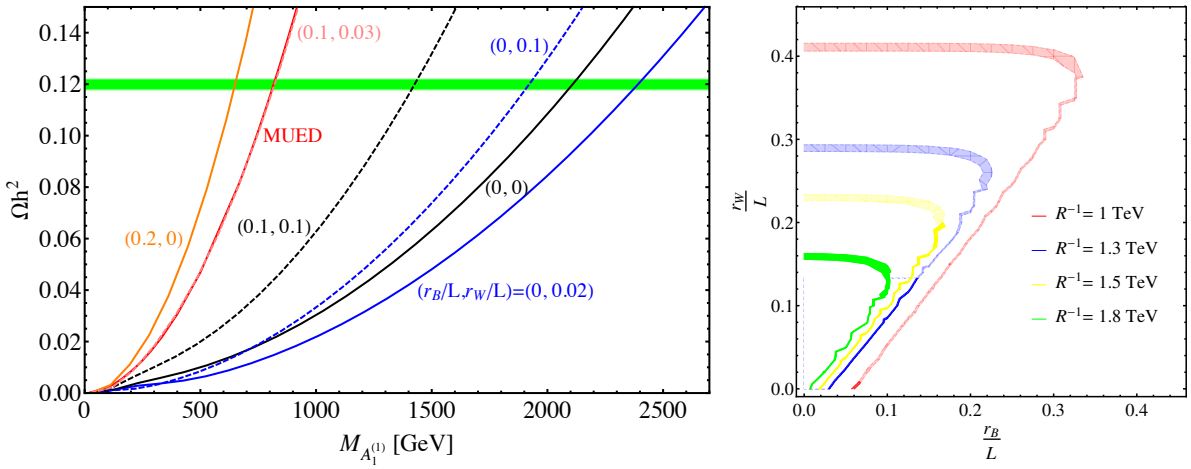

Fig. 3.6 Relic abundance of $A_1^{(1)}$ DM. On the left is the relic density Ωh^2 as a function of DM mass $M_{A_1^{(1)}}$ for given values of r_B/L and r_W/L. Different colors and line-styles indicate different (r_B, r_W) values. The green band indicates the desired $\Omega h^2 = 0.12$ from the result of Planck 2015 [176]. On the right are constraints from the relic density in the $(r_B/L, r_W/L)$ parameter space. The thickness of the contours corresponds to the thickness of the green band in the left figure, which indicates the uncertainties on the measured value of the relic density.

SM fermions with a small contribution from the Higgs-Higgs final state. With 1-loop corrected mass spectrum, the Weinberg angle at level-1 is very small and therefore there is no gauge boson final state [123]. We find the MUED results are reproduced with $(r_B/L, r_W/L) = (0.1, 0.03)$ which is shown as the pink dashed line.[1] The blue solid line shows a parameter choice which yields the maximum allowed value of the DM mass around 2.4 TeV. We indicate the observed relic abundance Ωh^2 from the Planck collaboration [176] in the green band. On the right we present relic density contours for different values of R^{-1} in the parameter space of the BLKT's.

Since the KK mixing angle changes rapidly in the vicinity of the line along $|r_B - r_W| = 0$ as can be seen in Fig. 3.1, the DM phenomenology is strongly altered when crossing this parameter region. For $r_W > r_B$, the main component of the LKP $A_1^{(1)}$ becomes $W_3^{(1)}$. Since the SU(2) coupling is stronger than the $U(1)_Y$, the annihilation cross section in this regime becomes greater than the value for the $B^{(1)}$-like

[1] The MUED line is understood as follows. In MUED, it is assumed that boundary parameters are all set to be zeroes as $(r_B/L, r_W/L)|_{\text{cut-off}} = (0,0)$ at the cut-off scale. After the renormalization group evolution, the non-zero boundary parameters are radiatively generated at the electroweak (EW) scale. Note again that for the rest of our study, we set the boundary parameters $(r_B/L, r_W/L)$ at the electroweak scale unless otherwise stated.

LKP, which implies that the observed relic density is reproduced at a much larger LKP mass. That is the reason why we get smaller LKP mass for $(r_B/L, r_W/L) = (0.2, 0)$ shown in the orange line in Fig. 3.6. However, if r_W/L is further increased, the size of effective gauge coupling becomes smaller and the LKP mass has to be reduced to compensate the effect. We find that the allowed upper limit on the LKP mass gets larger up to a critical point $r_W/L = 0.02$ and then drops down for a larger r_W/L. This feature is shown as blue solid line and blue dashed line in Fig. 3.6. The maximally allowed mass of the electroweak gauge boson LKP is about 2.4 TeV, which is significantly higher than the "naive" MUED value of 0.9 TeV for the KK photon LKP in MUED [154].

For $(r_B/L, r_W/L) = (0, 0.02)$, the masses of neutral KK bosons $A_1^{(1)}$, $A_2^{(1)}$ are 2.38 and 2.43 TeV, respectively. The lightest charged KK boson $W_1^{(1)}$ has a mass only slightly higher than the LKP and its contribution to the coannihilation is important, and is fully taken into account in our analysis. In passing, we would mention the potential enhancement of the annihilation cross section through the resonance of the 2nd KK excitation modes. It has been shown in MUED that 2nd KK resonance effects can greatly enhance the annihilation cross section so that the LKP mass could be as high as ~ 1.3 TeV [135]. However, the resonance effect becomes important only when the second KK mode masses ($m_{2\text{nd}}$) are very close to twice the mass of the first KK mode ($m_{1\text{st}}$). This relation between the first and second KK mode masses is satisfied in UED in the absence of boundary terms, but, as can be seen when comparing Figs. 3.1 (left) and 3.2 (left), in the presence of BLKTs, the second KK resonance is becoming heavier than twice the first KK resonance.

In Fig. 3.7 we show the parameter space for various values of $R^{-1} \in (1.0, 2.4)$ TeV, which is allowed by dilepton resonance searches (for $A_{1,2}^{(2)}$) and at the same time yields a relic density of $\Omega_{\text{DM}}h^2 < 0.12$ for the dark matter candidate $A_1^{(1)}$, such that $A_1^{(1)}$ does yield more than the observed DM. The bounds from LHC and from the dark matter relic density are complementary because a large BLKT induces a weak interaction strength thus a small annihilation cross section and a large relic abundance for a given R^{-1} but the resonance search result gives a weaker bound on $(r_B/L, r_W/L)$ plane for a larger R^{-1}. Thus from LHC searches, more parameter space in the (r_B/L, r_W/L) plane is allowed for larger values R^{-1} TeV, but the allowed parameter space shrinks back with a larger value of R^{-1} due to the relic density

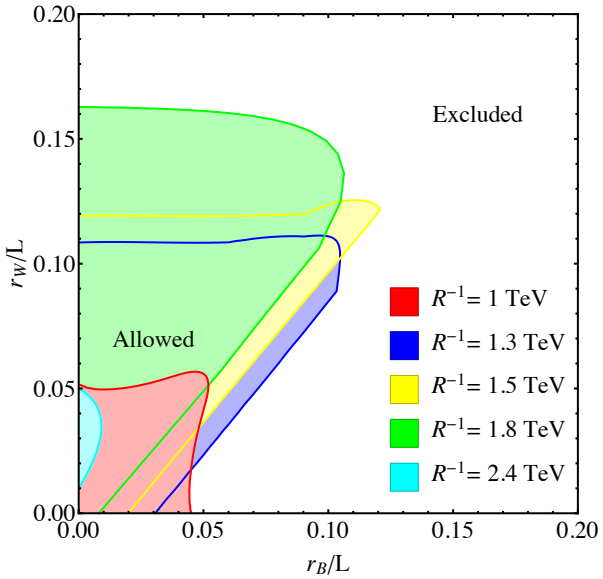

Fig. 3.7 Combined bounds from dilepton searches for $A_1^{(2)}$ and $A_2^{(2)}$ and from the relic density of the LKP in the r_W/L vs. r_B/L parameter plane. The shaded regions represent the allowed parameter space for various values of R^{-1}. Outside the shaded region, there would be too much dark matter produced, resulting in overclosure of the Universe, thus this region is excluded on this basis. The shaded areas indicate the right amount of DM produced. However, if we assume the LKP is the only DM component in the Universe, then we must lie on the edges of these contours for each value of the inverse radius.

constraints. For example for $R^{-1} = 2.4$ TeV (the sky blue region in Fig. 3.7) only small r_W/L and very small r_B/L are allowed by the combined bound.

3.3.2 Direct and Indirect Detection

Despite many ongoing searches with DM direct detection experiments, no firm signals of dark matter have been observed yet [47, 110, 111], and these experiments have set bounds on the scattering cross-section of dark matter. The elastic scattering of KK DM and nucleon is mediated by exchange of KK quark and the SM Higgs as shown in Fig. 3.8. The spin independent (SI) scattering cross-section is given as

$$\sigma_{SI} = \frac{M_T^2}{4\pi(M_{A_1^{(1)}} + M_T)^2}[Zf_p + (A-Z)f_n]^2, \tag{3.42}$$

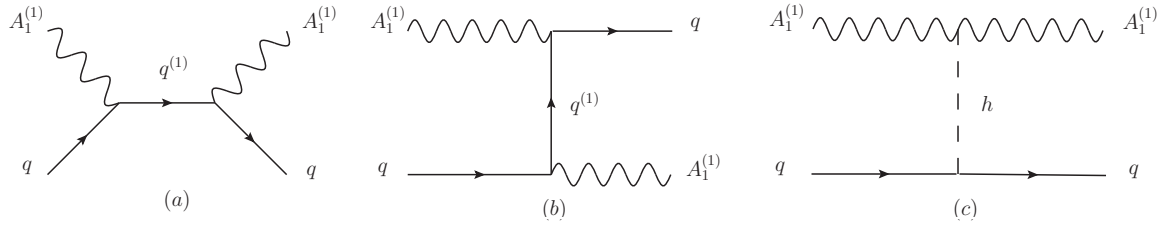

Fig. 3.8 Tree level diagrams for the elastic scattering of $A_1^{(1)}$ with quarks. In figures (a) and (b) scattering occurs through the level 1 KK quark and in figure (c) through the SM Higgs.

where M_T is the target nucleus mass, Z and A are the atomic number and atomic mass of the target respectively. The elastic scattering form factor for the nucleon is given by

$$f_{p/n} = \sum_{u,d,s} \frac{(\beta_q + \gamma_q)}{M_q} M_{p/n} f_{T_q}^{p/n}, \tag{3.43}$$

where $M_{p/n}$ is the mass of the proton(neutron) and M_q is the light quark mass. We adopt the nucleon matrix elements from Ref. [177] in our analysis. The dominant contribution to the nucleon form factors is from light quarks, whereas the heavier quarks (c,b,t) contribute through the gluon form factor, given as $f_{T_G}^{(p/n)} = 1 - \sum_q f_{T_q}^{(p/n)}$ but the effects are suppressed [178].

The β_q encapsulates the contributions from the left and right handed KK quarks as depicted in Fig. 3.8 (a) and (b) and γ_q from the Higgs (Fig. 3.8 (c)):

$$\begin{aligned}
\beta_q &= M_q (\cos\theta_W^{(1)} g_{B^{(1)}\psi^{(1)}\psi^{(0)}})^2 \left[Y_{q_L}^2 \frac{M_{A_1^{(1)}}^2 + M_{q_L^{(1)}}^2}{\left(M_{q_L^{(1)}}^2 - M_{A_1^{(1)}}^2\right)^2} + Y_{q_R}^2 \frac{M_{A_1^{(1)}}^2 + M_{q_R^{(1)}}^2}{\left(M_{q_R^{(1)}}^2 - M_{A_1^{(1)}}^2\right)^2} \right] \\
&+ M_q (\sin\theta_W^{(1)} g_{W^{(1)}\psi^{(1)}\psi^{(0)}})^2 \left[\frac{1}{4} \frac{M_{A_1^{(1)}}^2 + M_{q_L^{(1)}}^2}{\left(M_{q_L^{(1)}}^2 - M_{A_1^{(1)}}^2\right)^2} \right], \qquad (3.44) \\
\gamma_q &= \frac{M_q [(\cos\theta_W^1 g_{B^{(1)}B^{(1)}\phi^{(0)}})^2 + (\sin\theta_W^1 g_{W^{(1)}W^{(1)}\phi^{(0)}})^2]}{2M_h^2}, \qquad (3.45)
\end{aligned}$$

where $M_h \simeq 125$GeV is the SM Higgs mass. $g_{V^{(1)}\psi^{(1)}\psi^{(0)}}$ is the gauge coupling of the respective level 1 gauge boson V with fermions as defined in Eq. (3.26) and $g_{V^{(1)}V^{(1)}\phi^{(0)}}$ is the coupling of the gauge bosons

with the SM Higgs. $Y_{q_{L/R}}$ are the values of the hypercharges of the SM quarks, with the convention $Y_i = Q_i - T_i^3$, Q_i and T_i^3 being the electric charge and weak isospin respectively. $\theta_W^{(1)}$ is the level 1 KK Weinberg angle and $M_{q_{L/R}^{(1)}}$ is the mass of the level 1 KK quark introduced in Fig 3.8. The mass gap between the KK quark and dark matter masses are parameterized by

$$\delta_q = \frac{M_{q^{(1)}} - M_{A_1^{(1)}}}{M_{A_1^{(1)}}} \approx \frac{1 - RM_{A_1^{(1)}}}{RM_{A_1^{(1)}}},$$

where we used the approximate relation $M_{q^{(1)}} \approx 1/R$.

The spin-dependent cross-section is given by

$$\sigma_{SD} = \frac{M_T^2}{6\pi \left(M_{A_1^{(1)}} + M_T\right)^2} J_N(J_N+1) \left[\sum_{u,d,s} \alpha_q \lambda_q\right]^2, \tag{3.46}$$

with α_q and λ_q given as

$$\begin{aligned} \alpha_q \;=\; 2 \Bigg[& (\cos\theta_W^{(1)} g_{B^{(1)}\psi^{(1)}\psi^{(0)}})^2 \left(\frac{Y_{q_L}^2 M_{A_1^{(1)}}}{M_{q_L^{(1)}}^2 - M_{A_1^{(1)}}^2} + \frac{Y_{q_R}^2 M_{A_1^{(1)}}}{M_{q_L^{(1)}}^2 - M_{A_1^{(1)}}^2} \right) \Bigg] \\ & + \; (\sin\theta_W^{(1)} g_{W^{(1)}\psi^{(1)}\psi^{(0)}})^2 \left(\frac{M_{A_1^{(1)}}}{M_{q_L^{(1)}}^2 - M_{A_1^{(1)}}^2} \right), \end{aligned} \tag{3.47}$$

$$\lambda_q \;=\; \Delta_q^p \frac{\langle S_p \rangle}{J_N} + \Delta_q^n \frac{\langle S_n \rangle}{J_N}, \tag{3.48}$$

where $\Delta_q^{p/n}$ is the fraction of the nucleon spin carried by the quark, for which we use the values from Ref. [177]. The ratio $\langle S_{p/n} \rangle / J_N$ is the fraction of the total nuclear spin carried by the spin of the nucleon, J_N being the total nuclear spin. Direct detection experiments commonly present their constraints in terms of effective WIMP-nucleon cross sections for which λ_q reduces to $\Delta_q^{p/n}$.

In Fig. 3.9, on the left, we show the spin independent scattering cross section within the parameter space, which is fully compatible with the currently available experimental results from EWPT, KK

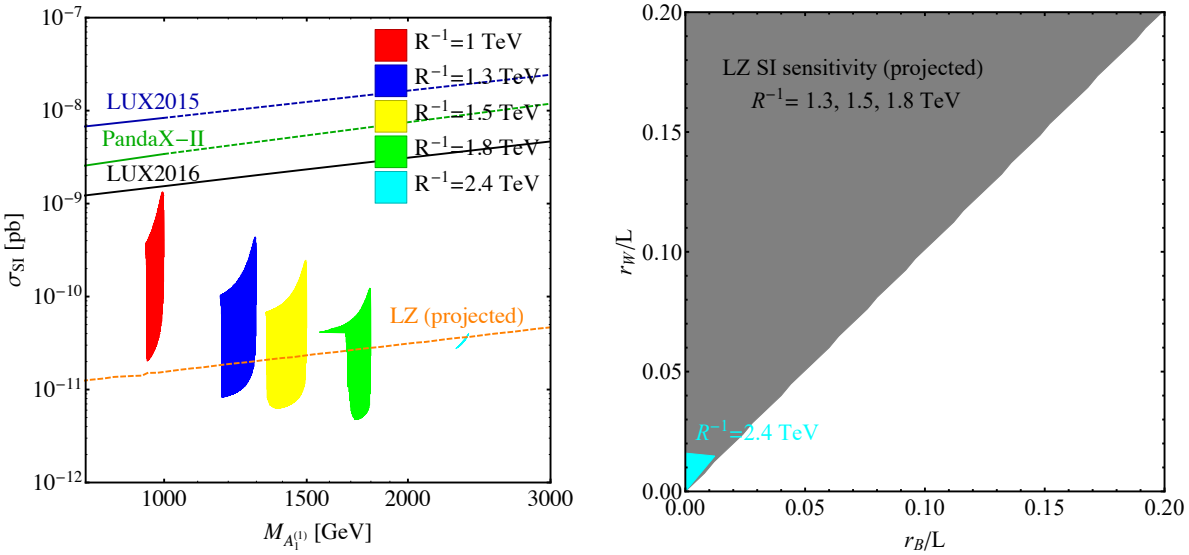

Fig. 3.9 The expected SI cross sections (σ_{SI}) are plotted for various values of R^{-1} ranging from 1 TeV to 2.4 TeV. For each R^{-1}, we vary $(r_B/L, r_W/L)$ (on the left) and present in the $(r_B/L, r_W/L)$ parameter space (on the right) within the allowed parameter regions from Fig. 3.7 in order to obtain the predicted regions of σ_{SI}. Current exclusion limits are set by LUX [110] (dark blue and black) and PandaX-II [47] (dark green). The expected sensitivity of LZ (orange) is found in Ref. [111]. The LZ projected sensitivity would cover the entire remaining parameter space for $R^{-1} = 1$ TeV. A large part of the parameter space in $(r_B/L, r_W/L)$ is within the testable range for a larger value of R^{-1}, too. In the right figure, the region of parameter space that may be probed by the LZ experiment for the larger values of R^{-1} are represented by the black shaded region, while $R^{-1} = 2.4$ TeV is shown as the blue shaded region, which has the potential to be seen at LZ, the rest of the space may be probed by experiments beyond LZ.

resonance searches and the right relic abundance of DM. The expected cross sections are represented in the regional plots with different colors corresponding to a given value of R^{-1}: 1 TeV (red), 1.3 TeV (blue), 1.5 TeV (yellow), 1.8 TeV (green) and 2.4 TeV (sky blue) from left to the right. The expectations are compared with the limit on the spin independent dark matter-proton scattering cross-section from the latest LUX result [110] and also from the PandaX-II result [47]. Current experiments are not quite sensitive enough to probe DM masses above 1 TeV. We also present the projected sensitivity limit from LUX-Zeplin (LZ), 3×10^{-48}cm^2, which is based on the estimation of a 3 year run with 6000 kg fiducial mass [111]. It is encouraging to notice that the future LZ sensitivity region would cover the full parameter space for $R^{-1} \leq 1$ TeV and also quite large portions of the parameter spaces for heavier

DM above 1.3 TeV. On the right we present the SI projected sensitivity for the LZ experiment in the $(r_B/L, r_W/L)$ parameter space. We present the values of R^{-1} from 1.3 TeV to 1.8 TeV in grey as they roughly overlap in this parameter space, while the cyan region is reserved for $R^{-1} = 2.4$ TeV.

In Fig. 3.10, we present the remaining parameter space after taking the complementary constraints from the collider search and also the relic abundance calculation for $R^{-1} = 1.3, 1.5, 1.8$ and 2.4 TeV, respectively. The expected coverage of the 3 year run at LZ is shaded by grey. It is clear that LZ can probe almost the entire parameter space which is compatible with current experiments. Thus, the DM direct detection experiments will play an important complementary role to the LHC searches and other future experiments in the search for KK DM.

Finally, we comment on indirect signals of electroweak KK DM. First, the mass of KK DM (which is likely to be heavier than 1 TeV or even higher but still less than 2.4 TeV) is rather high compared to the range of energies $\lesssim$ a few $\times \mathcal{O}(100)$ GeV considered in the recent Gamma-ray studies of Dwarf galaxies and of the milky way galactic center [114]. Other cosmic ray measurements could in principle provide constraints on heavier masses but these observations currently involve large astrophysical uncertainties [115, 117]. We have noticed several studies in this line: Refs. [179–182] study photon lines (and continuous photon background) from UED models, partially with $B^{(1)}$, partially with Z' DM. We therefore do not include the Sommerfeld effect in our analysis here and reserve a detailed analysis for future studies.

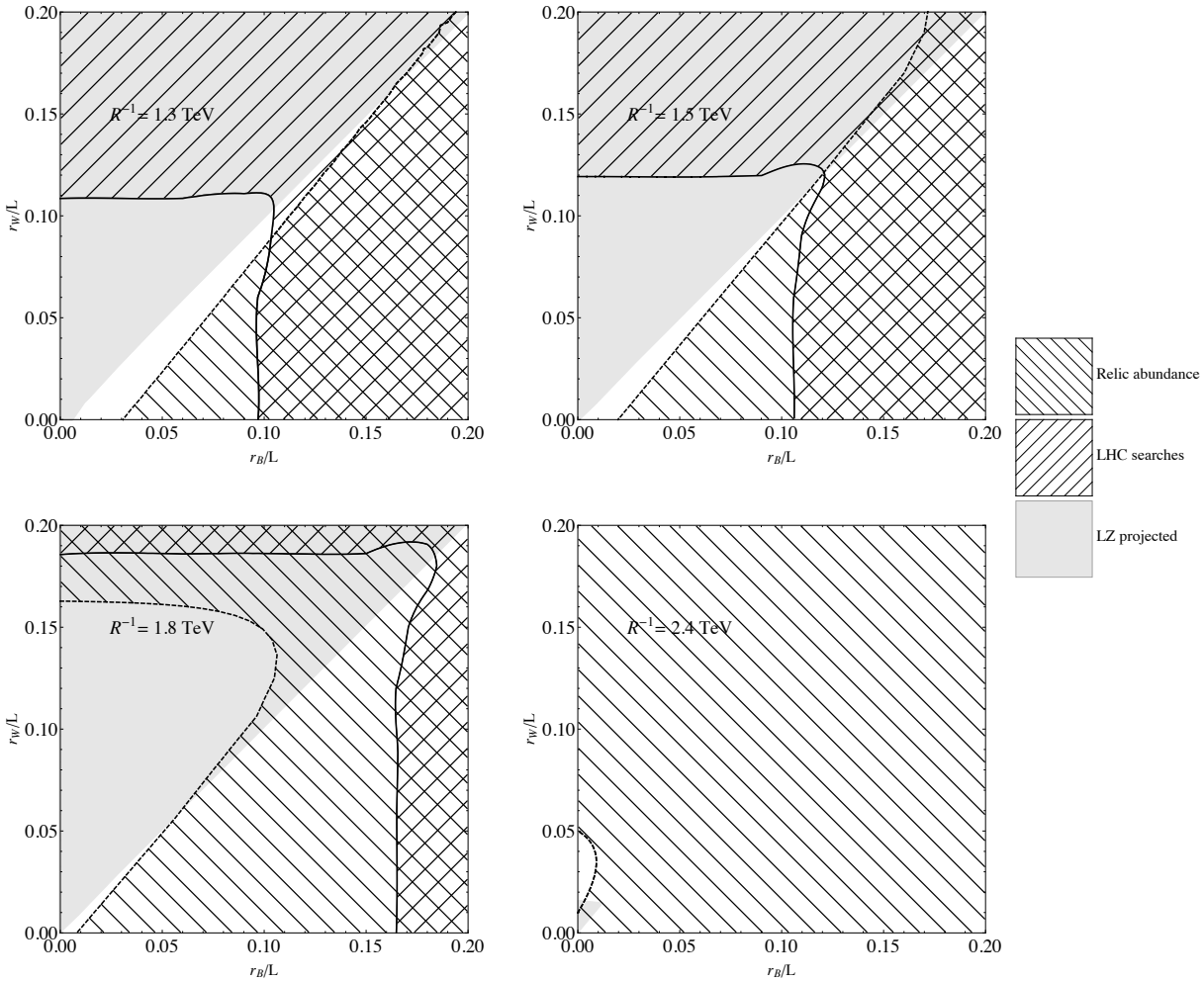

Fig. 3.10 Combined constraints from relic abundance (left hatched), LHC collider search (right hatched) and LZ projected direct detection sensitivity (grey shaded) for $R^{-1} = 1.3, 1.5, 1.8, 2.4$ TeV in $(r_B/L, r_W/L)$ plane. The solid curves are limits from LHC collider search and the dashed curves are limits from relic abundance. Here we combine all constraints on one figure, for each value of the radius. This is to illustrate the complementarity of the different search strategies. In all the figures, anywhere outside the dashed contour, the Universe is overclosed, this this region is excluded. For the lower values of R^{-1}, the region outside the square area in the lower left is excluded due to dilepton resonance searches. DM may lie in within the dashed contours and the solid black square contours.

Part II

Model Independent Framework

The large number of possible models available make the characterization of dark matter properties very challenging. The lack of a clear DM signal forces us to interpret our experimental data by placing bounds on how DM may interact with the SM. It is particularly difficult to do this based on specific models, as these require many assumptions and are dependent on many parameters. Ideally model independent methods are free of such constraints and allow for the study of DM in a general, all inclusive manner.

The purpose of this part of the dissertation is to present a parallel framework of studying dark matter. In this framework, we focus on exploring a potential signal of DM without worrying about the underlying complete model. The main purpose is to study this potential physics signal and determine which experiments would be most sensitive to it. We consider a minimal effective field theory involving two dark matter particles. For the purpose of the study we assume the two dark matter particles are fermions and we assume that they interact via a contact four-fermion operator. We assume that one particle is much heavier than the other and is more dominant in the Universe, i.e. forms most of the relic abundance of DM in the Universe. We also assume that the heavier particle is secluded from the SM and may only talk to the SM through the lighter particle. The heavier particle may accumulate in the center of the galaxy or the Sun and annihilate into its smaller counterpart. The large mass difference between the two means that the smaller particles will be boosted and travel relativistically to the Earth where they can scatter off SM particles inside detectors on the Earth.

For this study, we first discuss the interactions between the two DM states in the dark sector as well as the interaction of the boosted particles with the SM sector. We then calculate the relic abundance of DM for the two DM states, assuming the heavier partner is the most dominant. We then match our calculated relic abundance to the observed relic abundance in the Universe. Since the interaction of the boosted particles with the SM particles occurs through scattering, we calculate the scattering cross-section of the boosted DM off electrons. Boosted DM may scatter off nucleons as well, but for purposes of this study we focus on electron scattering. We then focus on the experimental details, discussing the properties of the detectors we would like to study and the possible background sources

that might overwhelm or mimic our potential DM signal. After understanding the possible backgrounds we could have, we discuss the sources of boosted DM. We then calculate the flux from each source after annihilation of the heavier partner as well as the number of signal counts we may observe in the detectors we are considering.

We investigate boosted DM coming from the center of our Galaxy, the center of the Sun and from the Earth. We find that we have a higher potential to observe boosted DM coming from the Sun at Hyper-Kamiokande or at DUNE 40. We also find that signals for boosted DM from the GC and the Sun are complementary as the detectors would be able to probe different parts of the parameter space for the different sources.

In this part of the dissertation, we show the importance of working in the effective field theory framework. In this framework we can explore a potential signal without worrying about the underlying complete model and working free of many parameters and degrees of freedom. However, if a signal is detected it would be very hard to characterize it and a full theory would be needed to understand its properties.

Chapter 4

Boosted Dark Matter

The DM scenarios we investigated in chapters 2 and 3 are very attractive. Naturally the kind of phenomenology they present is very abundant with large amounts of parameter space available to study using complementary search strategies. We found that in each DM scenario there are positive prospects for detection, providing direction on where to focus our future searches. Undoubtedly, these are not the only DM scenarios to consider and there are many more which are highly experimentally motivated and harbor appealing prospects.

Among the myriad possibilities, scenarios with multiple dark matter particles are well motivated and their implications have been studied at different scales from the large in cosmology to the small at the Large Hadron Collider (LHC) at CERN [36]. Several issues have been especially investigated on the cosmological side in the context of multiple dark matter candidates. While N-body simulations of structure formation based on cold dark matter (CDM) present a steep cusp density profile [183], observations of dwarf galaxies indicate a cored density profile rather than a cusped one [184] (so-called "core vs cusp problem"). Simulations also predict that CDM evolves to very dense sub-halos of Milky Way type galaxies, which can not host the brightest satellites, but it would be hard to miss the observation of these substructures (known as the "too big to fail problem") [185]. Warm dark matter has been proposed as a solution to the small scale conflict between the observations and the simulations with CDM, since it is expected to develop shallower density profiles at a small scale and would avoid

unreasonably dense sub-halos [186].

Self-interacting DM (SIDM) has been suggested as another interesting solution to those small scale problems [187]. Cosmological simulations with SIDM [188] show that SIDM with the ratio of the DM self-interaction cross section to the DM mass $\sigma_{\chi\chi}/m_\chi \sim \mathcal{O}(0.1-1\,\mathrm{cm}^2/\mathrm{g})$ can reconcile the inconsistency between simulations and observations at a small scale, while it does not modify the CDM behavior at a large scale. Analysis of the matter distribution of the Bullet Cluster [189] provides the most robust constraint on SIDM, $\sigma_{\chi\chi}/m_\chi < 1.25\,\mathrm{cm}^2/\mathrm{g}$. Another analysis based on the kinematics of dwarf spheroidals [190] shows that SIDM resolves the small scale conflicts of CDM only when $\sigma_{\chi\chi}/m_\chi \gtrsim 0.1\,\mathrm{cm}^2/\mathrm{g}$.

In this chapter, we investigate the detection prospects of a two-component dark matter at large volume neutrino detectors. We focus on a scenario with a relatively large mass gap between the two components, where the heavier candidate interacts with the standard model (SM) particles only at loop level. Its sister (the light one) is assumed to have interactions with both the heavier counterpart and the standard model particles. If the heavier dark matter is dominant in our current universe, the dark sector with such candidates is secluded and all current direct and indirect bounds are evaded. Although the light dark matter particles are subdominant, they may be produced via the annihilation of the heavy sisters with a large boost due to the large mass difference. Boosted DM arises in various multi-component DM scenarios such as semi-annihilation $\psi_i\psi_j \to \psi_k\phi$ [42, 58, 191, 192], assisted freeze-out $\psi_i\psi_i \to \psi_j\psi_j$ [42], and decay $\psi_i \to \psi_j + \phi$. Recently a possibility of detecting a boosted dark matter particle in large volume neutrino telescopes has been examined [56, 57, 193–197]. In Ref. [194], the heavier DM annihilates in the center of the Galaxy, and its pair annihilation products travel to the Earth and leave Cherenkov light in the detector via a neutral current-like interaction, which points toward the galactic center (GC). Detection of boosted dark matter from the Sun has been studied in Refs. [195], where a search for proton tracks pointing toward the Sun is proposed in a different model.

Implication of self-interaction in the context of solar BDM has been discussed in Ref. [56, 57]. While more recently, the sensitivity of DUNE and SK, for BDM from the GC and dwarf spheroidal galaxies [198] was investigated. In this study, we explore the detection prospects of boosted dark matter,

from the center of the Milky Way Galaxy. We consider as well BDM from the Sun when the heavier component is captured in the presence of self-interactions. We study the discovery potential of Boosted DM at Super-K, Hyper-K, PINGU, we then compare the sensitivities of near future experiments such as the Liquid argon based Deep Underground Neutrino Experiment (DUNE) and SK as well as HK which are Cherenkov radiation based. This chapter is therefore outlined in the following manner. We consider the model studied in Ref. [194], which we revisit in section 4.1. We then explore the experimental capabilities of each detector as well as the estimation of background events in section 4.2. Furthermore, we discuss the detection of boosted DM from three sources; the GC (in section 4.3), the Sun (in section 4.4) and the Earth (in section 4.5). Finally we give our conclusions at the end of the dissertation.

4.1 Boosted Dark Matter and the Assisted Freeze-out Mechanism

In this section, we present an explicit example of a model with two-component DM in order to discuss the detection prospects of boosted DM. We choose the model studied in Ref. [194] based on the assisted freeze-out mechanism [42]. Additionally we introduce DM self-interaction preferred by cosmological simulations and observations for the heavier constituent of the two DM components for observations in the Sun. We only briefly summarize the key points of our bench mark model and refer to Ref. [194] for details on the model.

4.1.1 Theoretical Background

We consider the case where ψ_A and ψ_B are two stable DM candidate particles with masses $m_A > m_B$. This can be achieved with separate symmetries, for example, $\mathrm{U}(1)' \otimes \mathrm{U}(1)''$ [42] or $Z_2 \otimes Z_2'$ [194]. We assume that the two DM species, ψ_A and ψ_B interact via a contact operator,

$$\mathscr{L}_{AB} = \frac{1}{\Lambda^2}\overline{\psi}_A \psi_B \overline{\psi}_B \psi_A \,, \tag{4.1}$$

and that ψ_A can only annihilate into ψ_B and not directly into SM particles. Moreover, the heavier

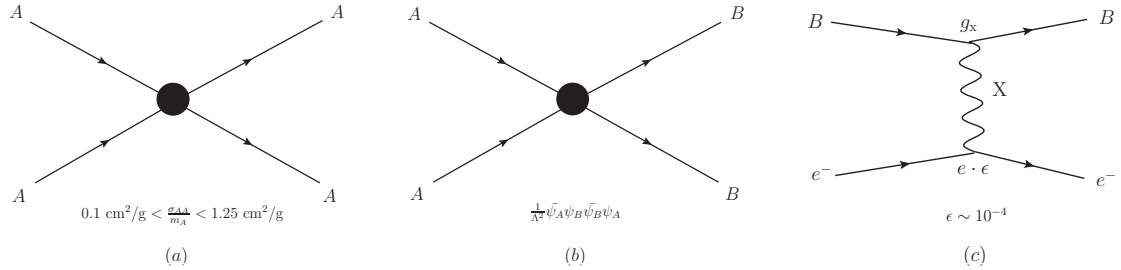

Fig. 4.1 Diagrams for (a) self-interaction of the heavier DM ψ_A, (b) production of the boosted DM ψ_B from the annihilation of ψ_A, and (c) elastic scattering of ψ_B off an electron.

component ψ_A is the dominant DM constituent in the universe. The boosted DM ψ_B is currently produced via the contact interaction Eq. (4.1). We additionally allow a self-interaction for ψ_A in the range of $0.1\,\mathrm{cm}^2/\mathrm{g} < \sigma_{AA}/m_A < 1.25\,\mathrm{cm}^2/\mathrm{g}$ (Figure 4.1(a)), favored by simulations and observations [187–190].

The particle ψ_B is charged under a hidden $\mathrm{U}(1)_X$ gauge symmetry, with a charge $Q_X^B = 1$ for simplicity, which is spontaneously broken leading to the gauge boson mass m_X. In addition, a mass hierarchy, $m_A > m_B > m_X$ is assumed. The gauge coupling of $\mathrm{U}(1)_X$, g_X will be taken to be large enough, e.g. $g_X = 0.5$, so that the thermal relic density of ψ_B is small due to the large annihilation cross section of the process $\psi_B\overline{\psi}_B \to XX$. We assume that the DM sector couples to the SM sector only through a kinetic mixing between $\mathrm{U}(1)_X$ and $\mathrm{U}(1)_{\mathrm{EM}}$ (originally $\mathrm{U}(1)_Y$) [199, 200],[1]

$$\mathscr{L} \supset -\frac{1}{2}\sin\varepsilon X_{\mu\nu}F^{\mu\nu}\,. \tag{4.2}$$

Thus, ψ_B can scatter off SM particles via a $t-$channel X boson exchange.

This model can be described by a set of seven parameters:

$$\{m_A, m_B, m_X, \Lambda, g_X, \varepsilon, \sigma_{AA}\}\,, \tag{4.3}$$

where Λ will be appropriately taken in our analysis to obtain the required DM relic density, $\Omega_A \simeq \Omega_{\mathrm{DM}} \approx$

[1] One can find a general and detailed analysis on a hidden sector DM and the kinetic mixing in Ref. [200].

0.2, as done in Ref. [194]. In all the interactions between DM and SM particles, g_X and ε always appear as a simple combination, $(g_X \cdot \varepsilon)$. As a result, our analysis will depend on five parameters, $\{m_A, m_B, m_X, g_X \cdot \varepsilon, \sigma_{AA}\}$. For an easier comparison, we choose the same benchmark scenario as in Ref. [194], except for ε,

$$m_A = 20\,\text{GeV},\ m_B = 0.2\,\text{GeV},\ m_X = 20\,\text{MeV},\ g_X = 0.5,\ \text{and}\ \varepsilon = 10^{-4}. \tag{4.4}$$

However, we choose $\varepsilon = 10^{-4}$, instead of 10^{-3} chosen as a reference value in Ref. [194], for boosted ψ_B to avoid too much energy loss during its traversal of the Sun as explained in Section 4.4.4. $\varepsilon = 10^{-4}$ happens to be consistent with current limits on a hidden X gauge boson (or a dark photon), $\varepsilon \lesssim \mathcal{O}(10^{-3})$ for $m_X \gtrsim 10$ MeV [201–206]. Furthermore, for consistency and ease of cross-checking, we use $\varepsilon^2 = 2 \times 10^{-7}$ and $m_X = 15$ MeV for our study of BDM from the GC. We further extend this to the Sun to evaluate the effect of this coupling on the BDM flux.

4.1.2 Relic Abundance and Scattering Cross Section

A set of coupled Boltzmann equations describes the evolution of the relic density of the two DM particles, ψ_A and ψ_B, in the assisted freeze-out mechanism [42, 194, 207]. [1] The annihilation process $\psi_A \overline{\psi}_A \to \psi_B \overline{\psi}_B$ (Figure 4.1(b)) determines the thermal relic abundance of ψ_A as well as the production rate of boosted ψ_B in the current universe. The annihilation cross section for the process is obtained as

$$\langle \sigma_{A\overline{A}\to B\overline{B}}\, v \rangle \simeq \frac{1}{8\pi\Lambda^4}\,(m_A + m_B)^2 \sqrt{1 - \frac{m_B^2}{m_A^2}} + \mathcal{O}(v^2) \tag{4.5}$$

from the contact operator in Eq. (4.1). In the limit $\langle \sigma_{B\overline{B}\to XX}\, v \rangle \gg \langle \sigma_{A\overline{A}\to B\overline{B}}\, v \rangle$, the relic abundance of ψ_A is given by [194]

$$\Omega_A \simeq 0.2 \left(\frac{5 \times 10^{-26}\,\text{cm}^3/\text{s}}{\langle \sigma_{A\overline{A}\to B\overline{B}}\, v \rangle} \right). \tag{4.6}$$

[1] See Ref. [42] for a numerical analysis and Ref. [194] for more details on the analytic estimates.

Indeed, $\langle\sigma_{B\overline{B}\to XX}v\rangle \gg \langle\sigma_{A\overline{A}\to B\overline{B}}v\rangle$ corresponds to the case that we are interested in, and thus the abundance of ψ_A dominates over that of ψ_B. In our numerical analysis, we will set $\langle\sigma_{A\overline{A}\to B\overline{B}}v\rangle \simeq 5\times10^{-26}\,\mathrm{cm}^3/\mathrm{s}$, matching the thermally averaged annihilation cross-section required for a thermal relic.

The lighter component ψ_B can scatter off SM particles via a $t-$channel X boson exchange through the kinetic mixing shown in Eq. (4.2). However, we cannot detect signals from scattering off nuclei by the thermal relic ψ_B in dark matter direct detection experiments due to its very small abundance, e.g., $\Omega_B \approx \mathcal{O}(10^{-7}-10^{-6})$ for the benchmark scenario in Eq. (4.4). As shown in Ref. [194], the boosted ψ_B from the process $\psi_A\overline{\psi}_A \to \psi_B\overline{\psi}_B$ might be detected at a large volume neutrino detector through the elastic scattering off electrons, $\psi_B e^- \to \psi_B e^-$ (Figure 4.1(c)). The minimum detectable scattered electron energy is set by the threshold energy of each experiment, $E_e^{\min} = E_e^{\mathrm{th}}$, and the maximum energy is given by

$$E_e^{\max} = m_e\,\frac{(E_B+m_e)^2+E_B^2-m_B^2}{(E_B+m_e)^2-E_B^2+m_B^2}\,, \tag{4.7}$$

where E_B is the energy of boosted ψ_B before collision with a target electron. The differential cross section for the process $\psi_B e^- \to \psi_B e^-$ is given by

$$\frac{d\sigma_{Be^-\to Be^-}}{dt} = \frac{1}{8\pi}\,\frac{(e\varepsilon g_X)^2}{(t-m_X^2)^2}\,\frac{8E_B^2m_e^2+t(t+2s)}{s^2+m_e^4+m_B^4-2sm_e^2-2sm_B^2-2m_e^2m_B^2}\,, \tag{4.8}$$

where $s = m_B^2+m_e^2+2E_Bm_e$ and $t = 2m_e(m_e-E_e)$.

The heavier DM ψ_A can interact with the SM sector via a ψ_B loop even since ψ_A has no direct coupling to the SM sector. The ψ_A-nucleon scattering cross section is expressed as

$$\sigma_{A-\mathrm{nucleon}} = \frac{\mu_{A-p}^2(Z\varepsilon e)^2}{\pi A^2}\,\frac{t^2}{(t-m_X^2)^2}\left[\frac{g_X}{48\pi^2}\,\frac{\log(m_B^2/(\lambda\Lambda)^2)}{\Lambda^2}\right]^2\,, \tag{4.9}$$

where μ_{A-p} is the ψ_A-nucleon reduced mass, A and Z denote the atomic mass and the proton number of a target nucleus, $t=-2m_NE_R$ with the nucleus mass m_N and the nuclear recoil energy E_R. The

quantity λ is a hidden sector Yukawa coupling of order unity, and Λ is determined by $\langle \sigma_{A\bar{A}\to B\bar{B}} v \rangle \simeq 5 \times 10^{-26}\,\mathrm{cm}^3/\mathrm{s}$ [194]. The cross section $\sigma_{A-\mathrm{nucleon}}$ is suppressed by the small ε parameter and one-loop factor, and thus the direct detection of the relic ψ_A is almost impossible even in a future DM direct detection experiment, e.g. XENON1T. However, even this small cross section will contribute to the accumulation of ψ_A in the Sun.

4.2 Experimental Details and Backgrounds

We discuss here the experimental specifications and provide conservative estimates for background events at DUNE, SK, HK and PINGU.

The DUNE far detector, which consists of four LArTPC modules to be located deep underground at the Sanford Underground Research Facility, South Dakota, provides an excellent opportunity for particle physics beyond the primary mission of the experiment. The excellent angular resolution and particle identification capability of the LArTPC detector will substantially reduce the background in the direction of the expected DM-induced neutrino signal, and can potentially provide competitive limits in the low DM-mass range. In this study, we consider the direct detection of BDM with the DUNE LArTPC rather than detecting neutrinos induced by DM annihilation. Later we will compare the sensitivities of DUNE against those for other neutrino detectors based on Cherenkov radiation, such as SK and HK. We compare as well with detectors based in ice, such as the future upgrade of IceCube called PINGU. We further mention here that we do not consider IceCube itself in this study due to its very large energy threshold and angular resolution [194]. Table 4.1 summarizes detector volume, threshold energy and angular resolution for SK, HK, DUNE and PINGU.

Furthermore, the dominant backgrounds for the boosted DM signal originate from the charged current interaction of atmospheric neutrinos, i.e., $\nu_e\, n \to\ e^-\, p$ in the mass range of our interests. On the other hand, solar neutrinos dominate the background below energies around 20 MeV [215]. Further background can come from muons which do not Cherenkov-radiate but decay to neutrinos in the SK/HK detector. The relevant energy range for the muon background is about 30–50 MeV and can be alleviated via fiducial volume cuts [216]. Table 4.1 shows 100 MeV for threshold energy at SK/HK.

	Volume (kTon)	$E_{\rm th}$ (MeV)	$\theta_{\rm res}$ (°)	Running Time (years)
SK [208]	22.5	100	3°	> 13.6
HK [209]	560	100	3°	
DUNE [210]	40-50	30	1°	
PINGU [211]	500	1000	23°	

Table 4.1 List of experiments (SK, HK, DUNE and PINGU) considered in this study with volume, threshold energy, angular resolution, and running time. In principle, the threshold energy at SK/HK could be lowered below 100 MeV at the cost of having worse energy and angular resolution. However, in our study we use 100 MeV to reduce backgrounds from solar neutrinos and muon decays [194]. We consider two different sizes for DUNE: 10 kTon (DUNE 10) and 40 kTon (DUNE 40), since the staged implementation of the far detector is planned as four 10 kTon modules [210, 212–214]. We also consider here the planned implementation of PINGU, which is a future low threshold energy upgrade of the IceCube detector.

However, in principle the threshold energy at SK can be lowered even below 10 MeV. For example, Ref. [217] studies solar neutrinos, focusing on the 5–20 MeV range. In this case, both energy resolution and angular resolution become poor, $\frac{\sigma(E)}{E} > 0.15$ and $\theta_{\rm res} > 25^\circ$ for $E_e < 10$ MeV [217]. We use $E_e > 100$ MeV in our analysis, to reject backgrounds from solar neutrino and muon decays. However, this cut may be lowered down to 50–100 MeV with slightly poorer angular resolution [194, 217]. For DUNE, the muon background can be distinguishable due to excellent particle ID and we use $E_{\rm th} = 30$ MeV as described in the DUNE CDR [210, 212–214].

For the angular resolution of SK/HK, we use $\theta_{\rm res} = 3^\circ$ following Ref. [194] but in the energy range of our interests $E_e > 100$ MeV, it can be brought down to a lower value. The angular resolution of SK (single-ring e-like events) is 3° for sub-GeV (< 1.33 GeV) and 1.2° for multi-GeV (> 1.33 GeV) [218].

Super-K has measured atmospheric neutrino events for 10.7 years [218]. Thus, to estimate the backgrounds for BDM at SK, we use the fully contained single-ring e-like events including both sub-GeV (0-decay electron events only), which are 7,755 in total and multi-GeV 2,105 single-ring electron events. These have been detected in the energy ranges of $(0.1\,\text{GeV} - 1.3\,\text{GeV})$ and $(1.33\,\text{GeV} - 100\,\text{GeV})$, respectively [219]. For Super-K and Hyper-K, we use all 9,860 events, in the range of $(0.1\,\text{GeV} - 100\,\text{GeV})$ as conservative backgrounds although higher energy background events are less

	DUNE 10	DUNE 40	SK	HK	PINGU
GC	1 with 10°	4 with 10°	7.01 with 10°	174 with 10°	562 with 23°
Sun	0.01 with 1°	0.04 with 1°	0.632 with 3°	15.7 with 3°	562 with 23°

Table 4.2 Expected number of background events per year with appropriate angular cut and threshold energy. For the GC, we consider only 10° for the angular resolution, since the GC is a diffuse region, while the Sun is a point-like object and for its case we use the angular resolutions of the experiments.

relevant to ψ_B from a lighter mass of ψ_A which produces a less energetic event. Thus, we have a yearly background event rate:

$$\frac{N_{\rm BG}}{\Delta T} = 922/\text{year}\left(\frac{V_{\rm exp}}{2.25\times10^4\,\text{m}^3}\right), \tag{4.10}$$

where $V_{\rm exp}$ is the volume of the specific detector. For PINGU, we use all the events including multi-ring and μ-like events in the $(1.33\,\text{GeV} - 100\,\text{GeV})$ energy range due to a higher $E_e^{\rm th}$ and a poor reconstruction efficiency of the Cherenkov rings [194]. After rescaling by the effective detector volume of PINGU, $5\times10^5\,\text{m}^3$, we obtain a background rate of 14,100/year.

For our discussion in the rest of this study, we normalize the rate to 13.6 years, which is the current exposure time at SK.[1]

In the case of BDM from the GC, the number of expected signal events is obtained within a cone of half angle $\theta_C \simeq 10^\circ$ for maximum sensitivity, and the backgrounds are calculated correspondingly, $\frac{N_{\rm SK}^{\theta_C}}{\Delta T} = \frac{1-\cos\theta_C}{2}\frac{N_{\rm SK}^{\text{all sky}}}{\Delta T} \simeq 7.01$ year^{-1} for 22.5 kTon [194]. LArTPC detectors have several advantages over Cherenkov-based detectors, such as lower threshold energy, better angular resolution and efficient vetoing of events with hadronic activities [198]. These features are useful in identifying BDM signals and reduce the number of background events. A background-study at DUNE 10 (DUNE with 10 kTon) by simulation using the GENIE neutrino Monte-Carlo software results in a conservative estimate of background events, $N_{\rm DUNE10}^{\text{all sky}}/\Delta T \simeq 128$ year^{-1} for 10 kTon [198],[2] and thus for the GC, $\frac{N_{\rm DUNE10}^{\theta_C}}{\Delta T} =$

[1] More data has been used in Ref. [220] but it does not discriminate 0- and 1-decay electron events.

[2] According to DUNE CDR [210], the expected number of fully contained electron-like events including oscillations is 14053/(350 kTon·year), which corresponds to 402 year^{-1} for DUNE 10. In Ref. [198], they however find that less than 32%

$\frac{1-\cos\theta_C}{2}\frac{N^{\text{all sky}}_{\text{DUNE10}}}{\Delta T} \simeq 1\ \text{year}^{-1}$. Background rates for DUNE 40 (DUNE with 40 kTon) and HK are obtained by a simple rescaling based on their volume. See Table 4.2 for a summary of background events used in our study.

In the case of BDM arising from the Sun, angular resolution becomes crucial. The number of background events within a cone of angle θ is proportional to $\frac{1-\cos\theta}{2} \approx \theta^2/4$ for $\theta \ll 1$, and decreases rapidly as θ decreases. On the other hand, the number of signal events does not change, as the Sun is effectively a point-like source. Therefore, θ_C can be reduced to θ_{res} as shown in Table 4.1, which will reduce the number of background events significantly, while the number of signal events is not affected. In comparison between SK and DUNE, the angular resolution for SK is $\theta^{\text{SK}}_{\text{res}} = 3^\circ$ while it is $\theta^{\text{DUNE}}_{\text{res}} = 1^\circ$ for DUNE. This implies that background rejection at DUNE would be nine times better than at SK, *if all other conditions are identical*. A change in angular cut from 10° for the GC to 1° for the Sun reduces background events by a factor of 100 for the same detector. Likewise, a similar analysis can be done in comparing DUNE with PINGU. In the case for PINGU however, the large angular resolution means that the background is not reduced much when considering the Sun compared with the GC.

Another strength of the DUNE detector is a lower threshold energy, $E_{\text{th}} = 30$ MeV. This is partly due to excellent particle ID with the LArTPC, which also allows better background rejection, *i.e.,* rejection of Michel electrons from muon decays [198].

The main advantage of SK over DUNE is that it has already been running for more than 13 years and will accumulate more data over the next few years at least. In addition, its volume is about twice as large as that at DUNE 10, while HK might be 10 times (or more) bigger than DUNE 40. Moreover, the volume of PINGU would be the same size as that of HK, however HK will have an advantage over PINGU, due to its much smaller angular resolution and energy threshold. The phenomenology of BDM with the HK detectors at two different location is also worth investigating [221]. In the following sections we focus on the rates of boosted DM from different sources, namely the Galactic center, the Sun and the earth.

of background events pass the hadronic cuts which are implemented after simulation. As a result, for DUNE 10, 402 $\text{year}^{-1} \times 32\% \simeq 128\ \text{year}^{-1}$ is obtained.

4.3 Boosted Dark Matter from the Galactic Center

In this section, we discuss the sensitivity of the detectors on the boosted dark matter arising from the galactic center. Here we report the number of events expected at PINGU as in Table 4.2.

4.3.1 Flux of Boosted DM and Signal

Following the formalism in Ref. [194], we calculate the flux of boosted DM ψ_B coming from the galactic center through the annihilation $\psi_A\overline{\psi}_A \to \psi_B\overline{\psi}_B$ as

$$\frac{d\Phi_{\rm GC}}{d\Omega dE_B} = \frac{r_{\rm Sun}}{16\pi}\left(\frac{\rho_0}{m_A}\right)^2 \langle\sigma_{A\bar{A}\to B\bar{B}}v\rangle J\frac{dN_B}{dE_B}, \tag{4.11}$$

where $r_{\rm Sun} = 8.33$ kpc is the distance from the GC to the Sun, ρ_0 is the local dark matter density with a value of 0.3 GeV/cm^3 and $\langle\sigma_{A\bar{A}\to B\bar{B}}v\rangle$ is the thermally averaged annihilation cross-section of ψ_A into ψ_B around the GC. The galactic halo information is encoded in the so-called J-factor which involves an integral over the DM density squared along the line of sight (l.o.s):

$$J(\theta) = \int_{\rm l.o.s}\frac{ds}{r_{\rm Sun}}\left(\frac{\rho(r(s,\theta))}{\rho_0}\right)^2. \tag{4.12}$$

Here $\rho(r(s,\theta))$ is the galactic halo DM density profile and s is the l.o.s distance from the source to the Earth, while $r(s,\theta) = \sqrt{r_{\rm Sun}^2 + s^2 - 2r_{\rm Sun}\cdot s\cdot\cos\theta}$ is a coordinate distance centered on the GC and θ is the angle between the direction of the l.o.s and the GC–Earth axis. We assume the NFW halo profile [222, 223] following Ref. [194]. For the purposes of this study, it is in fact more robust to consider a DM halo profile incorporating SIDM, which ensures the correct DM density at the GC and around our solar system. Recent studies on SIDM however suggest that for the self-interaction strengths provided by the limits from the Bullet cluster and dwarf spheroidals, density profiles of SIDM are intimately tied with the details of the disk and bulge formation as well as the associated feed back of a baryon dominated galaxy such as the Milky Way. SIDM profile turns out to be comparable to the NFW profile in our region of interest [224–226]. We assume that the ψ_B particles from this process are

mono-energetic and thus their differential energy spectrum is simply described by

$$\frac{dN_B}{dE_B} = 2\delta(E_B - m_A)\,, \tag{4.13}$$

where E_B is the energy of the boosted particle ψ_B. Finally, the boosted ψ_B flux over a cone of a half angle 10° around the GC can be approximated by [198]

$$\Phi_{\rm GC}^{10^\circ} \simeq 4.7\times10^{-8}{\rm cm}^{-2}{\rm s}^{-1} \times \left(\frac{\langle\sigma_{A\bar{A}\to B\bar{B}}v\rangle}{3\times10^{-26}{\rm cm}^3/{\rm s}}\right)\left(\frac{20\,{\rm GeV}}{m_A}\right)^2 . \tag{4.14}$$

To mitigate backgrounds, we require the BDM events to fall within a θ_C cone around the GC. The optimal choice of θ_C is about 10° for the annihilation case as discussed in Ref. [194], which is also used in our analysis. For BDM interacting with electrons, the number of signal events is given by

$$N_{\rm sig}^{\rm GC} = \Delta T\; N_{\rm target}\; \Phi_{\rm GC}^{\theta_C}\; \sigma_{Be^-\to Be^-}\,, \tag{4.15}$$

where ΔT is the exposure time of the experiment and $N_{\rm target}$ is the total number of target electrons in a given experiment, which is proportional to the volume of the experiment. The quantity $\Phi_{\rm GC}^{\theta_C}$ is the flux of BDM particles coming from a θ_C cone around the GC and $\sigma_{Be^-\to Be^-}$ is the elastic scattering cross-section between the boosted ψ_B and an electron in the experiment. We refer to Ref. [194] for more details.

To compute the sensitivity of each detector for BDM coming from the GC, we use the number of background events listed in Table 4.2. The signal significance is defined as

$$\sigma = \sqrt{2\big(N_{\rm sig}+N_{\rm BG}\big)\log\Big(1+\frac{N_{\rm sig}}{N_{\rm BG}}\Big) - 2N_{\rm sig}}\,, \tag{4.16}$$

where $N_{\rm sig}$ is the number of signal events given by Eq. (4.15) and $N_{\rm BG}$ is the number of background events in a θ_C cone, given in section 4.2. We have verified that the same results are obtained with a likelihood ratio, assuming a Poisson distribution as in Ref. [227].

In order to effectively study the dependence of the signal sensitivity on the threshold energy of

the experiment, we reduce the cross-section $\sigma_{Be^-\to Be^-}$ to a constant cross-section having assumed a constant scattering amplitude as discussed in Ref. [198]. In this limit, we redefine Eq. (4.15) as

$$N_{\rm sig}^{\rm GC} = \Delta T\, N_{\rm target}\, \Phi_{\rm GC}^{\theta_C}\, \sigma_0 \left(1 - \frac{E_{\rm th}}{E_{\rm max}}\right), \tag{4.17}$$

where σ_0 is the constant cross-section for $\sigma_{Be^-\to Be^-}$. The number of signal events has been rescaled in terms of the threshold energy of the experiment and the maximum energy imparted to an electron after scattering which is given by Eq. 4.7 To get the sensitivity in this limit, we use Eq. (4.16) with the same background rates.

4.3.2 Detection Prospects

We first reproduced all the results on BDM from the GC in Ref. [198], where the performance of SK, HK and DUNE detectors are compared, assuming the same 13.6 years of physics running for all detectors. The authors of Ref. [198] have shown the excellent performance of DUNE with 10 kTon, which is comparable to SK (with twice larger volume). Moreover, DUNE covers slightly larger parameter space due to the lower threshold energy. In Fig. 4.2 we show in the m_B vs m_A parameter space, the number of signal events expected per year at SK, HK, DUNE and PINGU. For illustration we show the parameter space covered if we would observe 10 events per year and 100 events per year. In Fig. 4.3, we show the 2σ signal-significance in the σ/m_A^2–$E_{\rm max}$ plane (top) and in the m_A–m_B plane (bottom) for the corresponding detectors. We consider two different timelines: 5 years of construction and 10 years of physics running of DUNE in the left panel, and 10 years of construction and 3 years of physics running of DUNE in the right panel. The total physics running time of SK would be 28.6 and 26.6 years, respectively. An approximate expression for the flux as in Eq. (4.14) is used only for the two figures in the upper panel of Fig. 4.3 (following Ref. [198]), while the full flux in Eq. (4.11) is used in all other figures. We used the corresponding volume, angular resolution and threshold energy for each detector as summarized in Table 4.1. We checked however that there is no significant difference between the results from 3° and 5° of angular resolutions for the GC analysis. We find that the increment

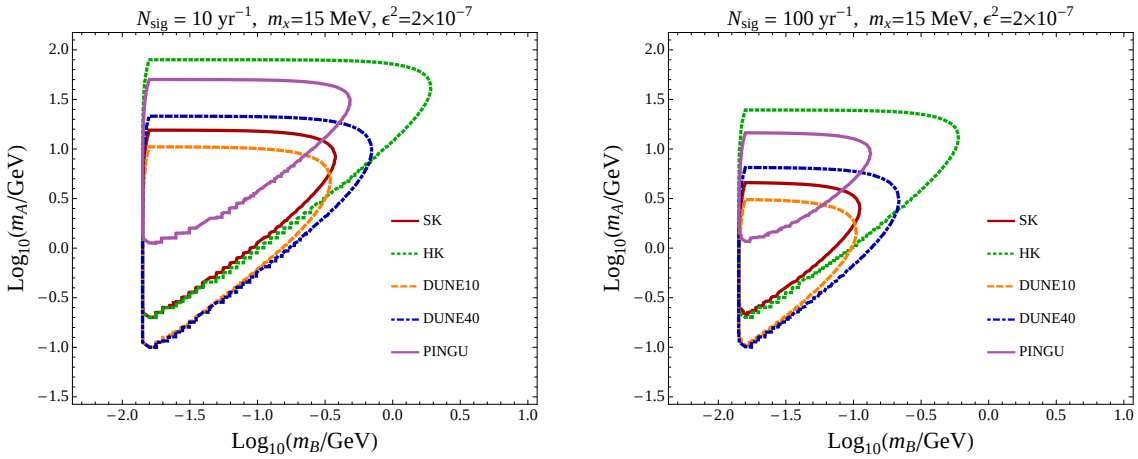

Fig. 4.2 Number of signal events per year for the different experiments for $\varepsilon^2 = 2 \times 10^{-7}$ and $m_X =$ 15 MeV. In the left panel we show contours for 10 events per year and on the right 100 events per year in the m_B vs m_A parameter space. These figures show that within the parameter space region covered by the experiments, we expect to see either 10 or 100 boosted DM events coming from the direction of the GC.

in the number of events with $E_{\rm th}$ =30 MeV to the number of events with $E_{\rm th}$ =100 MeV is about 20–50 % in the bulk of parameter space of the m_A–m_B plane, and the signal increases very rapidly closer to the diagonal direction, $m_A \sim m_B$.

Fig. 4.3 also includes the 2σ exclusion (in gray) using currently available all-sky SK data assuming a 10% systematic uncertainty in the background estimation. There are other relevant but model-dependent bounds such as the direct detection of non-relativistic ψ_B and CMB constraints [194]. Although the relic abundance of ψ_B is small, it has a large ψ_B-nucleon scattering cross section. The mass range of ψ_B that we are interested in is $m_B \lesssim \mathcal{O}(1)$ GeV, and the corresponding recoil energy is close to the threshold energy of many direct detection experiments. The most stringent bounds come from DAMIC [228] due to its low threshold energy. The expected elastic scattering cross section is so large that any events above the threshold energy would be seen, even when taking into account an effective nuclear cross section that is properly scaled down by the non-relativistic relic abundance, $\sigma^{eff}_{Bp\to Bp} = \frac{\Omega_B}{\Omega_{DM}}\sigma_{Bp\to Bp}$ [194]. From Ref. [228], we conclude that $m_B \geq 1$ GeV is disfavored by DAMIC data if ψ_B couples to quarks, which is shown as the cyan shaded region. Although sub-GeV DM is better constrained by scattering off electrons than off nuclei [229], as in XENON10 bounds [230], BDM sig-

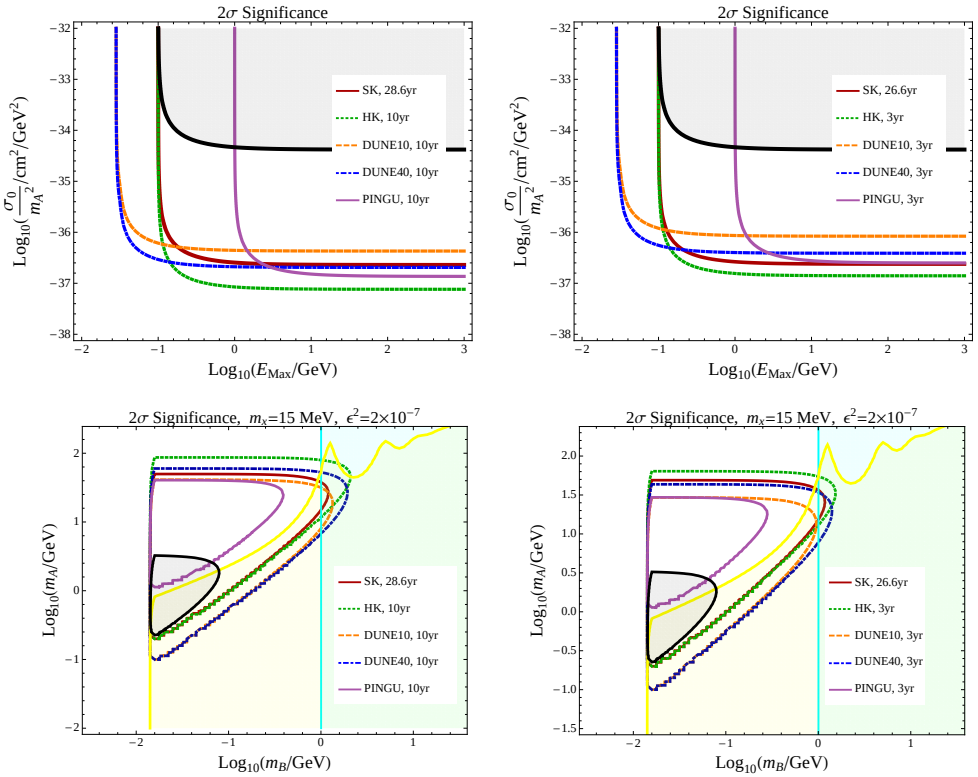

Fig. 4.3 95% limits on the effective cross section σ_0 (top panel) and the 2σ signal-significance (bottom panel) assuming 5 years of construction and 10 years of physics running of DUNE (left), and 10 years of construction and 3 years of physics running of DUNE (right). The corresponding total running time of SK would be 28.6 and 26.6 years, respectively. For comparison, we assume that the HK as well as PINGU timeline are the same as for DUNE. The gray-shade represents the current 2σ exclusion with all-sky data from SK, assuming 10% systematic uncertainty in the background estimation. The other shaded areas are potential bounds from direct detection of non-relativistic ψ_B (in cyan, with vertical boundary) and CMB constraints on ψ_B annihilation (in yellow, with diagonal boundary).

nals are not affected by XENON10 due to different kinematics, and it turns out that bounds from CMB heating are more important [194], which is shown as the yellow-shaded area. Other constraints such as limits on the dark photon, direct detection of non-relativistic ψ_A, indirect detection of non-relativistic ψ_B and BBN bounds on ψ_B annihilation are either weaker than the CMB bound or evaded by our choice of parameters. We note that apart from the current SK bound, all other limits are model-dependent and it is certainly possible to avoid or weaken the bounds. For instance, DM models with $p-$wave annihilation can easily avoid the CMB constraint due to v^2 suppression with $v \sim 10^{-3}$, and direct detection

bounds do not apply if the non-relativistic ψ_B does not couple to quarks.

4.4 Boosted Dark Matter Flux from the Sun

In this section, we briefly review the evolution of DM (ψ_A) number in the Sun, and calculate the boosted DM (ψ_B) flux from the annihilation of the heavier DM component (ψ_A). The DM capture in the Sun via the collisions between DM and nuclei was examined in Refs. [231, 232]. Subsequent studies discussed several important effects such as evaporation for a relatively light DM ($m_{\rm DM} \lesssim$ 3-5 GeV) [233, 234] and enhancement of the DM accumulation due to self-interaction [235, 236]. Such a DM self-interaction has been proposed to alleviate the small scale structure problems of simulations with collisionless CDM [187]. It has also been shown that self-interaction can participate in the evaporation process reducing the DM number [237].

4.4.1 Evolution of Dark Matter in the Sun

The time evolution of the DM number N_χ in the Sun is described by the following differential equation [237]

$$\frac{dN_\chi}{dt} = C_c + (C_s - C_e)N_\chi - (C_a + C_{se})N_\chi^2 , \tag{4.18}$$

where C_c is the DM capture rate by the Sun, C_s is the DM self-capture rate, C_e is the DM evaporation rate due to DM-nuclei interactions, C_a is the DM annihilation rate, and C_{se} is the evaporation rate due to the self-interaction. In our analysis, we assume that the DM and nuclei inside the Sun follow a thermal distribution and use numerical data on the solar model such as mass density $\rho(r)$, temperature $T(r)$, and mass fraction of the atom i, $X_i(r)$ inside the Sun given in Ref. [238].

If a DM particle interacts with nuclei, it loses its kinetic energy as it travels inside the Sun. The DM particle is gravitationally captured when its final velocity after its collision with nuclei is smaller than the escape velocity $v_{\rm esc}(r)$ from the Sun. The number of DM particles in the Sun increases through this capture process. The DM capture rate in the Sun C_c has been investigated in Refs. [234, 239, 240]. In

our study, we use the numerical results from Ref. [234] ($m_\chi \lesssim 10$ GeV) and Ref. [240] ($m_\chi \gtrsim 10$ GeV). For more details on the exact calculation, see Refs. [234, 239].

The coefficient C_a describes the annihilation of two DM particles trapped inside the Sun, which has been well studied in Refs. [231, 232]. Based on the exact numerical calculation, Refs. [234, 239] provided fitting functions: the former is valid in the range 0.1 GeV $\lesssim m_\chi \lesssim$ 10 GeV and the latter for $m_\chi \gtrsim$ a few GeV. We adopt the fitting functions from Ref. [234] ($m_\chi \lesssim 10$ GeV) and Refs. [239] ($m_\chi \gtrsim$ 10 GeV).

A captured DM particle could scatter off energetic nuclei and escape from the Sun when its velocity after the scattering is larger than the local escape velocity $v_{\rm esc}(r)$, which is generally called the evaporation process [232, 233]. The basic idea of evaporation is the same as capture. The main difference is whether the final velocity is smaller (for capture) or larger (for evaporation) than the escape velocity $v_{\rm esc}(r)$. The evaporation rate C_e is effective only for a low DM mass, $m_\chi \lesssim 5$ GeV and completely negligible for heavier DM masses. For the evaporation rate, the fitting functions to the numerical results given in Ref. [234] are used in our analysis. For more details on the calculation of C_e, see Refs. [233, 234].

Self-interactions of DM will also affect its capture and evaporation processes inside the Sun. The C_s is the self-capture rate by scattering off other DM particles that have already been trapped within the Sun. In this DM-DM scattering, a target DM particle that obtains too much kinetic energy will be ejected from the Sun, which results in no net accumulation of DM particles unlike the capture by collision with nuclei. However, the escape velocity from the interior of the Sun is at least two times larger than the typical velocity of a galactic DM particle. Thus, the ejection of a target DM particle via the DM-DM collision results in a tiny correction to the typical DM self-capture rate in the Sun [235]

$$C_s = \sqrt{\frac{3}{2}}\, n_\chi \sigma_{\chi\chi} v_{\rm esc}(R_\odot)\, \frac{v_{\rm esc}(R_\odot)}{\bar{v}}\, \langle \widehat{\phi}_\chi \rangle\, \frac{{\rm erf}(\eta)}{\eta}\,, \tag{4.19}$$

where n_χ is the local number density of galactic DM, $\sigma_{\chi\chi}$ is the self-elastic scattering cross section of DM, $v_{\rm esc}(R_\odot)$ is the escape velocity at the surface of the Sun, $\langle \widehat{\phi}_\chi \rangle$ is a dimensionless average solar potential experienced by the captured DM within the Sun, and $\eta^2 = 3(v_\odot/\bar{v})^2/2$ is a dimensionless

variable with the velocity of the Sun $v_\odot = 220\,\mathrm{km/s}$ and the local velocity dispersion of DM $\bar{v} = 270\,\mathrm{km/s}$. $\langle\widehat{\phi}_\chi\rangle \simeq 5.1$ [241] is generally used in the calculation of C_s, which however deviates from the commonly used value for smaller DM masses, $m_\chi \lesssim 10$ GeV. Thus, we numerically calculate $\langle\widehat{\phi}_\chi\rangle$ for our analysis. The full expression of the self-capture rate including the small ejection effect of the target DM particle is given in the Appendix of Ref. [235].

The last coefficient is the self-interaction induced evaporation rate C_{se}. A DM particle captured in the Sun can scatter off another captured DM particle through their self-interaction, which leads to the evaporation when one of two colliding DM particles has velocity greater than the escape velocity $v_{\rm esc}(r)$ after the collision. The authors of Ref. [237] recently investigated the self-interaction induced evaporation and provided details of the derivation of C_{se} in the Appendix. We numerically calculate C_{se} based on the analytic expression given in the Appendix of Ref. [237]. We assume that the DM temperature is in thermal equilibrium with the solar temperature following Ref. [237]. Thus, we use the solar temperature T as the DM temperature T_χ in our calculation.

4.4.2 Accumulated Dark Matter Number and Annihilation Rate

With the initial condition $N_\chi(0) = 0$, the solution to the DM evolution equation, Eq. (4.18) is given by [237]

$$N_\chi(t) = \frac{C_c \tanh(t/\tau_{\rm eq})}{\tau_{\rm eq}^{-1} - (C_s - C_e)\tanh(t/\tau_{\rm eq})/2} \tag{4.20}$$

with

$$\tau_{\rm eq} = \frac{1}{\sqrt{C_c(C_a + C_{se}) + (C_s - C_e)^2/4}}, \tag{4.21}$$

where the $\tau_{\rm eq}$ is the time-scale required for the DM number $N_\chi(t)$ in the Sun to reach the equilibrium between accumulation by C_c and C_s and dissipation by C_a, C_e, and C_{se}. Then, the DM annihilation rate

inside the Sun is simply given by

$$\Gamma_A^\chi = \frac{C_a}{2} N_\chi^2 . \tag{4.22}$$

For the age of the Sun $t = t_\odot \simeq 4.6 \times 10^9$ year, we obtain the currently accumulated number and annihilation rate of DM in the Sun. When the equilibrium state is attained, i.e., $t \gtrsim \tau_{\rm eq}$, N_χ and Γ_A^χ can be simplified as

$$N_\chi^{\rm eq} = \sqrt{\frac{C_c}{C_a + C_{se}}} \left(\sqrt{\frac{R}{4} + 1} \pm \sqrt{\frac{R}{4}} \right) \tag{4.23}$$

and

$$\Gamma_A^\chi = \frac{1}{2} \frac{C_c C_a}{C_a + C_{se}} \left(\sqrt{\frac{R}{4} + 1} \pm \sqrt{\frac{R}{4}} \right)^2 , \tag{4.24}$$

where $R \equiv (C_s - C_e)^2 / [C_c (C_a + C_{se})]$ is a dimensionless parameter defined by 5 coefficients in the DM evolution in Eq. (4.18), and the positive and negative signs are taken for $C_s > C_e$ and $C_s < C_e$, respectively [237]. Using our numerical code, we can obtain the results consistent with those in Ref. [237].

In Figure 4.4, we present the number of heavy DM ψ_A captured inside the Sun, $N_A^{\rm eq}$, for the benchmark model parameters as in Eq. (4.4). Min and Max curves respectively correspond to minimum and maximum values of the self-interaction of ψ_A in the preferred range, $0.1\,{\rm cm}^2/{\rm g} < \sigma_{AA}/m_A < 1.25\,{\rm cm}^2/{\rm g}$ [187–190]. In the case of no self-interaction, the amount of accumulated ψ_A is quite small since the ψ_A-nucleon scattering cross section is suppressed as explained in Section 4.1.2. However, the self-interaction of ψ_A, σ_{AA} can significantly enhance $N_A^{\rm eq}$.

4.4.3 Flux of Boosted Dark Matter

The flux of boosted DM ψ_B from the Sun through the annihilation $\psi_A \overline{\psi}_A \to \psi_B \overline{\psi}_B$ can be expressed as

$$\frac{d\Phi_B^{\rm Sun}}{dE_B} = \frac{\Gamma_A^{\psi_A}}{4\pi R_{\rm Sun}^2} \frac{dN_B}{dE_B} , \tag{4.25}$$

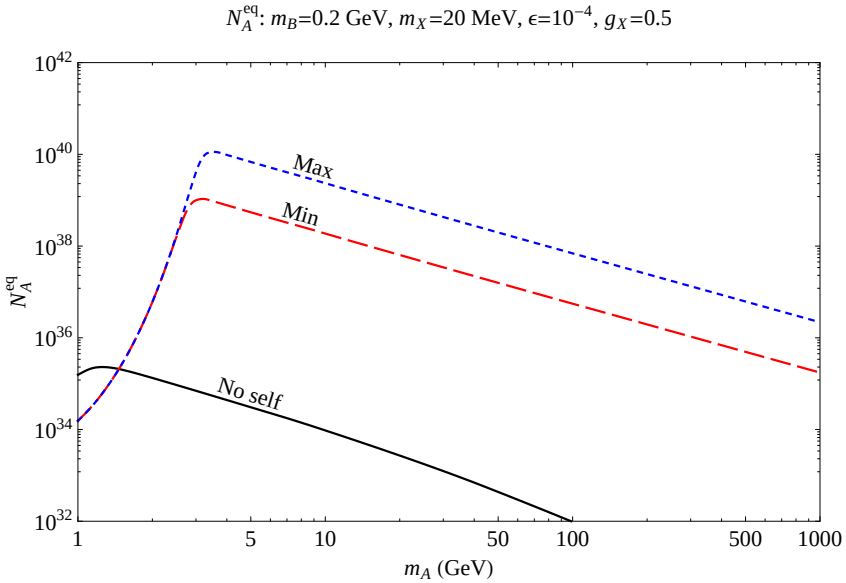

Fig. 4.4 Number of ψ_A captured inside the Sun as a function of the ψ_A mass m_A for the benchmark parameters in Eq. (4.4). Each curve corresponds to No ($\sigma_{AA}/m_A = 0$), Min ($\sigma_{AA}^{\rm min}/m_A = 0.1\,{\rm cm}^2/{\rm g}$), and Max ($\sigma_{AA}^{\rm max}/m_A = 1.25\,{\rm cm}^2/{\rm g}$) self-interaction, respectively. This shows the importance of the DM self-interaction in the capture and accumulation of ψ_A inside the Sun.

where $R_{\rm Sun}$ is the distance between the Sun and the Earth, $\Gamma_A^{\psi_A}$ is the annihilation rate of heavy DM ψ_A in the Sun, and dN_B/dE_B is the differential energy spectrum of boosted DM ψ_B at the source. The differential spectrum is simply given by

$$\frac{dN_B}{dE_B} = 2\delta(E_B - m_A)\,, \tag{4.26}$$

since the annihilation of heavy DM ψ_A, $\psi_A\overline{\psi}_A \to \psi_B\overline{\psi}_B$ produces two mono-energetic boosted ψ_B's. The annihilation rate of ψ_A in the Sun, $\Gamma_A^{\psi_A}$, is obtained from Eq. (4.22) (or Eq. (4.24)) with Eqs. (4.20) and (4.21) for $t = t_\odot$. Note that there is no need to consider the line-of-sight integration in Eq. (4.25), since the annihilation $\psi_A\overline{\psi}_A \to \psi_B\overline{\psi}_B$ in the Sun provides a point-like source of the boosted DM ψ_B. This is different from the case with the boosted DM flux from the GC as in Ref. [194], where one needs to compute a halo-dependent integral over the line-of-sight.

4.4.4 Energy Loss in the Sun

The boosted DM particles ψ_B produced from the annihilation $\psi_A\overline{\psi}_A \to \psi_B\overline{\psi}_B$ in the Sun may lose their kinetic energy as they pass through the Sun from their production points due to the relatively large scattering cross section with electrons, $\sigma_{Be^-\to Be^-}$ and the large radius of the Sun, $R_\odot \simeq 6.96\times10^{10}\,\text{cm}$. The energy loss of the particles during propagation through matter is well discussed in Ref. [242]. The boosted DM particle propagating through matter loses its energy dominantly through ionization of atoms, which is very similar to the energy loss of a heavy charged SM particle [194]. For $\beta\gamma = p/Mc$ around the range of $\mathcal{O}(10-100)$, the mean rate of energy loss of a muon is ~ 1 GeV/m inside the Earth and ~ 0.6 GeV/m inside the Sun. The boosted DM ψ_B scatters off SM particles via a $t-$channel X boson exchange while the muon does via a $t-$channel photon exchange. Analogous to Ref. [194], we can easily approximate the required travel length for the ψ_B to lose 1 GeV of energy by comparing the couplings and propagator of the $\psi_B - e$ scattering and those of the $\mu - e$ scattering:

$$L^{\text{Sun}}_{\psi_B} \approx L^{\text{Sun}}_{\mu}\left[\frac{\varepsilon^2 g_X^2}{e^2}\left(\frac{t}{t-m_X^2}\right)^2\right]^{-1}, \tag{4.27}$$

where $t = 2m_e(m_e - E_e)$ and $L^{\text{Sun}}_{\mu} \simeq (100/0.6)$ cm.

For the benchmark scenario in Eq. (4.4), we estimate $L^{\text{Sun}}_{\psi_B} \approx 3\times10^{10}\,(0.5/g_X)^2(10^{-4}/\varepsilon)^2$ cm which is about a factor of 2 smaller than $R_\odot \simeq 6.96\times10^{10}\,\text{cm}$. To escape from the Sun, the boosted DM ψ_B of the benchmark scenario will lose ~ 2 GeV of energy on average which corresponds to $\sim 10\%$ of the initial energy of ψ_B, $E^i_B \simeq m_A = 20$ GeV. For the above estimation, we use $E_e = E_e^{\text{peak}}$, the electron energy corresponding to the peak of the recoil electron spectrum which is a reasonable choice since the $\psi_B - e$ scattering mostly occurs around the peak energy in the electron recoil spectrum. For comparison, we obtain $L^{\text{Sun}}_{\psi_B} \approx 7\times10^{9}\,(0.5/g_X)^2(10^{-4}/\varepsilon)^2$ cm for the most extreme (conservative) case $E_e = E_e^{\text{max}}$. In the following section, we will numerically compute the required energy of ψ_B, ΔE^{Sun}_B, to escape from the production point to the surface of the Sun assuming that the travel distance of ψ_B inside the Sun is equal to the radius of the Sun, $R_\odot$. The ratio between the energy loss and the initial energy of ψ_B, $\Delta E^{\text{Sun}}_B/E^i_B$ can be larger than 0.1, even $\mathcal{O}(1)$, for a low ψ_A mass ($m_A \lesssim 10$ GeV), i.e. small E_e.

Consequently, in our analysis, we use $E_B^f = E_B^i - \Delta E_B^{\rm Sun} = m_A - \Delta E_B^{\rm Sun}$ as the energy of ψ_B in a detector and the parameter region for $E_B^i < \Delta E_B^{\rm Sun}$ is not scanned.

4.4.5 Detection Prospects

In this section, we discuss the detection prospects of boosted DM particles in neutrino detection experiments. We particularly concentrate on the flux of boosted DM ψ_B from a point-like source, the Sun and it detection at DUNE, SK, HK, and PINGU.

The angular resolution of each experiment is very crucial in this analysis. Thus, DUNE, SK and HK are very well fitted experiments to detect the boosted DM flux from the Sun due to their good angular resolution and low energy threshold as shown in Table 4.1. Though PINGU has a higher energy threshold $E_e^{\rm th} \simeq 1$ GeV and worse angular resolution $\theta_{\rm res} \simeq 23^\circ$, it will be able to have some sensitivity as shown in the following subsections. We will not discuss IceCube in spite of its very large volume ($\sim 10^3$ Mton) due to its high energy threshold, $E_e^{\rm th} > 100$ GeV (here most of the boosted DM signal would be lost). A Brief discussion on the detection prospects from the Earth is found in Section 4.5.

As discussed earlier, the signal of boosted DM ψ_B can be detected mainly through its elastic scattering off electrons, $\psi_B e^- \to \psi_B e^-$. Unlike the thermal relic ψ_A around the GC, the ψ_A trapped in the Sun becomes a point-like source of boosted DM ψ_B, and we need no angular-cut, θ_C. Finally, the number of electron signal events is given by

$$\begin{aligned} N_{\rm sig} &= \Delta T\, N_{\rm target}\, \Phi_B^{\rm Sun}\, \sigma_{Be^-\to Be^-} \\ &= \Delta T\, \frac{10\,\rho_{\rm target}\, V_{\rm exp}}{m_{\rm H_2O}}\, \frac{2\Gamma_A^{\psi_A}}{4\pi R_{\rm Sun}^2} \int_{E_e^{\rm min}}^{E_e^{\rm max}} dE_e\, \frac{d\sigma_{Be^-\to Be^-}}{dE_e}\,, \end{aligned} \tag{4.28}$$

where ΔT is the exposure time of the measurement, $N_{\rm target}$ is the total number of target electrons, $\Phi_B^{\rm Sun}$ is the boosted DM flux from the Sun and is dependent on the size of the self-interaction of relic ψ_A in the Sun. The larger the self-interaction strength, the more ψ_A particles are captured in the Sun, which results in a larger flux of boosted particles. The quantity $\sigma_{Be^-\to Be^-}$ is the $\psi_B - e$ scattering cross section, and the factor of 10 in the second line is the number of electrons per water molecule (for DUNE, this would

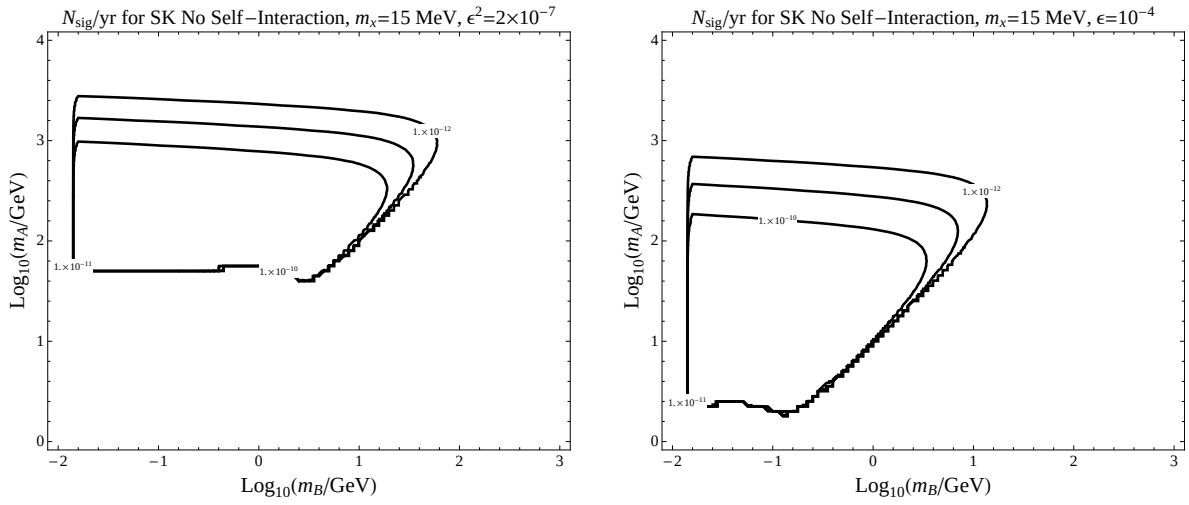

Fig. 4.5 The number of signal events per year for BDM from the Sun with no self-interactions. As an example we illustrate the number of BDM events detectable at SK with $\varepsilon^2 = 2\times10^{-7}$ ($\varepsilon^2 = 10^{-8}$) in the left (right) panel with $m_X = 15$ MeV, in the m_A vs m_B parameter space.

be replaced by the number of electrons in an Argon atom). We use a minimum energy-cut $E_e^{\rm min} = E_e^{\rm th}$ as in table 4.1 and $E_e^{\rm max}$ given by Eq. 4.7. For consistency, we have reproduced all the results shown in Ref. [56]. Figure 4.5 shows the number of events in the case of no self-interaction, showing that there is less accumulation of the ψ_A species in the sun resulting in a smaller flux of boosted DM particles and thus a very small number of events.

Using Eq. (4.28), we calculate the expected number of signal events per year. In Figure 4.6, we show the parameter space covered for the detection of 1 signal event per year in the (m_B, m_A) plane for the four experiments: Super-K, Hyper-K, DUNE and PINGU, respectively. With $\varepsilon^2 = 2\times10^{-7}$ ($\varepsilon^2 = 10^{-8}$) in the top (bottom) panel and for Min (Max) SI of ψ_A in the left-panel (right-panel). Naturally we can detect more signal events in an experiment with a larger volume and a lower $E_e^{\rm th}$, and also for stronger interactions of DM particles. Thus such an experiment is expected to cover a larger parameter space, when all are compared on an equal footing. Here Min (Max) SI is $\sigma_{AA}/m_A = 0.1\ (1.25)\,{\rm cm}^2/{\rm g}$. The interesting shape of the constant number of signal events is well studied in Ref. [56]. The boundary in the left side is set by $m_B > m_X$ where $m_X = 15$ MeV. The top edge is affected by the DM number density $\propto 1/m_{\rm DM}$. The right-diagonal edge is determined by $E_{\rm max} > E_{\rm min} = E_{\rm th}$. The bottom edge is set by the

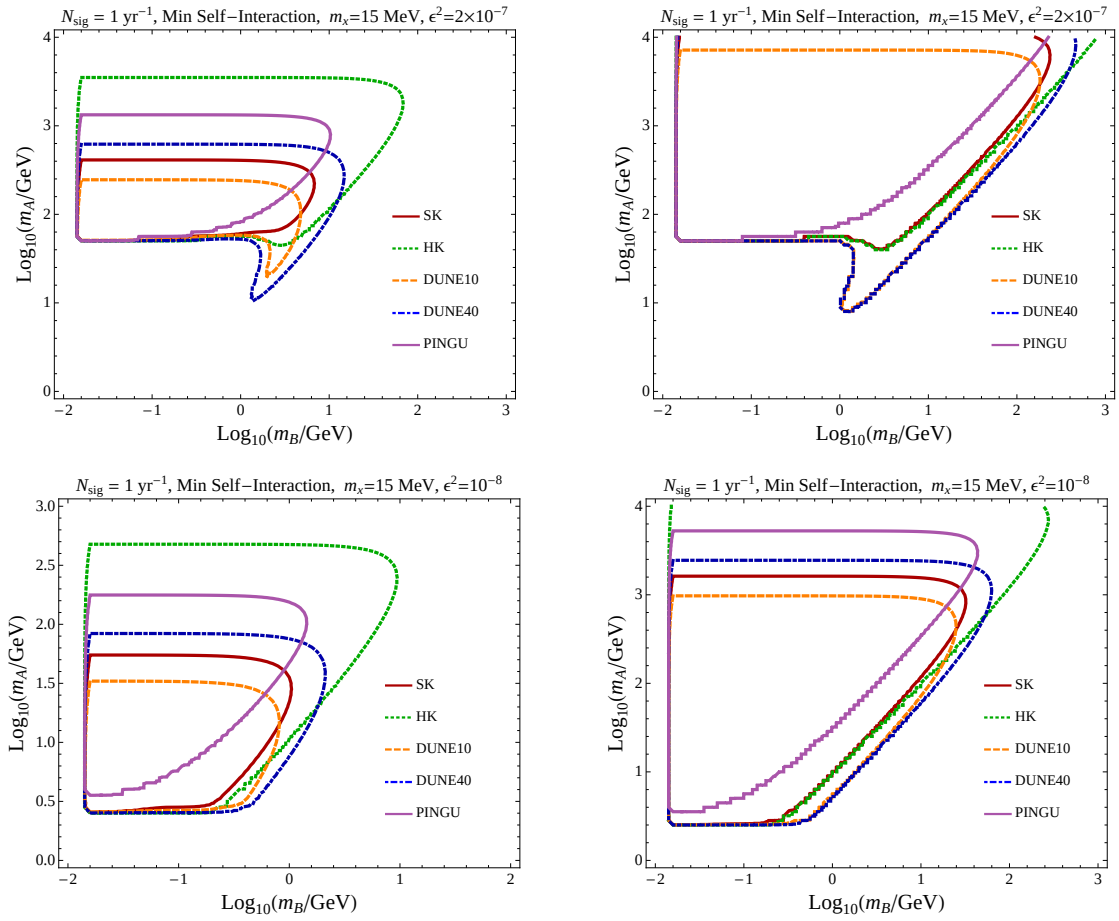

Fig. 4.6 The number of signal events per year expected at the discussed detectors for $\varepsilon^2 = 2\times10^{-7}$ ($\varepsilon^2 = 10^{-8}$) in the top (bottom) panel for Min (Max) SI in the left-panel (right-panel). Here we show contours illustrating the parameter space covered for the detection of one event per year at the experiments.

rapid drop in the accumulated number of DM particles inside the Sun for $m_{\rm DM} \lesssim$ 2–3 GeV due to the active evaporation ($\log_{10}(2.5\ {\rm GeV}/{\rm GeV}) \approx 0.4$). The bottom edge is also affected by the energy loss of BDM while traversing the Sun, which is especially active for a larger ε. This is shown in the upper panel of Fig. 4.6, for a smaller value, the effect is weak as illustrated in the bottom panel. Furthermore, the results for the case when there is maximum energy loss of boosted ψ_B in the Sun, $\Delta E_B^{\rm Sun}$ can be found in Ref. [56].

Using Eq. (4.16) and including the background rates given in Table 4.2, we calculate the 2σ signal-significance, which is shown in Fig. 4.7 for SK, HK, DUNE and PINGU for $\varepsilon^2 = 2\times10^{-7}$ ($\varepsilon^2 = 10^{-8}$)

in the top (bottom) panel for Min (Max) SI in the left-panel (right-panel). We assume that all detectors have been running for 13.6 years. As shown in Fig. 4.3, we include bounds from the CMB as well as DAMIC. It turns out that current SK limit applies to maximum self-interaction only.

As shown in the figure, the performance of DUNE 10 is much better than that of SK and DUNE 10 probes more parameter space: in the upper boundary because of the smaller background due to better angular resolution and along the diagonal direction due to the lower threshold energy. This implies that the strength of the DUNE detector is more pronounced for Solar BDM than for GC BDM. This effect is even more pronounced when comparing with PINGU. The low sensitivity of PINGU is due to its large angular resolution as well as larger energy threshold, resulting in lower background reduction and thus lower sensitivity. Similarly, DUNE 40 is comparable to HK and in fact probes more parameter space along the diagonal direction due to the lower threshold energy. Again this result illustrates the great performance of the DUNE detector with Solar BDM, even if the volumes of the HK and PINGU detectors are about 14 times larger than that of DUNE 40.

For BDM from the GC, the parameter space probed by these detectors is below $m_A \sim 100$ GeV for $\varepsilon^2 = 2 \times 10^{-7}$ [198], while the parameter space even above $m_A \sim 100$ GeV would be covered for BDM arising from the Sun. See the bottom panels of Fig. 4.3 and the top panels of Fig. 4.7.

Fig. 4.8 is the same as Fig. 4.7 but for a more realistic timeline. The 2σ significance is shown assuming 5 years of construction and 10 years of physics running of DUNE/HK (left), 10 years of construction and 3 years of physics running of DUNE/HK/PINGU (right) for $\varepsilon^2 = 2 \times 10^{-7}$ ($\varepsilon^2 = 10^{-8}$) in the top (bottom) panel. All curves assume minimum self-interaction, for which the current SK limit is rather weak and does not constrain the m_A–m_B space for the given choice of other parameters. In the second scenario with 10 years of construction and 3 years physics running, the SK-contour covers a little more in the higher mass (larger m_A) due to the longer exposure time, while a slightly larger m_B is probed at DUNE due to a lower threshold energy for a fixed value of m_A. If construction time can be reduced, *i.e.,* 5 years, then the signal significance at DUNE is superior as shown in the left panel, even if SK (HK) is (much) larger than DUNE 10 (DUNE 40) in volume.

Comparing results for BDM from the GC as shown in Fig. 4.3 (for $\varepsilon^2 = 2 \times 10^{-7}$), solar BDM is

less constrained by the CMB since the relevant parameter space is slightly moved up to a higher m_A region due to the evaporation and the energy loss. However, a larger portion of the mass space is more constrained by the direct detection of non-relativistic ψ_B ($m_B < 1$ GeV from DAMIC). On the other hand, BDM from the GC is constrained more by the CMB and less by DAMIC.

4.5 Detection of Boosted Dark Matter from the Earth

Finally we would like to comment on the detection prospects of boosted DM ψ_B from the Earth. As shown in Section 9.4 of Ref. [23], the ratio between the capture rates in the Sun and Earth is given by

$$C_c^{\rm Earth}/C_c^{\rm Sun} \approx 10^{-9}\,, \tag{4.29}$$

due to the much smaller mass ($M_\oplus/M_\odot \approx 3\times 10^{-6}$) and escape velocity ($v_{\rm esc}^\oplus/v_{\rm esc}^\odot \approx 10^{-2}$) of the Earth. In the case of no self-interaction and no evaporation, the boosted DM flux is simply proportional to C_c/R^2 where R is the distance between a detector and a source of the boosted DM. For the Earth, very tiny capture rates $C_c^{\rm Earth}$ can be compensated by the smaller distance from the source of the boosted DM. In the absence of self-interaction and evaporation, we find

$$\frac{\Phi_B^{\rm Earth}}{\Phi_B^{\rm Sun}} \approx \frac{C_c^{\rm Earth}}{C_c^{\rm Sun}}\frac{R_{\rm Sun}^2}{R_\oplus^2} \approx 0.5\,, \tag{4.30}$$

where $R_{\rm Sun} \simeq 1.5\times 10^8$ km is the distance between the Sun and the Earth and $R_\oplus \simeq 6.4\times 10^3$ km is the radius of the Earth. The evaporation effect is efficient only for a very low DM mass $m_{\rm DM} < 3-4$ GeV for the Sun, whereas it is important up to $m_{\rm DM} \lesssim 12$ GeV for the Earth due to the much smaller escape velocity of the Earth [232, 233, 243].

The DM self-capture rate C_s is proportional to N_χ (see Eq. (4.19)), and the seed of N_χ is determined by C_c since $N_\chi(0) = 0$. The smaller C_c therefore induces the smaller C_s, and consequently, self-capture is negligible for the Earth [235] since $C_c^{\rm Earth}/C_c^{\rm Sun} \approx 10^{-9}$. In summary, without self-interactions, $\Phi_B^{\rm Earth}$ could be comparable to $\sim 0.5\,\Phi_B^{\rm Sun}$ or less depending on $m_{\rm DM}$. However, with self-interactions, $\Phi_B^{\rm Earth}$

is much smaller than $\Phi_B^{\rm Sun}$ since self-capture is negligible for the Earth, while it enhances the flux significantly in the Sun.

Moreover the Earth is not a point-like source due to the short distance from the source unlike the Sun. Even if we consider only the inner core of the Earth, $R_{\rm in-core}^{\rm Earth} \approx 1.2 \times 10^3$ km, we should integrate over a $\sim 34^\circ$ cone around the center of the Earth. Thus, the background events by atmospheric neutrinos are governed by $\theta \simeq 34^\circ$ instead of the angular resolution of each experiment $\theta_{\rm res}$. Thus, even for the case of $\Phi_B^{\rm Earth} \approx \Phi_B^{\rm Sun}$, the final signal significance S for the Earth signals is much less than that for the Sun and the GC.

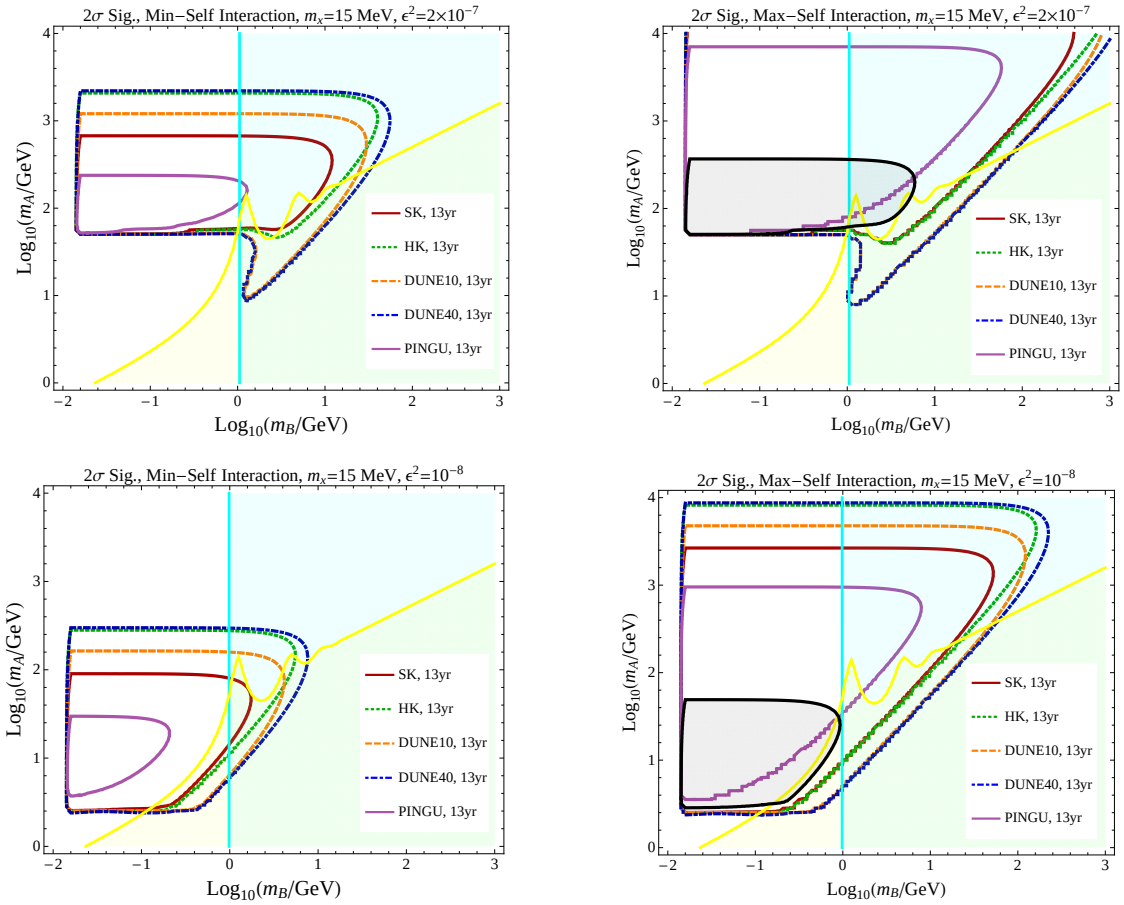

Fig. 4.7 2σ sensitivities of various detectors for $\varepsilon^2 = 2 \times 10^{-7}$ ($\varepsilon = 10^{-4}$) in the top (bottom) panel for Min (Max) SI in the left-panel (right-panel). For comparison, we assume all experiments to have been running over the same amount of time, which is 13.6 years. The gray-shaded region represents the current 2σ exclusion with all-sky data from SK, assuming 10% systematic uncertainty in the background estimation. The other shaded areas are potential bounds from direct detection of non-relativistic ψ_B (in cyan, with vertical boundary) and CMB constraints on ψ_B annihilation (in yellow, with diagonal boundary). Therefore the parameter space we are still able to probe is for BDM in the Sub-GeV region. When comparing all experiments, DUNE 40 and HK are ahead and have better sensitivity for BDM.

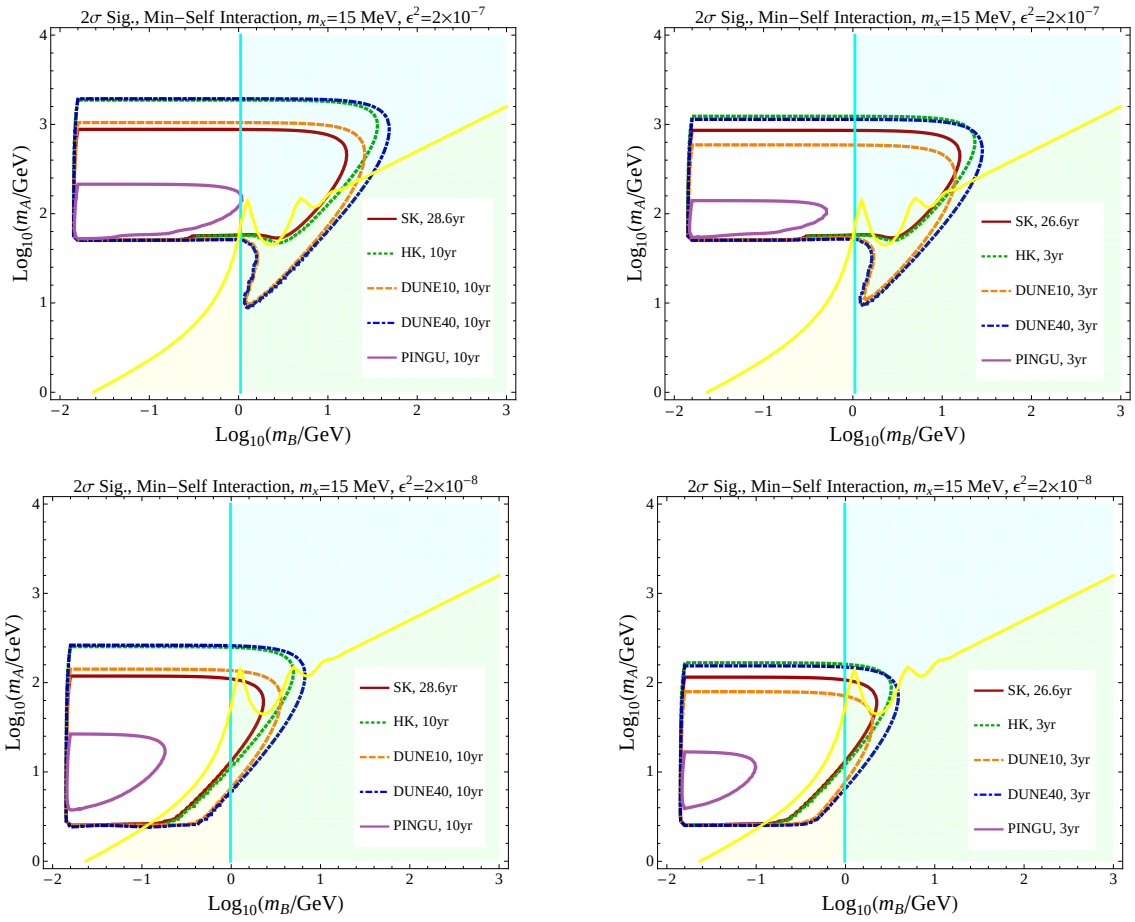

Fig. 4.8 2σ sensitivities assuming 5 years of construction and 10 years of physics running of DUNE/HK (left), and 10 years of construction and 3 years of physics running of DUNE/HK (right) for $\varepsilon^2 = 2\times10^{-7}$ ($\varepsilon = 10^{-4}$) in the top (bottom) panel. All curves assume Min SI. The shaded areas are potential bounds from direct detection of non-relativistic ψ_B (in cyan, with vertical boundary) and CMB constraints on ψ_B annihilation (in yellow, with diagonal boundary).

Part III

Simplified Model Framework

Effective field theories may provide a highly efficient manner to study DM physics. However, in case of a signal, interpretation and characterization would pose a challenge. We may therefore consider the possibility of a framework lying between model dependence and independence. This possibility arises in the form of simplified models. In this framework we have the ability to study DM through a minimal extension of the SM. This is done in such a way as to accommodate DM and ignore all the extra degrees of freedom in the model which do not have much contribution to the DM physics. In this part of the dissertation, we consider a simplified model involving two component dark matter which interacts with the SM through a SM Higgs boson.

We first introduce a simple $U(1)\prime$ extension of the SM where we describe the matter content of the model and discuss how the dark matter may be stabilized. After describing the model, we discuss the evolution of the two component DM system in the early Universe, showing which species is most dominant in the Universe when their masses are changed relative to each other.

We then study the phenomenology of both species as dark matter. To do this, we calculate the contribution that each species makes to the relic abundance of DM in the Universe. We further calculate the direct detection cross-section for each species scattering off nuclei in the detector. In this two component scenario the scattering cross-section for each DM is weighted by its contribution to the total DM relic abundance. Finally, if the DM particles are both lighter than the SM Higgs boson, they may contribute to the Higgs invisible width. We use the results from the invisible Higgs searches at the LHC as well as the relic abundance and direct detection to determine which part of our model parameter space is excluded and which is still available. We find that for a certain choice of couplings, a large part of the parameter space is ruled out by experiments and the parameter space still allowed occurs when the two species are of roughly equal mass. Again the excluded parts of parameter space give us an indication of what properties DM cannot have and leaves us to search further in the available parameter regions.

Chapter 5

Multicomponent Dark Matter through a Radiative Higgs Portal

As illustrated in chapter 4, scenarios with multiple dark matter particles are very well motivated and have illustrated very interesting phenomenology as well as the potential of providing “smoking gun" signatures in experiments on Earth. These types of scenarios may have further huge implications on the relic abundance of DM in the universe as well as for the detection of DM on the Earth. Studies of this type, when two or more DM particles are available, have shown much interest and promise in recent years.

Thus in the final chapter of this dissertation, we study a DM scenario which was in fact motivated by the study of chapter 4 as well as the study carried out in Ref. [244]. Here we investigate vector DM which alone cannot correctly account for the relic abundance in the current universe. The model we consider allows for a symmetry which stabilizes another DM candidate, where processes such as assisted freeze-out and semi-annihilation might be of importance. We investigate the interrelation of these two species, which interact with the SM through the Higgs Boson.

The SM has proven itself an important basis for the study of new physics. One example can be seen when studying the SM Higgs boson. The Higgs has a very important role to play in nature. As the

facilitator of electroweak symmetry breaking (EWSB), it can provide a window into new weak-scale physics beyond the SM. In particular, as the only elementary scalar in the SM, it can be the means through which new physics communicates with the SM. This can occur through the gauge invariant, low dimensional bilinear operator, $H^\dagger H$. As a consequence, fundamental questions such as the naturalness problem and the Higgs vacuum stability may be addressed by introducing new bosons which interact with the Higgs bilinear operator. These interactions can occur through a vector or scalar Higgs portal in the form of $\lambda H^\dagger H \Phi^\dagger \Phi$ and $\lambda H^\dagger H V^\mu V_\mu$ respectively, with λ being some dimensionless coupling. A further possibility is to have interactions of the Higgs with new heavy fermions through higher dimensional operators, a fermion Higgs portal. Any of these new particles can, in principle, constitute DM allowing for a direct glimpse into the dark sector.

In this study, we consider the model outlined in Ref. [244]. The phenomenology consists of a gauged, dark $U(1)'$ symmetry. The corresponding gauge boson, V, obtains a mass when the $U(1)'$ symmetry is spontaneously broken by a SM singlet scalar, Φ. Fermions charged under this $U(1)'$ and the SM Electroweak groups, are also introduced. A dark charge conjugation symmetry is imposed, which must not be broken when Φ receives a vev, so as to ensure stability of the vector. However, this requires the lightest of the new fermions to also be stable. Direct coupling of the vector to the Higgs is forbidden, which results in its interaction with the SM only at the radiative level.

This work is organized as follows. In Sec. 5.1, we provide a summary of the UV completion presented in Ref. [244] and expand on the stability mechanism. In Sec. 5.2 we discuss the evolution of the number density of the DM species considering different phenomenological scenarios. We evaluate the thermal relic density, the direct detection cross-section, and the invisible Higgs width in Sec. 5.3. This is followed by a discussion of how these observables constrain the model in Sec. 5.4.

5.1 The Radiative Higgs Model for Two Component DM

When writing down a UV completion to the typical Vector Higgs Portal ($H^\dagger H V^\mu V_\mu$), there are two previously proposed options. Both possibilities introduce a new gauge group, which when spontaneously

Table 5.1 Charge assignments for (1/2,0) Weyl fermions ψ, χ, and n and complex scalar Φ.

Field	$(SU(2)_W, U(1)_Y, U(1)')$	Field	$(SU(2)_W, U(1)_Y, U(1)')$
$\psi_{1\alpha}$	(2, 1/2, 1)	$\psi_{2\alpha}$	(2, 1/2, -1)
$\chi_{1\alpha}$	(2, -1/2, -1)	$\chi_{2\alpha}$	(2, -1/2, 1)
$n_{1\alpha}$	(1, 0, -1)	$n_{2\alpha}$	(1, 0, 1)
Φ	(1, 0, Q_Φ)		

broken generates a spin-1 dark matter candidate. The first portal is through mixing between the SM Higgs and the scalar which breaks the dark gauge group, resulting in a tree-level, mixing suppressed coupling between the Higgs and the vector [245–255]. The second option, which is of interest in this work, further introduces new fermions which carry dark and SM Electroweak charges. These fermions generate a loop-level coupling between the Higgs and vector [244].

The model explored in Ref. [244] proposes a $U(1)'$ whose gauge field is denoted as V. The model contains matter which is anomaly free and does not induce a kinetic mixing between the dark and SM gauge bosons. This is detailed in Sec. II of that work, which we summarize below.

The matter content of the model is given in Table 5.1 with the following mass and Higgs interaction terms for the fermions:

$$\begin{aligned}\mathscr{L} \supset & -m\,\varepsilon^{ab}\left(\psi_{1a}\chi_{1b}+\psi_{2a}\chi_{2b}\right)-m_n\,n_1n_2 \\ & -y_\psi\,\varepsilon^{ab}\left(\psi_{1a}H_bn_1+\psi_{2a}H_bn_2\right)-y_\chi\left(\chi_1H^*n_2+\chi_2H^*n_1\right)+h.c.\end{aligned} \tag{5.1}$$

In writing down this model, a $U(1)'$ charge conjugation (CC$'$) symmetry is imposed and whose transformation is given by the following prescription:

$$\begin{aligned} f_1 &\longleftrightarrow f_2 \\ V &\longrightarrow -V \\ \Phi &\longrightarrow \Phi^* \end{aligned} \tag{5.2}$$

Where f stands for the ψ, χ, and n fermions.

Imposing CC′ removes the tree-level kinetic mixing term between hypercharge and $U(1)'$, $F^{\mu\nu}F'_{\mu\nu}$, and aligns various Yukawa couplings and masses appearing in Eq. 5.1. Since we assume that $Q_\Phi \neq \pm 1$ and that the Higgs is not charged under the $U(1)'$, neither EWSB nor the spontaneous breaking of $U(1)'$ lead to CC′ violating terms.

One may be concerned that Φ spontaneously breaks CC′. One is free to rotate Φ using the global $U(1)'$, such that only the real component of Φ receives a vacuum expectation value. Under CC′, Φ transforms as $\mathrm{Im}(\Phi) \to -\mathrm{Im}(\Phi)$, therefore CC′ is left intact after $U(1)'$ is broken[1]. Note that the imaginary component of Φ, being the $U(1)'$ Goldstone boson, has the same transformations properties as V under CC′.

All perturbative processes which could break CC′ rely on a tree-level source of breaking. Therefore, with these assumptions, once this symmetry has been imposed at tree-level, it is preserved at every order in perturbation theory. V is odd under this symmetry, thus it can only decay to the new fermions. More precisely, if the fermions are heavy, i.e. $2M_f > M_V$, V is stable. This is in direct analogy to Furry's theorem of QED [256].

However, note that CC′ also forbids amplitudes with only one new fermion appearing in external lines. As pointed out in Ref. [244], the lightest new fermion is also stable and, therefore, another dark matter candidate.

Previous work on this model restricted itself to regimes where the fermions were heavy. In this work, we wish to explore the regime where one fermion is light enough to be a relevant degree-of-freedom in dark matter phenomenology. From the perspective of relic abundance, there are two effects which motivate investigating this case. First, the vector candidate annihilates more efficiently for lighter fermions, since the annihilation rate is suppressed by the mass of the fermion. Further, when the fermion running in the h-V-V loop can be on-shell, the imaginary component of the annihilation amplitude grows, as per the optical theorem. Second, when both the vector and fermion are present in the early universe, new annihilation channels are available, e.g. semi-annihilation. We further expect that the

[1] Alternatively, this may equivalently be seen without rotating Φ. For general $\theta = \mathrm{Arg}(\langle\Phi\rangle)$, both CC′ and the global $U(1)'$ break. However, the subgroup whose transformation is $\Phi \to e^{2i\theta}\Phi^*$ is preserved. This would be identified as the new CC′ symmetry.

fermion will often develop a non negligible contribution to the thermal relic, if light enough.

Ref. [244] showed how the SM gauge interactions of the fermions could play an important role in setting the relic abundance in this model. In that work, the gauge interactions presented themselves in box diagrams connecting external legs such as V-V-Z-Z and V-V-W-W. When dark matter is heavy enough, these processes further increase the dark matter annihilation cross-section. However, in the present work we wish to focus on the role that the fermions could play in setting the relic abundance as dark matter itself or at least as a degree-of-freedom present in the early universe. In order to better isolate this phenomena from the SM gauge interactions, we will primarily be interested on the part of parameter space where the SM gauge interactions are subdominant to the Higgs interactions. Further, we will make the additional simplifying assumptions that the lightest fermion is the only relevant fermion for the phenomenology and that the scalar degree of freedom may be ignored. This is essentially the "Single Fermion Limit" explored in Sec. III.A. of Ref. [244]. It is important to note that the above assumptions tend to be conservative, as including effects from the other fermions and their gauge interactions most often reduce the relic abundance with minimal changes to other observables, further opening up viable parameter space.

The SM gauge interactions will not be completely ignored. A coupling between the fermion and the Z boson, can have marked effects. This coupling can be very small, in fact choosing $y_\chi = y_\psi$ will only generate off-diagonal couplings between the neutral fermions and Z boson, without appreciably decreasing the corresponding Higgs couplings, e.g. see the third set of benchmark parameters in Ref. [244]. This alignment may need to be highly tuned to avoid the relevance of the Z boson, therefore we will investigate the phenomenological effect of this coupling. It is important to note that the diagonal coupling of the Z to the fermions is only axial. This can be see from CC$'$ symmetry. Taking Ψ to be a neutral fermion, we find that $\overline{\Psi}\gamma_\mu\Psi$ and V_μ are odd under CC$'$, whereas $\overline{\Psi}\gamma_\mu\gamma_5\Psi$ and Z_μ are even. Therefore, the Z can only have an axial coupling to a particular new fermion.

For the remainder of this chapter, we will denote the vector field as V and the lightest new fermion as N_1. The subscript on the fermion serves as a reminder that it is the lightest neutral state. Therefore we will be concerned with five parameters in our study:

- M_V: mass of vector, V
- M_{N_1}: mass of fermion, N_1
- g_V: $U(1)'$ gauge coupling
- Y_N: effective Yukawa coupling of N_1 to the Higgs
- c_z: parameter for N_1 coupling to Z boson

The simplified interaction Lagrangian is given by:

$$\mathscr{L} \supset g_V V^\mu \overline{N_1} \gamma_\mu N_1 + \frac{Y_N}{\sqrt{2}} h \overline{N_1} N_1 + \frac{e c_z}{2 c_w s_w} Z^\mu \overline{N_1} \gamma_\mu \gamma_5 N_1 \tag{5.3}$$

Here the Z coupling has been normalized such that $|c_z| \leq 1$.

Where necessary, we utilize `FeynArts`, `FormCalc` and `LoopTools` (see Appendix) to ensure that the full momentum and mass dependence of the loop-level processes are properly taken into account. For vector annihilation, this includes the box diagrams which become relevant above the two Higgs final state threshold. The full loop dependence was incorporated into `MicrOMEGAS` [40] to correctly account for the temperature dependence of the annihilation cross-section.

5.2 Thermal History of the Two Component System

The annihilation diagrams for the vector are given in Fig. 5.1. There are similar diagrams for the fermion; aside from cutting these loop diagrams, there is also a process through an s-channel Z as well as ZZ and ZH final state channels. There are also semi-annihilation channels shown in Fig. 5.2 and similar diagrams with the Z in place of the Higgs.

There are three classes of interactions in our model. There are the usual annihilation channels where the final states are SM fields. There are processes that don't involve SM fields in the final state, which convert one species of dark matter into another. Finally, there are semi-annihilation processes where the final state has a DM particle and a SM particle.

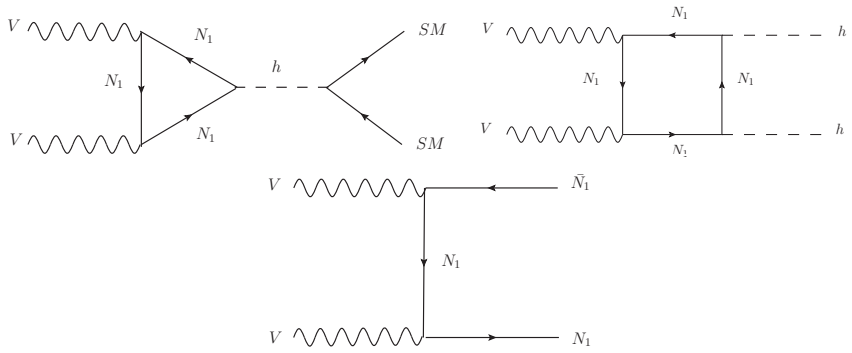

Fig. 5.1 Feynman diagrams showing the main annihilation channels for the vector dark matter.

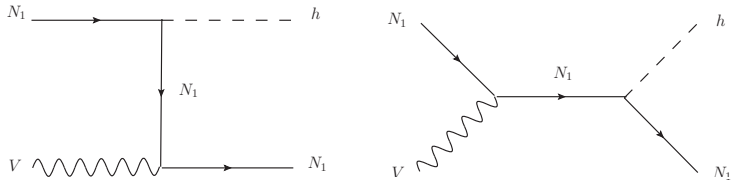

Fig. 5.2 Representative diagrams showing the coannihilation or semi-annihilation channels, relevant when the vector and the fermion have similar masses. Note that when considering couplings to the Z, similar diagrams exist with the Z in place of the Higgs.

This model has two distinct semi-annihilation channels. One reduces vector density without changing fermion density, $VN \to XN$. The second converts fermion density into vector, $N\overline{N} \to VX$. These rates will be most relevant when X is on-shell, since X must be the Higgs or Z, these rates are most relevant when V and N are relatively heavy. For $VN \to XN$, $M_V \gtrsim M_X$ whereas N could be lighter, so long as the vector abundance is not too Boltzmann suppressed. For $N\overline{N} \to VX$, we find that $2M_{N_1} \gtrsim M_V + M_X$. Interestingly, this process can still be relevant for V–N_1 mass splittings which would normally suggest that co-annihilation is irrelevant. Specifically, if the vector is heavier than the fermion such that the vector abundance is highly Boltzmann suppressed, vectors may still be produced by this process thereby reducing the total abundance. This breaks the phenomenology into three distinct regimes, where "much greater/less than" should be interpreted as one field's abundance being highly Boltzmann suppressed:

- $\underline{M_V \gg M_{N_1}}$: If M_V is too large to significantly effect the freeze-out of the fermion, typically

semi-annihilation is not relevant and conversion processes are not accessible. One caveat being processes such as $N_1\overline{N}_1 \to VH/Z$, which can be relevant for mass differences larger than would be expected based on typical semi-annihilation processes. Eqn. 5.4 nearly reduces to that of a Fermion Higgs Portal. The vector relic abundance is increasingly small for larger M_V, however note that when $M_V > 2M_{N_1}$, the vector is no longer stable and will not retain an abundance.

- $\underline{M_V \ll M_{N_1}}$: Likewise, if the fermion is very heavy it will not significantly effect the current day relic abundance as a degree-of-freedom, again reducing to a single component DM scenario composed of vector DM. However, note that the fermion is still necessary for the vector's loop interaction with the SM. Therefore, this interaction will be suppressed for larger fermion masses, making it increasingly difficult for the vector to be a thermal relic.

- $\underline{M_V \sim M_{N_1}}$: This scenario is the most phenomenologically rich. Here the masses are close enough that semi-annihilation and conversion processes may take place. The details of the freeze-out process will heavily depend on the couplings and masses chosen. It is this regime we wish to study in more detail in this work.

The evolution of the number density of dark matter is described by a set of coupled Boltzmann equations. These are parametrized in terms of the number of dark matter particles per comoving volume and entropy density of the Universe. The coupled Boltzmann equations for the different dark matter species is written as a function of the temperature $x = M_{N_1}/T$:

$$\begin{aligned}
x^2\frac{dY_{N_1}}{dx} &= -\lambda_{N_1\overline{N_1}\to XX}\left[Y_{N_1}^2 - (Y_{N_1}^{eq})^2\right] - \lambda_{N_1\overline{N_1}\to VV}\left[Y_{N_1}^2 - \left(\frac{Y_{N_1}^{eq}}{Y_V^{eq}}\right)^2 Y_V^2\right] \\
&\quad - \lambda_{N_1\overline{N_1}\to VX}\left[Y_{N_1}^2 - \frac{(Y_{N_1}^{eq})^2}{Y_V^{eq}}Y_V\right], \\
x^2\frac{dY_V}{dx} &= -\lambda_{VV\to XX}\left[Y_V^2 - (Y_V^{eq})^2\right] - \lambda_{VV\to N_1\overline{N_1}}\left[Y_V^2 - \left(\frac{Y_{N_1}^{eq}}{Y_V^{eq}}\right)^2 Y_{N_1}^2\right] \\
&\quad -\frac{1}{2}\lambda_{N_1V\to N_1X}\, Y_{N_1}\left[Y_V - Y_V^{eq}\right] + \frac{1}{2}\lambda_{N_1\overline{N_1}\to VX}\left[Y_{N_1}^2 - \frac{(Y_{N_1}^{eq})^2}{Y_V^{eq}}Y_V\right].
\end{aligned} \tag{5.4}$$

Where $\lambda_{ij\to kl} = \frac{s(x=1)}{H(x=1)}\langle\sigma v\rangle_{ij\to kl}$, with $\langle\sigma v\rangle_{ij\to kl}$ the thermally averaged annihilation cross-section of species i and j into species k and l. The quantity s is the entropy density of the Universe, H is the Hubble parameter, and Y_i^{eq} is the equilibrium number density per comoving volume for the different species:

$$Y_V^{eq} = \frac{g_1}{g_{*s}}\frac{45}{4\pi^4}r^2x^2K_2[rx], \quad Y_{N_1}^{eq} = \frac{g_2}{g_{*s}}\frac{45}{4\pi^4}x^2K_2[x]. \tag{5.5}$$

Here $g_1 = 3$ and $g_2 = 8$ are the number of internal degrees of freedom of the vector and fermion, respectively. $r = M_V/M_{N_1}$ is the ratio of the masses and $K_2[x]$ is the modified Bessel function. We obtain the solution for the coupled Boltzmann equations numerically, using the micrOMEGAS 4.2.5 package [40].

Typical thermal histories for the DM candidates are shown in Fig. 5.3. Note that even when the masses are degenerate, their respective thermal relics do not match. This is largely due to the fact that the vector couples to the SM at loop-level, therefore it annihilates at a slower rate and develops a greater thermal relic abundance. The presence of the fermion helps to maintain thermal equilibrium between the vector and the rest of the universe. However, upon freezing out, the fermion becomes a subdominant component of the total abundance. This phenomena is essentially the Assisted Freeze-out Mechanism [42].

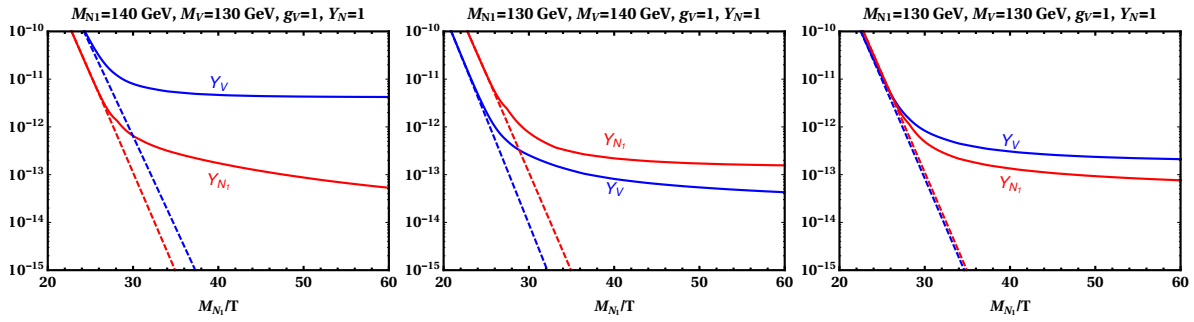

Fig. 5.3 Representative comoving number densities of the dark matter species after solving the coupled Boltzmann equations. The left and middle figures show the thermal history of the Universe when the lighter particle is the vector and fermion respectively. The right figure shows the thermal history when both the masses are degenerate. We choose $Y_N = 1$ and $g_V = 1$ as benchmark points. The heavier species freezes out earlier due to Boltzmann suppression, resulting in a lower relic abundance.

5.3 Phenomenology

Here we discuss the relevant sources of bounds, their corresponding formulae, and the methodology for setting limits.

5.3.1 Relic Abundance

In a scenario with multiple DM candidates, the relic density follows from the coupled Boltzmann equations, as discussed in Sec. 5.2, where the total predicted relic density from this model is the sum of the two components. However in order to examine the dependence of the relic abundance of each species on the parameters, we represent the relic abundance as a function of the masses of the DM states, as represented in Fig. 5.4. We define a mass splitting parameter:

$$\Delta = \frac{M_{N_1} - M_V}{M_V}. \tag{5.6}$$

Boltzmann suppression is determined by the relative mass difference, so Δ is useful as a crude measure of the relevance of co-annihilation processes. From Eq. 5.6 we notice that for negative values of Δ the fermion is lighter and therefore is typically the dominant dark matter component. Furthermore, for $\Delta < -1/2$, i.e. the vector mass is more than twice the fermion mass, CC$'$ no longer protects its stability and thus does not contribute to the total relic density. The transition in the relative contribution of each species to the relic abundance as a function of Δ is illustrated in Fig. 5.5, where $M_V = 100$ GeV.

Fig. 5.4 shows the total relic density for various parameters. In the left panel, the large dip in the relic density is due to resonant annihilation through an s-channel Higgs into SM states, which is the dominant annihilation process in this mass regime. At slightly larger masses, the relic density decreases near the threshold for annihilating to WW and ZZ. Another drop in the relic density occurs near the two Higgs final state threshold, which is mediated by both triangle and box diagrams represented in the top panels of Fig. 5.1. Semi-annihilation processes also become important in this high mass regime.

The right panel of Fig. 5.4 shows the relic for various mass splittings. For negative Δ, the fermion typically dominates, so the Higgs resonance will shift with the fermion mass accordingly, such that

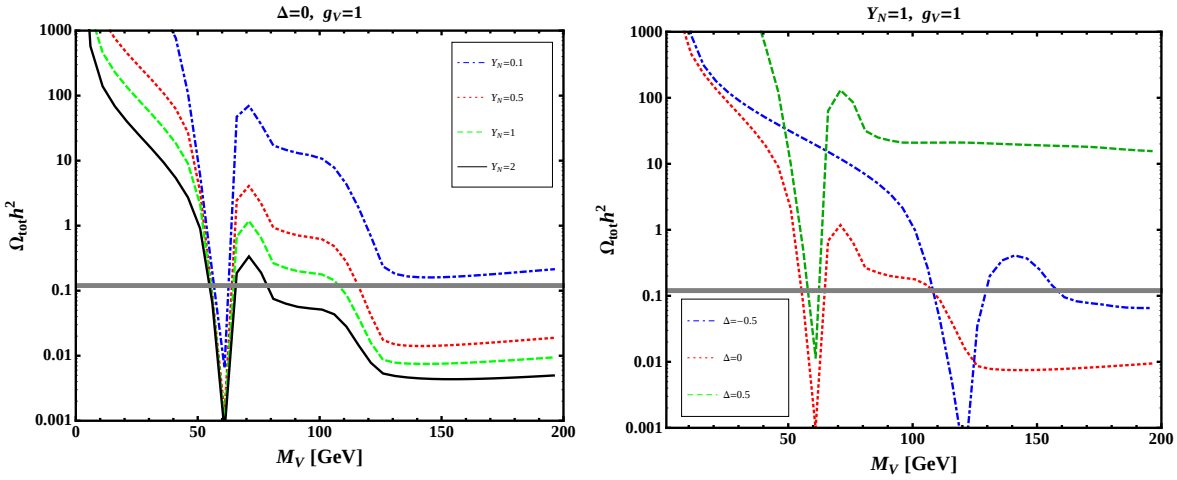

Fig. 5.4 Left: Relic density as function of the vector mass for different values of the Yukawa couplings and benchmark values for the mass splitting Δ and the gauge coupling g_V: The blue dashed curve represents $Y_N = 0.1$, red dotted $Y_N = 0.5$, green dashed $Y_N = 1$ and orange solid $Y_N = 2$. Right: Relic density as a function of the vector mass for benchmark values of the Yukawa and gauge couplings for different values of the mass splitting Δ; blue dot-dashed represents $\Delta = -0.5$, red dotted $\Delta = 0$ and green dashed $\Delta = 0.5$. The gray solid horizontal line represents the observed relic density of 0.12 [16].

$M_{N_1} = M_h/2$. The positive Δ benchmark given, shows an absence of the HH threshold. The large fermion mass running in the loop and the absence of a significant fermion relic density, suppresses processes of this form.

5.3.2 Direct Detection

The vector and the fermion dark matter species interact with nucleons through Higgs exchange and thus the scattering cross-section is spin-independent. The scattering with nucleons is illustrated in Fig. 5.6 and is calculated as:

$$\sigma_{SI}^{V} = \frac{Y_N^2 g_V^4 M_n^4}{4\pi(M_n + M_V)^2 M_h^4} \frac{f_n^2}{v^2} |F_0(M_{N_1}, M_V)|^2, \tag{5.7}$$

Where F_0 is a loop function defined in terms of the Passarino–Veltmann coefficients and can be found in the appendix of Ref. [58]. The scattering of N_1 with nucleons occurs through tree-level Higgs exchange and is written as,

$$\sigma_{SI}^{N_1} = \frac{Y_N^2 M_{N_1}^2 M_n^4}{2\pi(M_n + M_{N_1})^2 M_h^4} \frac{f_n^2}{v^2} \tag{5.8}$$

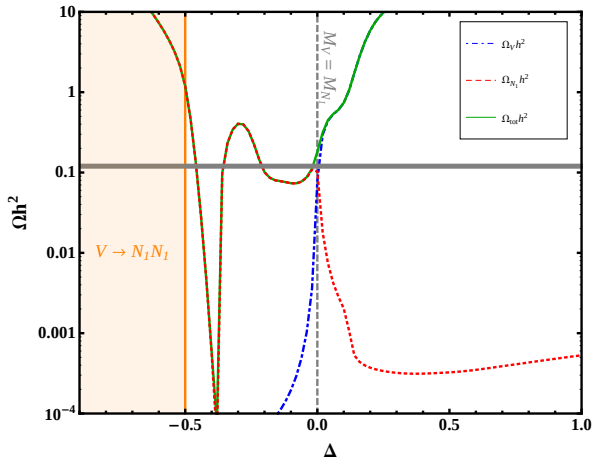

Fig. 5.5 The relative contributions of the vector and the fermion to the total relic density as a function of the mass splitting. The red dotted curve represents the contribution of the Fermion, blue dot-dashed, the contribution of the vector and green solid is the total relic density of the two species. The orange shaded region shows where the vector is heavy enough to decay into the fermion, while the grey dashed vertical line shows the value of Δ for which the vector and the fermion are degenerate. The gray solid line, again represents the observed relic density.

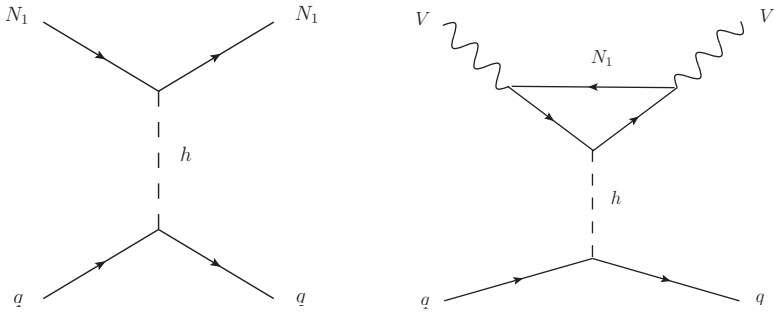

Fig. 5.6 Diagrams showing the scattering of the fermion (left panel) and of the vector, at loop level (right panel), with SM quarks. The scattering occurs through Higgs exchange and gives spin-independent rates.

f_n are the nucleon matrix elements defined as

$$f_n = \sum_{q=u,d,s} f_{T_q}^{(n)} + \frac{2}{9} f_{T_G}^{(n)}, \tag{5.9}$$

We use the hadronic matrix elements f_{T_q} obtained from DarkSUSY [257]. We define v in the equations above as the standard model Higgs vacuum expectation value and M_n the mass of the nucleon.

Current direct detection experiments have provided limits assuming that the local DM density consists of only one DM species. Thus, in a model with two DM candidates, those limits must be reinterpreted. In order to understand the limits set by experiments and properly apply them to our specific study, we consider the recoil rates measured by the direct detection experiments. The differential recoil rate on a target nucleus per recoil energy for a single DM particle scattering off a nucleus is defined as:

$$\frac{dR}{dE_R} = \frac{\sigma_{\chi N}^{(0)} \rho_\chi^{loc}}{2 M_\chi \mu_{\chi N}^2} F^2(E_R) I_\chi(E_R). \tag{5.10}$$

Where E_R is the recoil energy of the target nucleus, $\sigma_{\chi N}^{(0)}$ is the DM–nucleus cross-section at zero momentum transfer, $\rho_\chi^{loc} = 0.3$ GeV/cm^3 is the local energy density of dark matter. $\mu_{\chi N}$ is the reduced mass of the dark matter and Nucleus system, $F^2(E_R)$ is the nuclear form factor which depends on the recoil energy E_R. $I_\chi(E_R)$ is the velocity integral assuming some velocity distribution of the galactic dark matter halo, this depends on the minimum velocity required for a DM particle to cause a recoil, $V_{min} = \sqrt{2 E_R M_N / \mu_{\chi N}^2}$.

The DM–Nucleus cross-section can be written in terms of the DM–nucleon scattering cross-section, which is most often quoted by experiments, and atomic number A as

$$\sigma_{\chi N}^{(0)} = \frac{\mu_{\chi N}^2}{\mu_{\chi n}^2} \sigma_{\chi n}^{SI} A^2. \tag{5.11}$$

Eq. 5.10 can thus be represented as a function of the DM–nucleon scattering cross-section $\sigma_{\chi n}^{SI}$.

On the other hand when considering multiple DM particles forming part of the DM halo in the Milky way galaxy, one has to take into account the nuclear scattering of each species in the detector,

meaning we have to consider each particle's contribution to the local halo density and each particle's velocity distribution in the galactic halo. The total recoil rate then should account for each particle's recoil and thus is represented as:

$$\frac{dR}{dE_R} = \sum_i \frac{\sigma_{iN}^{(0)} \rho_i^{loc}}{2M_i \mu_{iN}^2} F^2(E_R) I_i(E_R). \tag{5.12}$$

Note that in general the local DM density need not have the same composition as the cosmological abundance. However, for simplicity we will assume that this is the case here, i.e. $\rho_i^{loc}/\rho_\chi^{loc} \sim \Omega_i/\Omega_\chi^{tot}$, with $\Omega_\chi^{tot} h^2 = 0.12$.

Following the formalism of Dynamical Dark Matter in [258] we obtain the recoil rates for our two component scenario as a function of the cross-section of each species scattering off nucleons. We represent the recoil rate, after taking into account the scattering from both species, as

$$\frac{dR}{dE_R} = \frac{\rho_\chi^{loc} A^2}{2} \left[\frac{\Omega_V h^2}{0.12} \frac{\sigma_{Vn}^{SI}}{\mu_{Vn}^2 M_V} I_V(E_R) + \frac{\Omega_{N_1} h^2}{0.12} \frac{\sigma_{N_1 n}^{SI}}{\mu_{N_1 n}^2 M_{N_1}} I_{N_1}(E_R) \right] F^2(E_R). \tag{5.13}$$

Here σ_{Vn}^{SI} and $\sigma_{N_1 n}^{SI}$ are the spin-independent DM–nucleon scattering cross-sections for the vector and the fermion species respectively, while I_V and I_{N_1} represent the velocity distributions of each of the species in the galaxy. From Eq. 5.13, we find that the two species have a nontrivial effect on the recoil spectra. To properly set direct detection limits on a two-species scenario, the full predicted recoil spectra should be compared to data. However, very often there is a large hierarchy in the scattering rates of the two species, such that one dominates the total scattering rate. If this is the case, an approximate limit may be set by requiring each species to independently satisfy:

$$\sigma_{DD}^{SI} \; > \; \frac{\Omega_i h^2}{0.12} \, \sigma_{in}^{SI}. \tag{5.14}$$

Here σ_{DD}^{SI} is the limit on the DM–nucleon scattering cross-section quoted by a direct detection experiment, such as LUX. σ_{in}^{SI} is the scattering cross-section between species i and a nucleon, predicted by the model. In the above, the predicted scattering cross-section has been weighted by the fractional abun-

dance of that species in accordance with Eq. 5.13. This approximation breaks down if the scattering rates of each species are similar, however such a scenario is rare due to the loop level scattering of the vector candidate. Also note that when this approximation breaks down, the limit on the scattering cross-section is underestimated by a factor of two, at most. This method leads to conservative limits on the model parameters. Note that we do not require the sum of both species to compose the entirety of the dark matter relic abundance. We use the most recent direct detection limits set by LUX [46] [1].

5.3.3 Invisible Higgs Width

If the mass of either of the DM species is lighter than half the Higgs, i.e. $M_i < M_h/2$, then that species will contribute to the Higgs width. The Higgs partial width into vectors is given by:

$$\Gamma_{h\to VV} = \frac{Y_N^2 g_V^4 \sqrt{1-4M_V^2/M_h^2}}{64\pi M_h}\left[M_h^4|A_{inv}|^2\left(1-4\frac{M_V^2}{M_h^2}+6\frac{M_V^4}{M_h^4}\right)\right.$$
$$\left. + 6\,\mathrm{Re}[A_{inv}^* B_{inv}]\, M_h^2\left(1-\frac{2M_V^2}{M_h^2}\right)+\frac{1}{2}|B_{inv}|^2\frac{M_h^4}{M_V^4}\left(1-4\frac{M_V^2}{M_h^2}+12\frac{M_V^4}{M_h^4}\right)\right]. \quad (5.15)$$

Where A_{inv} and B_{inv} are functions of the vector, fermion, and Higgs masses, the functional form of which can be found in the appendix of Ref. [58].

The decay channels of the Higgs are further opened as it can also decay into the fermion, N_1, with the decay width:

$$\Gamma_{h\to N_1N_1} = \frac{Y_N^2 M_h}{16\pi}\left(1-4\,\frac{M_{N_1}^2}{M_h^2}\right)^{3/2}. \quad (5.16)$$

Thus the total contribution to the invisible Higgs width becomes,

$$\Gamma_{h\to inv} = \Gamma_{h\to VV} + \Gamma_{h\to N_1N_1}. \quad (5.17)$$

The ATLAS collaboration constrains $\mathrm{Br}(h\to inv) < 0.23$ at 95% CL with $4.7 fb^{-1}$ of data at 7 TeV and $20.3 fb^{-1}$ at 8 TeV [259], which we use to constrain our parameter space.

[1] We point out here that the limits from the experiments are not rescaled, since these are what the experiments report assuming one DM component.

5.3.4 Z Couplings

Thus far the discussion has ignored couplings to the Z. For direct detection, the Z only induces SD and velocity suppressed SI direct detection cross-sections due to its axial coupling to the fermion. Unless the lightest fermion has an exceptionally small Yukawa coupling and large c_z, direct detection constraints are dominated by Higgs-exchange.

One may also consider constraints from the invisible Z width when the fermion is kinematically accessible, where new contributions should not exceed 2 MeV [242, 260]. The most stringent constraint on the coupling is in the limit where the fermion is massless, where the invisible Z width requires $|c_z| \lesssim 0.08$.

The most significant impact will be on setting the relic abundance. Note that s-channel annihilation through the Z to SM fermions is helicity suppressed, therefore the cross-section is suppressed by m_f^2 [261]. However, the s-channel annihilation through the Higgs has a similar suppression due to the SM Yukawas. Therefore, such processes may be important even when the top quark is not kinematically accessible. Fig. 5.8 shows limits when the z-couplings are included. The relic abundance constraint shows both the Higgs and Z resonances, however as is illustrated the Z resonance is only important in the region where the fermion is the dominant DM component as is expected. Increasing the Z coupling, increases the weight of the processes where both the vector and the fermion annihilate through the Z boson. In this region of annihilation through both the Higgs and Z, DM can over annihilate leaving a smaller relic abundance. Thus in the right figure in Fig. 5.8, the relic density lines showing Higgs and Z resonances disappears, though annihilation through the Higgs is still dominant.

5.4 Results

In Fig. 5.7, the contour of $\Omega h^2 = 0.12$ is shown in a solid black line for various benchmark parameters, as well as limits from the invisible Higgs width shown in blue. Regions which avoid these constraints lie inside the black contour and outside the blue shaded region.

The Higgs width excludes a large part of parameter space, nearly everywhere where the fermion

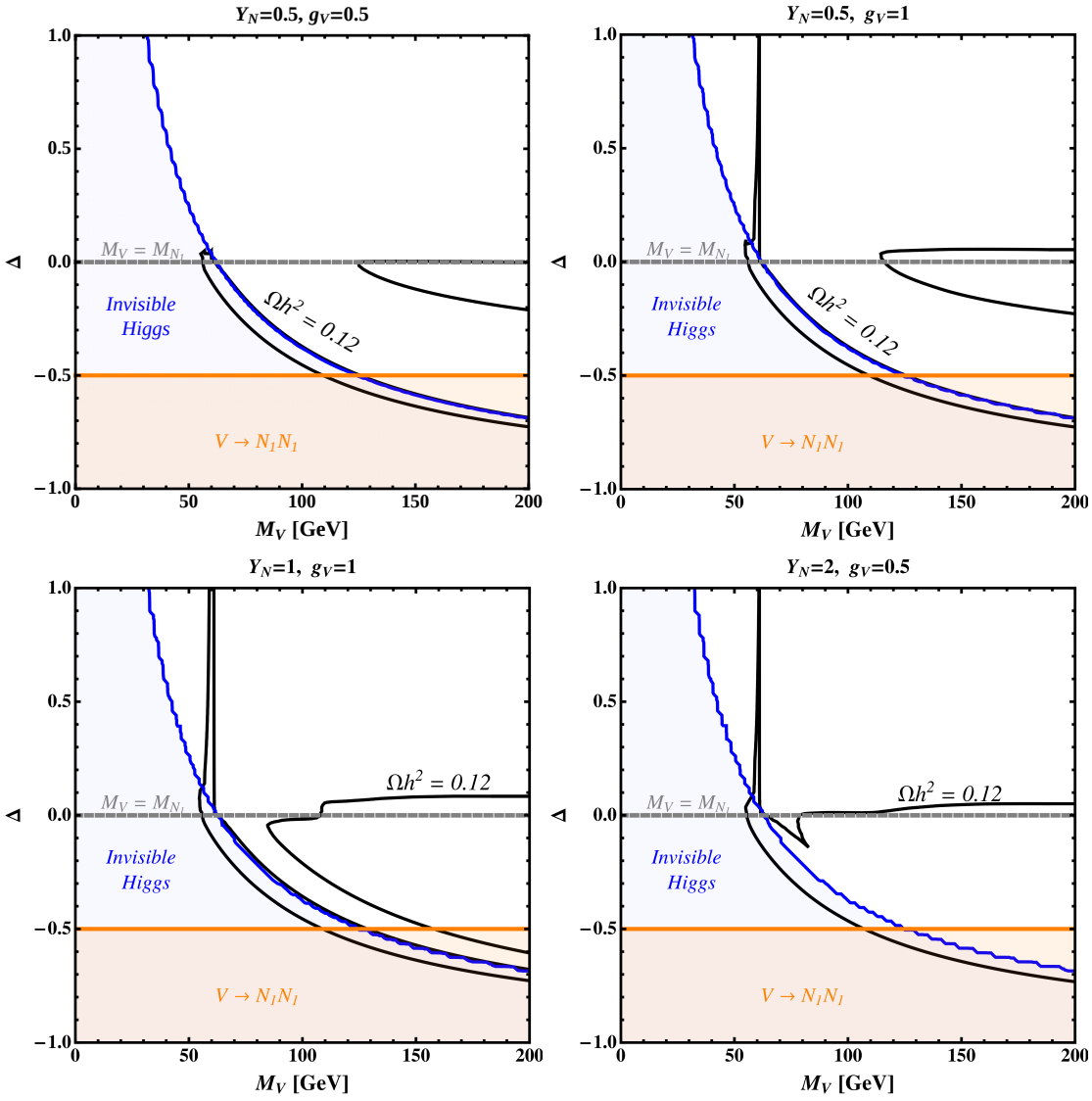

Fig. 5.7 Constraints from both relic abundance and Invisible Higgs measurements from the LHC, assuming $c_z = 0$. The orange shaded region shows where the vector decays into the fermion and we effectively have only one thermal DM component contributing to the relic abundance. Along the solid black curves, we have a relic abundance in agreement with the observed cosmological dark matter density. The grey dashed line represents $\Delta = 0$ and roughly indicates the point where there is a transition of the relative contributions of each species to the thermal relic abundance. The blue shaded region indicates the limits from the invisible Higgs searches. In order to satisfy the relic abundance requirement, while evading the bounds, we must be in the region of parameter space on or in between the black solid contours and outside the blue shaded region. On the outside of the contours, annihilation is not efficient and the Universe is over-closed.

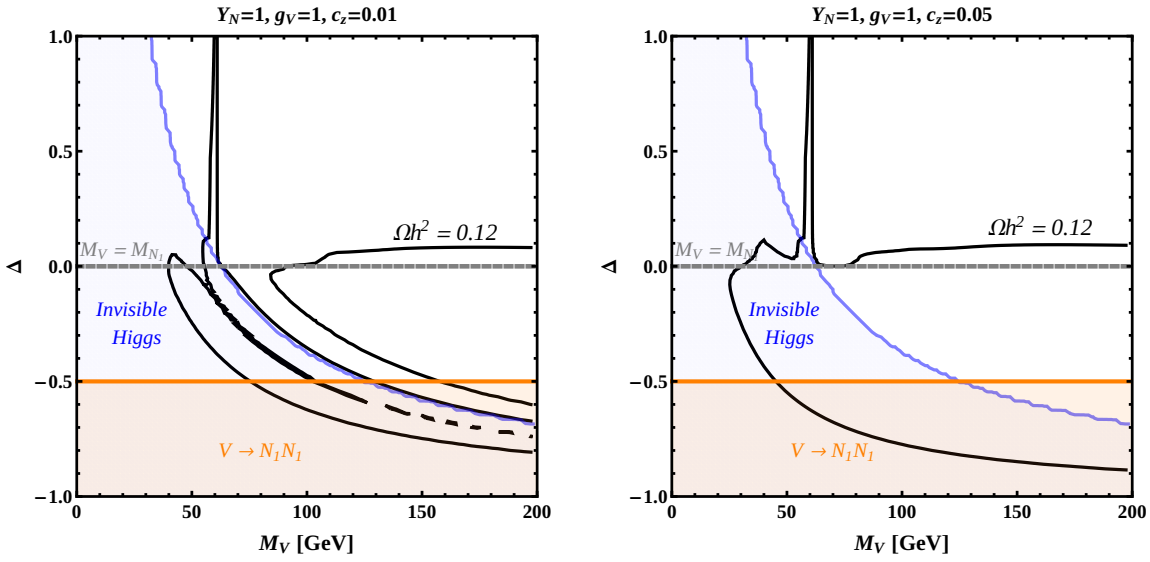

Fig. 5.8 Constraints from both relic abundance and Invisible Higgs measurements from the LHC, assuming $c_z = 0.01$ (left) and $c_z = 0.05$ (right). The orange shaded region shows where the vector decays into the fermion and we effectively have only one thermal DM component contributing to the relic abundance. Along the solid black curves, we have a relic abundance in agreement with the observed cosmological dark matter density. The grey dashed line represents $\Delta = 0$ and roughly indicates the point where there is a transition of the relative contributions of each species to the thermal relic abundance. The blue shaded region indicates the limits from the invisible Higgs searches. The left figure shows the contribution from the Z-boson, allowing more efficient annihilation and more areas of parameter space giving the correct relic abundance.

is kinematically accessible by Higgs decay. For relic abundance, we find a thin curved region which corresponds to resonant fermion annihilation through the Higgs, which is almost entirely excluded by the Higgs width. The thin vertical region with positive Δ corresponds to resonant vector annihilation through the Higgs. There is also a region at larger vector mass where diboson final states as well as semi-annihilation processes are kinematically accessible and dominate. Note that this region is mostly in the negative Δ regime where the vector abundance is Boltzmann suppressed due to its larger relative mass and rapid annihilation into fermions. The tree-level annihilation of the fermion allows for efficient annihilation. However, for the region near $\Delta = 0$, semi-annihilation becomes important and even allows a thermal relic up to roughly $\Delta = 0.1$ for some parameters.

Fig. 5.9 shows the limits from direct detection for $\Delta = 0$. Despite the fermion relic being a fraction

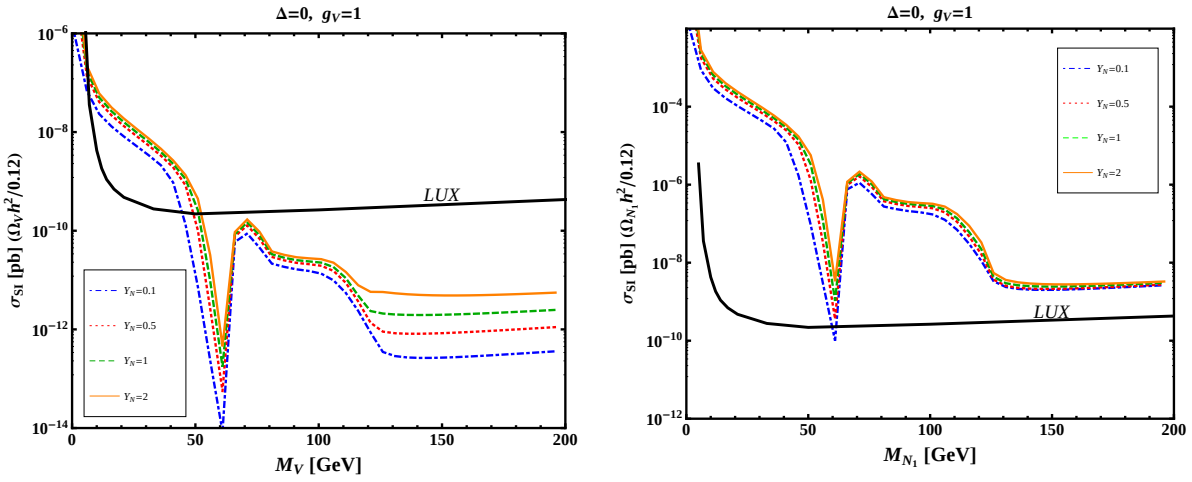

Fig. 5.9 Rescaled scattering cross-section (in pb) as a function of the mass of each DM species, (left) vector and (right) fermion. Each cross-section is rescaled according to its relative contribution to the observed relic density as indicated in Eq. 5.14. Each color line represents a different Yukawa coupling to the Higgs; for $Y_N = 0.1$ (blue dot-dashed), $Y_N = 0.5$ (red dotted), $Y_N = 1$ (green dashed) and $Y_N = 2$ (orange solid). The black solid line represents the most recent limits reported by LUX.

of the total dark matter abundance, it is not enough to suppress direct detection constraints. For typical s-wave processes, reducing the coupling has a small effect on the predicted $\langle \sigma_{DD} \rangle \times \Omega_{N_1} h^2$ since both the direct detection and annihilation cross-section scale with the coupling in the same way. However, the processes here are p-wave, where the relic abundance depends on a lower power of the freeze-out temperature compared to s-wave processes, i.e. T_f^{-2} rather than T_f^{-1}. Therefore, variations in the freeze-out temperature are more apparent, leading to deviations from the approximation that the relic density is inversely proportional to the annihilation cross-section. In fact, decreasing the Yukawa decreases the direct detection cross-section faster than it increases the relic abundance. In Fig. 5.9, we find that decreasing the Yukawa can satisfy direct detection constraints, as illustrated in Fig. 5.10. Unfortunately, in doing so this also causes these dark matter candidates to be overabundant. In fact there is very little room to simultaneously satisfy direct detection and be a thermal relic by solely altering the Yukawa. The only region which typically evades bounds is positive Δ and $M_V \sim M_h/2$, due to the resonant annihilation of vectors through the Higgs.

This difficulty is largely due to the presence of the fermion, which has a large direct detection

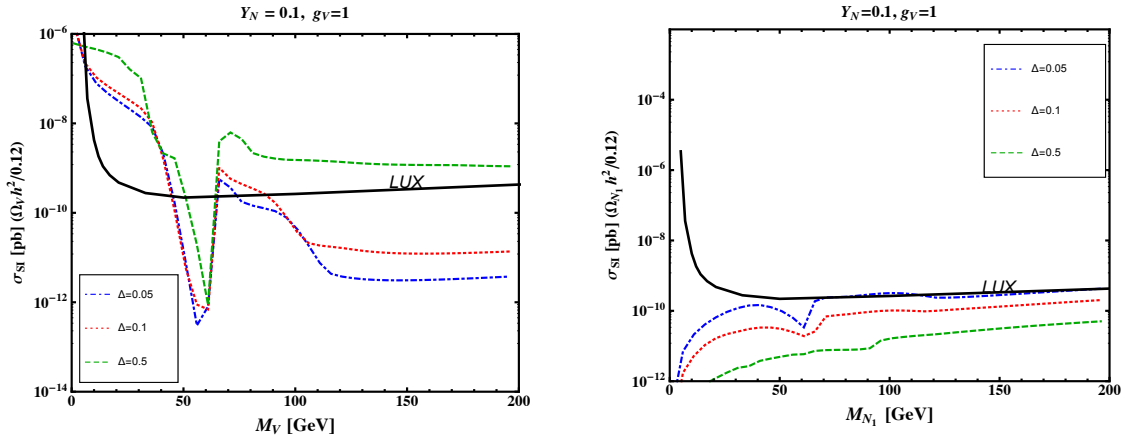

Fig. 5.10 Rescaled scattering cross-section (in pb) as a function of the mass of each DM species, (left) vector and (right) fermion. Each cross-section is rescaled according to its relative contribution to the observed relic density as indicated in Eq. 5.14. Each color line represents a different mass splitting; for $\Delta = 0.05$ (blue dot-dashed), $\Delta = 0.1$ (red dotted), $\Delta = 0.5$ (green dashed) for benchmark values of the Yukawa and gauge couplings. The black solid line represents the most recent limits reported by LUX.

scattering cross-section. For fermion masses above 20 GeV, the fermion must satisfy $Y_N^2\ \Omega h^2 \lesssim 10^{-4}$ in order to evade direct detection constraints. Masses below this are less constrained due to the direct detection threshold, however are heavily constrained by Higgs invisible constraints. Therefore, the fermion should be a subdominant component of the total dark matter abundance and/or have a small Yukawa coupling.

Phenomenologically interesting regions, i.e. where this model may explain a sizable portion of the dark matter abundance, are then restricted to scenarios where the dark matter is predominantly composed of the vector which has a comparably small direct detection cross-section.

There are two ways to reduce the fermion relic density without increasing the direct detection cross-section. The first is to increase g_V, the $U(1)'$ gauge coupling. Semi-annihilation rates will increase, and will be most effective for Δ near zero. For positive Δ, this also increases the rate that fermions convert into the vector candidate. However, if the fermion is too heavy to be a dynamical participant for the freeze-out of the vector DM, it suppresses the vector annihilation as it runs in the h-V-V loop. Therefore, the large gauge coupling is still necessary to compensate this suppression and allow for efficient vector annihilation.

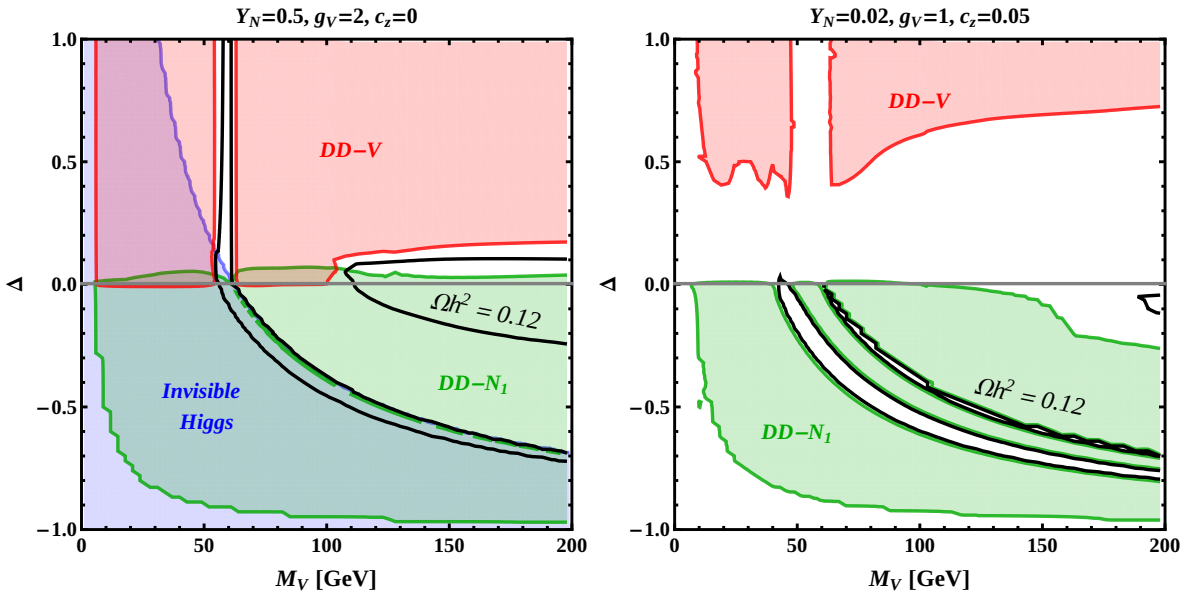

Fig. 5.11 Constraints from relic abundance, Invisible Higgs limits, and direct detection. Along the solid black curves, we have a relic abundance in agreement with the observed cosmological dark matter density. The blue shaded region indicates the limits from the invisible Higgs searches. The red and green shaded regions are excluded by the direct detection of the vector and fermion, respectively. On the left figure, in order to potentially accommodate DM we must lie in the Higgs resonance region or on the far right region near $\Delta = 0$. Decreasing the value of the Yukawa (as in the right figure) removes the invisible Higgs constraints, while increasing the $Z - N_1$ coupling opens more channels of annihilation and scattering off nuclei.

The left plot of Fig. 5.11 shows that this scenario can satisfy direct detection constraints and form a thermal relic. For these parameters, this is successful for $M_V \gtrsim 110$ GeV and $0.05 \lesssim \Delta \lesssim 0.15$, where N_1 makes up at most 1% of the total DM abundance. Resonant vector annihilation through the Higgs, e.g. $M_V \sim M_h/2$, with $\Delta \gtrsim 0.1$ can also avoid constraints. However, note that for larger values of Δ, both g_V and Y_N may be safely increased and can allow for a sufficiently small relic abundance for the vector candidate.

The second promising avenue is to consider new annihilation channels induced by couplings to the Z. Since the Z only couples directly to the fermion, this effect will be most relevant when the fermion is comparable in mass or lighter than the vector. Similar to the previous case, increasing c_z increases fermion–fermion annihilation as well as semi-annihilation processes such as $NV \to NZ$ and $N\overline{N} \to VZ$. A small Y_N will also be necessary to avoid direct detection constraints on the fermion. Further, if Y_N is small enough, the invisible Higgs constraints can be evaded which allows for fermions light enough to resonantly annihilate through the Z.

The right plot in Fig. 5.11 shows the available parameter space. In this case, the Yukawa is small enough such that Higgs invisible constraints are not relevant in this plane. The small Yukawa also severely reduces direct detection constraints. This set of parameters is viable for negative Δ, with $M_{N_1} \sim M_Z/2$ or $M_h/2$, where the fermion resonantly annihilates through an s-channel Z or Higgs, respectively. In this region, N_1 can make up all of the DM relic abundance, while V can at most make up 10% near $\Delta = 0$.

This is also viable for $M_V \gtrsim 190$ GeV with $-0.15 \lesssim \Delta \lesssim -0.05$, where specifically ZZ and VZ final states allow for efficient annihilation. Here, V makes up roughly 10% of the relic, with N_1 making up 50–90%. This latter window is not accessible to Z decays and therefore may be further opened by increasing c_z.

Chapter 6

Conclusions

Dark matter remains one of the most mysterious aspects of nature. The discovery of this elusive matter would be another triumph of modern physics and might point us to a fundamental higher energy theory for which the SM is a lower energy approximation. This would be a significant step in our quest to understanding nature.

One of the ultimate objectives in the field of (astro) particle physics is to find dark matter, characterize its properties and fit it to a theory which can explain how it interacts with the visible sector. Lack of a clear experimental signature for DM and the large number of possible candidates, makes studying and understanding its nature a challenge. The aim of this dissertation is to explore the phenomenology of dark matter and contribute to the ongoing search for its nature. We approached this dark matter problem by considering three main frameworks of study: (I) the model dependent direction, (II) model independent method using an effective field theory and (III) simplified models. Instead of concentrating on one particular framework, we explored in each direction novel DM scenarios that were highly theoretically and experimentally motivated. We investigated their current experimental constraints while highlighting their available parameter spaces at future experiments.

In chapter 1, we introduced DM and discussed its evidence, possible nature and available methods of detection. In the first part of the dissertation we focussed on the model dependent framework of study where we explored two extensions of the SM. In chapter 2, we extended the gauge symmetry

of the SM and studied a scenario which was motivated theoretically by parity violation in the SM and experimentally by the faint hint of a 2 TeV resonance in the data from run 1 of the LHC. Even in the absence of a collider signal this model favored novel dark matter signatures that had not been previously studied in the literature. Therefore, we explored dark matter in left-right extensions of the SM and found that the DM candidate can be a mixed state of fermionic multiplets. We limited this model to singlet-triplet, singlet-bidoublet, and triplet-bidoublet dark matter, and we found that an acceptable thermal relic abundance can be obtained for a wide range of masses in each of these cases. New gauge and Higgs bosons present in minimal left-right models provide the dominant interactions between the SM and dark sector, while scattering in direct detection experiments is largely governed by the tree-level exchange of the SM Higgs or Z'. Interestingly, stability of the lightest neutral state in the dark sector is guaranteed to all orders by $B-L$ gauge invariance for the models considered. The parameter space of the singlet-triplet model will be largely unconstrained by future experiments such as LUX-ZEPLIN and XENON1T. In contrast, these experiments will be able to thoroughly investigate models of thermal dark matter in the singlet-bidoublet and triplet-bidoublet cases. We have also taken note of interesting regions of parameter space where the branching fraction $\mathrm{BR}(W' \to \text{dark sector}) \gtrsim 10\%$. Such large invisible branching fractions are needed if we would like to have the theoretically attractive choice of $g_R = g_L$, giving us left-right symmetry and parity restoration at higher energy scales. Continuing in the model dependent direction, in chapter 3, we extended the space-time symmetry of the SM to include one extra spatial dimension. These types of scenarios were theoretically attractive for solving the gauge hierarchy problem. We limited our study to non-SUSY scenarios and investigated DM in the context of Non-Minimal Universal Extra Dimensions. We found that the inclusion of bulk masses and boundary-localized kinetic terms significantly change the phenomenological properties of the KK dark matter. A linear combination of the KK weak boson and KK hypercharge gauge boson forms the lightest Kaluza-Klein particle (LKP), which we call electroweak Kaluza-Klein dark matter. Depending on the parameter choice, the electroweak Kaluza-Klein dark matter may be mainly KK Z-boson like or KK photon-like. In this study, we performed all the detailed derivation of KK weak mixing angles with KK mass spectra and their couplings with the standard model particles taking only the brane localized

kinetic terms for electroweak gauge bosons into account. We then compared our theoretical expectations with the existing experiments ranging from electroweak precision tests, LHC resonance searches as well as dark matter direct detection experiments to determine the parameter space compatible with current observations. We identified the upper limit on the KK dark matter mass to be 2.4 TeV, which is significantly higher than the conventionally quoted value at 1.3 TeV in minimal UED models. The heavier regime above a TeV will be tested at future experiments such as LUX Zeplin (LZ) as well as at future LHC resonance searches.

In part II of the dissertation, i.e in chapter 4 we focused our attention on the model independent approach. We studied DM in the context of multiple stable states. These types of scenario are very well motivated, especially in the context of providing a solution to the small scale astrophysical problems and fitting astrophysical data. In order to avoid many model assumptions and to focus more on the prospective new DM signal, we incorporated an effective field theory to study boosted DM. We investigated a scenario where two DM candidates have a large mass gap, with the heavier one as the dominant component in our Universe while the lighter one is subdominant. The heavier candidate is secluded from the SM sector without any tree-level interaction, while the lighter one interacts with the SM via light dark photon exchange. Although subdominant, the lighter DM particles are produced with a large Lorentz boost by the present-day annihilation of the heavier counterpart in the GC or in the center of the Sun. We determined the detection prospects of BDM from the GC at various neutrino telescopes, including SK, HK, PINGU and DUNE. We investigated the discovery potential of DUNE for BDM arising from the Sun and compared the results with those for the detectors based on Cherenkov radiation such as SK and HK as well as at future Ice detectors such as PINGU. We found that when searching for this type of signal LArTPC detectors are of particular interest as they provide excellent particle identification, which can be used in the background reduction in search for a BDM signal. An angular resolution of 1° which significantly reduces backgrounds while retaining the same amount of signal events is a further advantage of a LArTPC and in particular we found that a point-like source such as the Sun benefits greatly from this good angular resolution. Furthermore, we found that a lower

threshold energy of 30 MeV increases the signal sensitivity in the relevant parameter space. As a result, the strength of the DUNE detector is remarkable, especially for the solar BDM.

Other potential bounds arise from dark photon searches, direct detection of non-relativistic particles (both heavy and light ones), indirect detection of the non-relativistic candidate, CMB constraints on the annihilation of the lighter DM candidate, BBN constraints on the lighter one, and DM searches at colliders. In our scenario with two DM candidates, the most important bounds were obtained from the CMB and the direct detection of the lighter DM candidate. However, these bounds are model-dependent and can be evaded in a different setup.

We illustrated that it is very promising to look for BDM particles, especially from the Sun, at DUNE with a LArTPC detector. We found that the performance of DUNE (10 kTon or 40 kTon) is much better than that of SK or even HK and is especially better than that of PINGU, for the same exposure time, even if their volumes are smaller. In order to compete with the others, PINGU due to its worse angular resolution and higher energy threshold, would require much larger exposure times. Finally, searches for BDM particles coming from the GC and from the center of the Sun are complementary, since the allowed parameter space that is accessible to one is not to the other. For instance, $m_A \gtrsim 100$ GeV may be better probed with the solar BDM, while $m_A \lesssim 100$ GeV is well covered for the GC BDM.

Finally, in part III of the dissertation i.e. in chapter 5, we investigated a radiative Higgs portal emerging from a simplified model. We explored another multicomponent DM model which comes from a simple extension of the SM. This model is theoretically favored by the type of interactions the SM Higgs can have with the dark sector. In this scenario we found that a vector and fermion dark matter naturally arise from a dark sector $U(1)'$. Both states are stabilized by an imposed dark charge conjugation symmetry. The vector can annihilate through a Higgs portal at the radiative level, with the fermion running in the loop and the fermion can annihilate at tree level through the Higgs. We explored the phenomenology of this model considering relic abundance, direct detection, and constraints from Invisible Higgs searches at the LHC. This model is highly constrained by the direct detection of the fermion candidate, requiring that it compose a small fraction of the total relic abundance. Constraints may be avoided by decreasing the Yukawa coupling while increasing the $U(1)'$ gauge coupling. The increased

gauge coupling helps to enhance semi-annihilation, conversion of N_1 into V, and V annihilation; while further reducing direct detection constraints on N_1.

The fermion coupling to the Z may also be increased to enhance new semi-annihilation channels as well as annihilation through a Z resonance and ZZ final state processes. Since the Z only couples axially to N_1, contributions to direct detection are spin-dependent or velocity suppressed, therefore, increasing this coupling may be done with little recourse from direct detection. Invisible Z width constraints are also easily evaded. Furthermore, when studying the bounds from direct detection, experiments typically set their bounds assuming only one DM component in the galactic halo, this assumption although based on the minimal nature of DM need not be "cast in stone". It has been illustrated in this study and many others that multicomponent dark sectors are substantiative and could well be where DM lies. As such, it would be a fair assumption for future experiments to make; that the DM in our Galaxy has more than one component. This in turn could provide unexpected and intriguing results.

In summary, what we have done in this dissertation is tried to contribute to the ongoing search for the answer to "what is dark matter?" Of course this is a very big question and to answer it will involve a large amount of collaboration between the theory and experimental communities. We attempt to answer this big question, by asking smaller questions such as "where do we begin to search for DM?" However, this question is also particularly challenging to answer due to the vast possibilities that DM can attain, for which exhaustive searches appear improbable.

We have illustrated in this dissertation that there are many ways to approach studies of DM and there are several points from which to start. We showed this by considering three frameworks of study and demonstrated that we may start from the SM and build from the top-down, extending in a model dependent manner. Alternatively we may consider general model independent theories, constructed from the bottom-up without worrying about the underlying theory, and finally we may simplify our models concentrating only on the DM physics. As illustration, in each of the frameworks we focused on DM scenarios which were very well motivated from the theoretical as well as experimental perspective. In these scenarios we not only studied the constraints from current experiments, indicating what DM

cannot be, we also illuminated where DM might lie and might be found by future experiments. In fact, in some of the studies considered here, we presented new physics scenarios that have wide implications for future experiments, presenting us with unique and unambiguous signals that would provide a "smoking gun" signature of dark matter if found.

Each of the frameworks considered in this document contain advantages and disadvantages, yet they provide a structure in which to study DM. Concentrating our attentions only on model dependent methods we are faced with the challenge that the phenomenology depends on certain assumptions entering into the model. This makes it difficult to study the model parameter space in an unbiased manner. However, if we do find a signal, we will be looking at particular models for characterization of the DM properties. Model independent frameworks, on the other hand, allow us to concentrate on the potential DM signal and physics at hand without worrying about many assumptions and theoretical constraints. Yet, it is very difficult to interpret signals in this very general framework. Simplified models allow us to study DM by considering very simple extension of the SM, while ignoring all the extra physics not contributing to the DM phenomenology. Rather than focussing on the individual directions of pursuit, we may be better served by connecting them under one main idea of a balanced phenomenological plan. Individually each framework may only tell us a fraction of the valuable information we seek. Yet, together they have the ability push us forward. For instance, with effective theories or simplified models we can study and focus on potential signals or interpreting the hints we get from experimental searches. Once a definitive signal is found, these theories may be matched onto a complete theory where the signal can be fully characterized and the nature of DM determined.

The studies considered in this dissertation contribute to the ideas and methods of studying and finding DM by illustrating a systematic approach of investigation. A systematic approach certainly maybe what is needed to provides us with ideas which can help us understand what theories are better suited for our experiments. By considering these types of approaches, we may even discover more exotic possibilities and new methods of detection that would allow us to build new experiments sensitive to dark matter. In our search for DM, we may be better served by keeping an open mind and considering the various possibilities, from the traditional scenarios to especially those that provide less expected

solutions.

The fields of particle physics and astrophysics are at a pivotal point. The experimental progress we have made over the past decades have helped us better understand our theoretical models. The null results at past and current experiments have ruled out certain parts of the DM parameter space, thus indicating what DM is not. This has paved a way forward for us to construct better phenomenological models and build better experiments sensitive to our searches. Thus our hunt for new physics, be it at colliders or from astrophysical phenomena should bear some fruit within the next decade or so. During this time, the field of (astro)particle physics will be transformed with a blast of experimental and technological progress set to put the most promising ideas to the test. Our field is a very dynamic one and it is simply impossible to predict the direction it will take a few years down the line. This makes the studies contained in this dissertation as well as those of a similar nature particularly important. The ability to study different aspects in the realm of possibility makes hunting in the dark more worthwhile and certainly adds to the joys of being a theoretical particle physicist.

Appendix A

Description of Public Packages

A.1 Feynrules

`Feynrules` is a package written in Mathematica. It is used to implement particle physics models, these are usually very complicated and it is impossible to calculate all the observables one needs in a reasonable amount of time, by hand. One implements the particle fields involved as well as their properties and implements their interactions in a Lagrangian. `Feynrules` takes this information and calculates the Feynman rules for every possible interaction and then produces files in the appropriate format which can be used in other programs, i.e. `MicrOMEGAs` for the calculation of the relic abundance. Model implementation is not easy as one has to know and understand the model as well as the interactions of the different particles. For further information please see Ref. [262].

A.2 MicrOMEGAs

`MicrOMEGAs` is publicly available C code that takes the output from `Feynrules` in `CH` format and calculates the relic abundance as well as other dark matter properties for a generic model. Please see Refs. [40, 263] for further information. This is code is widely used in the particle physics community and has undergone various checks against analytic results for various models.

A.3 MadDM

MadDM, is a fairly new dark matter tool which takes output from Feynrules in UFO format and calculates the relic abundance as well as direct detection rates in a generic dark matter model. While MicrOMEGAs uses the CalcHEP format, MadDM uses the MG5_aMC@NLO format which is based on Fortran and Python. For more information please see Ref. [177]. MadDM is currently under further development and will be able do automated loop computations for DM studies in the near future.

A.4 CalcHEP

CalcHEP is an automated package for computing tree-level decays and collisions of elementary particles. It is written in C and uses the CH output from Feynrules. Thus one starts at Lagrangian level in Feynrules and ends up with particles physics observables, in principle simulating the type of particle collisions that occur in particle colliders. For more information please see Ref. [264]

A.5 MadGraph5_aMC@NLO

MG5_aMC@NLO is a computational tool for simulating elementary particle collisions. It uses the UFO output from Feynrules to compute all the necessary aspects of particle physics phenomenology. This ranges from particle decays and cross-sections to event generation and matching. MG5_aMC@NLO can be linked with particle showering simulation tools as well as detector simulation tools, allowing for the most efficient studies of particle collider phenomenology. For more information please see Ref. [265]

A.6 FeynArts

FeynArts is a tool written in Mathematica for the computation and visualization of Feynman diagrams as well as their amplitudes in a generic particle physics model. One of its main uses is the generation of counter-terms in the computations of loop level diagrams. Please see Ref. [266].

A.7 FormCalc

`FormCalc` is a Mathematica package to the calculation of Feynman diagrams. It uses the output of `FeynArts` to compute the amplitudes for tree-level and loop-level diagrams in either Fortran or C (fror numerical computations) or Mathematica (for analytical computations). Please see Ref. [267].

A.8 LoopTools

`LoopTools` is computational tool for the evaluation of one loop integrals. It may use the output from `FormCalc` to compute the integrals. Please see Ref. [268].

References

[1] Matts Roos. Dark Matter: The evidence from astronomy, astrophysics and cosmology. 2010.

[2] Marco Regis. *Aspects of wimp dark matter*. PhD thesis, SISSA, Trieste, 2008. URL `http://hdl.handle.net/1963/5246`.

[3] Edward W. Kolb and Michael S. Turner. The Early Universe. *Front. Phys.*, 69:1–547, 1990.

[4] Douglas Clowe, Marusa Bradac, Anthony H. Gonzalez, Maxim Markevitch, Scott W. Randall, Christine Jones, and Dennis Zaritsky. A direct empirical proof of the existence of dark matter. *Astrophys. J.*, 648:L109–L113, 2006. doi: 10.1086/508162.

[5] De-Chang Dai, Reijiro Matsuo, and Glenn Starkman. Gravitational Lenses in Generalized Einstein-Aether theory: The Bullet Cluster. *Phys. Rev.*, D78:104004, 2008. doi: 10.1103/PhysRevD.78.104004.

[6] Gianfranco Bertone, Dan Hooper, and Joseph Silk. Particle dark matter: Evidence, candidates and constraints. *Phys. Rept.*, 405:279–390, 2005. doi: 10.1016/j.physrep.2004.08.031.

[7] A. G. Doroshkevich, V. N. Lukash, and E. V. Mikheeva. A solution to the problems of cusps and rotation curves in dark matter halos in the cosmological standard model. *Phys. Usp.*, 55:3–17, 2012. doi: 10.3367/UFNe.0182.201201a.0003.

[8] Katherine Freese. Review of Observational Evidence for Dark Matter in the Universe and in upcoming searches for Dark Stars. *EAS Publ. Ser.*, 36:113–126, 2009. doi: 10.1051/eas/0936016.

[9] P. Salucci and M. Persic. Dark matter halos around galaxies. 1996. [ASP Conf. Ser.117,1(1997)].

[10] A. Burkert. Do dwarf spheroidal galaxies contain dark matter? *Astrophys. J.*, 474:L99, 1997. doi: 10.1086/310433.

[11] Eduardo Battaner and Estrella Florido. The Rotation curve of spiral galaxies and its cosmological implications. *Fund. Cosmic Phys.*, 21:1–154, 2000.

[12] Eduardo Battaner and J. Jimenez-Vicente. A simple model of magnetically induced warps. *Astron. Astrophys.*, 332:809, 1998.

[13] Eduardo Battaner, E. Florido, and J. Jimenez-Vicente. Magnetic fields and large scale structure in a radiation dominated universe. *Astron. Astrophys.*, 326:13–22, 1997.

[14] Jonathan L. Feng. Dark Matter Candidates from Particle Physics and Methods of Detection. *Ann. Rev. Astron. Astrophys.*, 48:495–545, 2010. doi: 10.1146/annurev-astro-082708-101659.

[15] Graciela Gelmini and Paolo Gondolo. DM Production Mechanisms. pages 121–141, 2010.

[16] P. A. R. Ade et al. Planck 2015 results. XIII. Cosmological parameters. *Astron. Astrophys.*, 594: A13, 2016. doi: 10.1051/0004-6361/201525830.

[17] Kim Griest and David Seckel. Three exceptions in the calculation of relic abundances. *Phys. Rev.*, D43:3191–3203, 1991. doi: 10.1103/PhysRevD.43.3191.

[18] Dan Hooper. Particle Dark Matter. In *Proceedings of Theoretical Advanced Study Institute in Elementary Particle Physics on The dawn of the LHC era (TASI 2008): Boulder, USA, June 2-27, 2008*, pages 709–764, 2010. doi: 10.1142/9789812838360_0014. URL `http://lss.fnal.gov/cgi-bin/find_paper.pl?conf-09-025`.

[19] Daniel J. H. Chung, Patrick Crotty, Edward W. Kolb, and Antonio Riotto. On the gravitational production of superheavy dark matter. *Phys. Rev.*, D64:043503, 2001. doi: 10.1103/PhysRevD.64.043503.

[20] Gian Francesco Giudice, Edward W. Kolb, and Antonio Riotto. Largest temperature of the radiation era and its cosmological implications. *Phys. Rev.*, D64:023508, 2001. doi: 10.1103/PhysRevD.64.023508.

[21] Graciela Gelmini and Carlos E. Yaguna. Constraints on Minimal SUSY models with warm dark matter neutralinos. *Phys. Lett.*, B643:241–245, 2006. doi: 10.1016/j.physletb.2006.10.063.

[22] Stephen P. Martin. A Supersymmetry primer. 1997. doi: 10.1142/9789812839657_0001,10.1142/9789814307505_0001. [Adv. Ser. Direct. High Energy Phys.18,1(1998)].

[23] Gerard Jungman, Marc Kamionkowski, and Kim Griest. Supersymmetric dark matter. *Phys. Rept.*, 267:195–373, 1996. doi: 10.1016/0370-1573(95)00058-5.

[24] Frank Daniel Steffen. Gravitino dark matter and cosmological constraints. *JCAP*, 0609:001, 2006. doi: 10.1088/1475-7516/2006/09/001.

[25] E. J. Chun, Jihn E. Kim, and Hans Peter Nilles. Axino mass. *Phys. Lett.*, B287:123–127, 1992. doi: 10.1016/0370-2693(92)91886-E.

[26] Kyoungchul Kong and Konstantin T. Matchev. Precise calculation of the relic density of Kaluza-Klein dark matter in universal extra dimensions. *JHEP*, 01:038, 2006. doi: 10.1088/1126-6708/2006/01/038.

[27] Geraldine Servant and Timothy M. P. Tait. Is the lightest Kaluza-Klein particle a viable dark matter candidate? *Nucl. Phys.*, B650:391–419, 2003. doi: 10.1016/S0550-3213(02)01012-X.

[28] Hsin-Chia Cheng, Jonathan L. Feng, and Konstantin T. Matchev. Kaluza-Klein dark matter. *Phys. Rev. Lett.*, 89:211301, 2002. doi: 10.1103/PhysRevLett.89.211301.

[29] Bogdan A. Dobrescu, Dan Hooper, Kyoungchul Kong, and Rakhi Mahbubani. Spinless photon dark matter from two universal extra dimensions. *JCAP*, 0710:012, 2007. doi: 10.1088/1475-7516/2007/10/012.

[30] Ayres Freitas and Kyoungchul Kong. Two universal extra dimensions and spinless photons at the ILC. *JHEP*, 02:068, 2008. doi: 10.1088/1126-6708/2008/02/068.

[31] Bob Holdom. Two U(1)'s and Epsilon Charge Shifts. *Phys. Lett.*, B166:196–198, 1986. doi: 10.1016/0370-2693(86)91377-8.

[32] P. Sikivie. Caustic rings of dark matter. *Phys. Lett.*, B432:139–144, 1998. doi: 10.1016/S0370-2693(98)00595-4.

[33] Mikhail Shaposhnikov and Igor Tkachev. The nuMSM, inflation, and dark matter. *Phys. Lett.*, B639:414–417, 2006. doi: 10.1016/j.physletb.2006.06.063.

[34] Graham D. Kribs, Tuhin S. Roy, John Terning, and Kathryn M. Zurek. Quirky Composite Dark Matter. *Phys. Rev.*, D81:095001, 2010. doi: 10.1103/PhysRevD.81.095001.

[35] Kathryn M. Zurek. Multi-Component Dark Matter. *Phys. Rev.*, D79:115002, 2009. doi: 10.1103/PhysRevD.79.115002.

[36] Partha Konar, Kyoungchul Kong, Konstantin T. Matchev, and Myeonghun Park. Dark Matter Particle Spectroscopy at the LHC: Generalizing M(T2) to Asymmetric Event Topologies. *JHEP*, 04:086, 2010. doi: 10.1007/JHEP04(2010)086.

[37] Mayumi Aoki, Michael Duerr, Jisuke Kubo, and Hiroshi Takano. Multi-Component Dark Matter Systems and Their Observation Prospects. *Phys. Rev.*, D86:076015, 2012. doi: 10.1103/PhysRevD.86.076015.

[38] Keith R. Dienes, Jason Kumar, Brooks Thomas, and David Yaylali. Dark-Matter Decay as a Complementary Probe of Multicomponent Dark Sectors. *Phys. Rev. Lett.*, 114(5):051301, 2015. doi: 10.1103/PhysRevLett.114.051301.

[39] M. Demianski and A. G. Doroshkevich. Cosmology beyond the standard model: Multi-component dark matter model. *Astron. Rep.*, 59(6):491–493, 2015. doi: 10.1134/S1063772915060128.

[40] G. Bélanger, F. Boudjema, A. Pukhov, and A. Semenov. micrOMEGAs 4.1: two dark matter candidates. *Comput. Phys. Commun.*, 192:322–329, 2015. doi: 10.1016/j.cpc.2015.03.003.

[41] Francesco D'Eramo and Jesse Thaler. Semi-annihilation of Dark Matter. *JHEP*, 06:109, 2010. doi: 10.1007/JHEP06(2010)109.

[42] Genevieve Belanger and Jong-Chul Park. Assisted freeze-out. *JCAP*, 1203:038, 2012. doi: 10.1088/1475-7516/2012/03/038.

[43] Mikhail V. Medvedev. Cosmological Simulations of Multicomponent Cold Dark Matter. *Phys. Rev. Lett.*, 113(7):071303, 2014. doi: 10.1103/PhysRevLett.113.071303.

[44] Marco Cirelli, Alessandro Strumia, and Matteo Tamburini. Cosmology and Astrophysics of Minimal Dark Matter. *Nucl. Phys.*, B787:152–175, 2007. doi: 10.1016/j.nuclphysb.2007.07.023.

[45] J. L. Feng et al. Planning the Future of U.S. Particle Physics (Snowmass 2013): Chapter 4: Cosmic Frontier. In *Proceedings, Community Summer Study 2013: Snowmass on the Mississippi (CSS2013): Minneapolis, MN, USA, July 29-August 6, 2013*, 2014. URL `http://inspirehep.net/record/1278570/files/arXiv:1401.6085.pdf`.

[46] D. S. Akerib et al. Results from a search for dark matter in the complete LUX exposure. *Phys. Rev. Lett.*, 118(2):021303, 2017. doi: 10.1103/PhysRevLett.118.021303.

[47] Andi Tan et al. Dark Matter Results from First 98.7 Days of Data from the PandaX-II Experiment. *Phys. Rev. Lett.*, 117(12):121303, 2016. doi: 10.1103/PhysRevLett.117.121303.

[48] C. Amole et al. Dark Matter Search Results from the PICO-60 C_3F_8 Bubble Chamber. 2017.

[49] J. Billard, L. Strigari, and E. Figueroa-Feliciano. Implication of neutrino backgrounds on the reach of next generation dark matter direct detection experiments. *Phys. Rev.*, D89(2):023524, 2014. doi: 10.1103/PhysRevD.89.023524.

[50] David N. Spergel. The Motion of the Earth and the Detection of Wimps. *Phys.Rev.*, D37:1353, 1988. doi: 10.1103/PhysRevD.37.1353.

[51] Philipp Grothaus, Malcolm Fairbairn, and Jocelyn Monroe. Directional Dark Matter Detection Beyond the Neutrino Bound. *Phys.Rev.*, D90:055018, 2014. doi: 10.1103/PhysRevD.90.055018.

[52] Asher Berlin, Patrick J. Fox, Dan Hooper, and Gopolang Mohlabeng. Mixed Dark Matter in Left-Right Symmetric Models. *JCAP*, 1606(06):016, 2016. doi: 10.1088/1475-7516/2016/06/016.

[53] Nima Arkani-Hamed, Savas Dimopoulos, and G. R. Dvali. The Hierarchy problem and new dimensions at a millimeter. *Phys. Lett.*, B429:263–272, 1998. doi: 10.1016/S0370-2693(98)00466-3.

[54] Nima Arkani-Hamed, Savas Dimopoulos, and G. R. Dvali. Phenomenology, astrophysics and cosmology of theories with submillimeter dimensions and TeV scale quantum gravity. *Phys. Rev.*, D59:086004, 1999. doi: 10.1103/PhysRevD.59.086004.

[55] Thomas Flacke, Dong Woo Kang, Kyoungchul Kong, Gopolang Mohlabeng, and Seong Chan Park. Electroweak Kaluza-Klein Dark Matter. *JHEP*, 04:041, 2017. doi: 10.1007/JHEP04(2017)041.

[56] Kyoungchul Kong, Gopolang Mohlabeng, and Jong-Chul Park. Boosted dark matter signals uplifted with self-interaction. *Phys. Lett.*, B743:256–266, 2015. doi: 10.1016/j.physletb.2015.02.057.

[57] Haider Alhazmi, Kyoungchul Kong, Gopolang Mohlabeng, and Jong-Chul Park. Boosted Dark Matter at the Deep Underground Neutrino Experiment. *JHEP*, 04:158, 2017. doi: 10.1007/JHEP04(2017)158.

[58] Anthony DiFranzo and Gopolang Mohlabeng. Multi-component Dark Matter through a Radiative Higgs Portal. *JHEP*, 01:080, 2017. doi: 10.1007/JHEP01(2017)080.

[59] Georges Aad et al. Search for high-mass diboson resonances with boson-tagged jets in proton-proton collisions at $\sqrt{s} = 8$ TeV with the ATLAS detector. *JHEP*, 12:055, 2015. doi: 10.1007/JHEP12(2015)055.

[60] Vardan Khachatryan et al. Search for resonances and quantum black holes using dijet mass spectra in proton-proton collisions at $\sqrt{s} = 8$ TeV. *Phys. Rev.*, D91(5):052009, 2015. doi: 10.1103/PhysRevD.91.052009.

[61] Georges Aad et al. Search for new phenomena in the dijet mass distribution using $p-p$ collision data at $\sqrt{s} = 8$ TeV with the ATLAS detector. *Phys. Rev.*, D91(5):052007, 2015. doi: 10.1103/PhysRevD.91.052007.

[62] CMS Collaboration. Search for massive WH resonances decaying to $\ell\nu b\bar{b}$ final state in the boosted regime at $\sqrt{s} = 8$ TeV. 2015.

[63] Vardan Khachatryan et al. Search for massive resonances decaying into pairs of boosted bosons in semi-leptonic final states at $\sqrt{s} = 8$ TeV. *JHEP*, 08:174, 2014. doi: 10.1007/JHEP08(2014)174.

[64] Bogdan A. Dobrescu and Zhen Liu. W' Boson near 2 TeV: Predictions for Run 2 of the LHC. *Phys. Rev. Lett.*, 115(21):211802, 2015. doi: 10.1103/PhysRevLett.115.211802.

[65] Johann Brehmer, JoAnne Hewett, Joachim Kopp, Thomas Rizzo, and Jamie Tattersall. Symmetry Restored in Dibosons at the LHC? *JHEP*, 10:182, 2015. doi: 10.1007/JHEP10(2015)182.

[66] P. S. Bhupal Dev and R. N. Mohapatra. Unified explanation of the $eejj$, diboson and dijet resonances at the LHC. *Phys. Rev. Lett.*, 115(18):181803, 2015. doi: 10.1103/PhysRevLett.115.181803.

[67] Matti Heikinheimo, Martti Raidal, and Christian Spethmann. Testing Right-Handed Currents at the LHC. *Eur. Phys. J.*, C74(10):3107, 2014. doi: 10.1140/epjc/s10052-014-3107-9.

[68] Arindam Das, Natsumi Nagata, and Nobuchika Okada. Testing the 2-TeV Resonance with Trileptons. *JHEP*, 03:049, 2016. doi: 10.1007/JHEP03(2016)049.

[69] Jogesh C. Pati and Abdus Salam. Lepton Number as the Fourth Color. *Phys. Rev.*, D10: 275–289, 1974. doi: 10.1103/PhysRevD.10.275,10.1103/PhysRevD.11.703.2. [Erratum: Phys. Rev.D11,703(1975)].

[70] Rabindra N. Mohapatra and Jogesh C. Pati. Left-Right Gauge Symmetry and an Isoconjugate Model of CP Violation. *Phys. Rev.*, D11:566–571, 1975. doi: 10.1103/PhysRevD.11.566.

[71] R. N. Mohapatra and Jogesh C. Pati. A Natural Left-Right Symmetry. *Phys. Rev.*, D11:2558, 1975. doi: 10.1103/PhysRevD.11.2558.

[72] G. Senjanovic and Rabindra N. Mohapatra. Exact Left-Right Symmetry and Spontaneous Violation of Parity. *Phys. Rev.*, D12:1502, 1975. doi: 10.1103/PhysRevD.12.1502.

[73] R. E. Marshak and Rabindra N. Mohapatra. Quark - Lepton Symmetry and B-L as the U(1) Generator of the Electroweak Symmetry Group. *Phys. Lett.*, B91:222–224, 1980. doi: 10.1016/0370-2693(80)90436-0.

[74] Rabindra N. Mohapatra and R. E. Marshak. Local B-L Symmetry of Electroweak Interactions, Majorana Neutrinos and Neutron Oscillations. *Phys. Rev. Lett.*, 44:1316–1319, 1980. doi: 10.1103/PhysRevLett.44.1316. [Erratum: Phys. Rev. Lett.44,1643(1980)].

[75] R. N. Mohapatra. *UNIFICATION AND SUPERSYMMETRY. THE FRONTIERS OF QUARK - LEPTON PHYSICS*. Springer, Berlin, 1986. ISBN 978-1-4757-1930-7, 978-1-4757-1928-4. doi: 10.1007/978-1-4757-1928-4.

[76] Paul Langacker. Grand Unified Theories and Proton Decay. *Phys. Rept.*, 72:185, 1981. doi: 10.1016/0370-1573(81)90059-4.

[77] JoAnne L. Hewett and Thomas G. Rizzo. Low-Energy Phenomenology of Superstring Inspired E(6) Models. *Phys. Rept.*, 183:193, 1989. doi: 10.1016/0370-1573(89)90071-9.

[78] Sofiane M. Boucenna, Martin B. Krauss, and Enrico Nardi. Dark matter from the vector of SO (10). *Phys. Lett.*, B755:168–176, 2016. doi: 10.1016/j.physletb.2016.02.008.

[79] Georges Aad et al. Analysis of events with b-jets and a pair of leptons of the same charge in pp collisions at $\sqrt{s} = 8$ TeV with the ATLAS detector. *JHEP*, 10:150, 2015. doi: 10.1007/JHEP10(2015)150.

[80] Pilar Coloma, Bogdan A. Dobrescu, and Jacobo Lopez-Pavon. Right-handed neutrinos and the 2 TeV W' boson. *Phys. Rev.*, D92(11):115023, 2015. doi: 10.1103/PhysRevD.92.115023.

[81] CMS Collaboration. Search for massive resonances decaying into pairs of boosted W and Z bosons at $\sqrt{s}$ = 13 TeV. 2015.

[82] The ATLAS collaboration. Search for diboson resonances in the $\nu\nu qq$ final state in pp collisions at $\sqrt{s}$ =13 TeV with the ATLAS detector. 2015.

[83] The ATLAS collaboration. Search for diboson resonances in the llqq final state in pp collisions at $\sqrt{s}$ = 13 TeV with the ATLAS detector. 2015.

[84] The ATLAS collaboration. Search for WW/WZ resonance production in the $\ell\nu qq$ final state at $\sqrt{s} = 13$ TeV with the ATLAS detector at the LHC. 2015.

[85] Julian Heeck and Sudhanwa Patra. Minimal Left-Right Symmetric Dark Matter. *Phys. Rev. Lett.*, 115(12):121804, 2015. doi: 10.1103/PhysRevLett.115.121804.

[86] Camilo Garcia-Cely and Julian Heeck. Phenomenology of left-right symmetric dark matter. *JCAP*, 2015. doi: 10.1088/1475-7516/2016/03/021. [JCAP1603,021(2016)].

[87] Miha Nemevsek, Goran Senjanovic, and Yue Zhang. Warm Dark Matter in Low Scale Left-Right Theory. *JCAP*, 1207:006, 2012. doi: 10.1088/1475-7516/2012/07/006.

[88] F. Bezrukov, H. Hettmansperger, and M. Lindner. keV sterile neutrino Dark Matter in gauge extensions of the Standard Model. *Phys. Rev.*, D81:085032, 2010. doi: 10.1103/PhysRevD.81.085032.

[89] J. N. Esteves, J. C. Romao, M. Hirsch, W. Porod, F. Staub, and A. Vicente. Dark matter and LHC phenomenology in a left-right supersymmetric model. *JHEP*, 01:095, 2012. doi: 10.1007/JHEP01(2012)095.

[90] Haipeng An, P. S. Bhupal Dev, Yi Cai, and R. N. Mohapatra. Sneutrino Dark Matter in Gauged Inverse Seesaw Models for Neutrinos. *Phys. Rev. Lett.*, 108:081806, 2012. doi: 10.1103/PhysRevLett.108.081806.

[91] Subhaditya Bhattacharya, Ernest Ma, and Daniel Wegman. Supersymmetric left-right model with radiative neutrino mass and multipartite dark matter. *Eur. Phys. J.*, C74:2902, 2014. doi: 10.1140/epjc/s10052-014-2902-7.

[92] P. Duka, J. Gluza, and M. Zralek. Quantization and renormalization of the manifest left-right symmetric model of electroweak interactions. *Annals Phys.*, 280:336–408, 2000. doi: 10.1006/aphy.1999.5988.

[93] Bogdan A. Dobrescu and Zhen Liu. Heavy Higgs bosons and the 2 TeV W$^?$ boson. *JHEP*, 10:118, 2015. doi: 10.1007/JHEP10(2015)118.

[94] Bogdan A. Dobrescu and Patrick J. Fox. Signals of a 2 TeV W' boson and a heavier Z' boson. *JHEP*, 05:047, 2016. doi: 10.1007/JHEP05(2016)047.

[95] Monika Blanke, Andrzej J. Buras, Katrin Gemmler, and Tillmann Heidsieck. Delta F = 2 observables and $B \to X_q$ gamma decays in the Left-Right Model: Higgs particles striking back. *JHEP*, 03:024, 2012. doi: 10.1007/JHEP03(2012)024.

[96] Vardan Khachatryan et al. Search for heavy neutrinos and W bosons with right-handed couplings in proton-proton collisions at $\sqrt{s} = 8\,\text{TeV}$. *Eur. Phys. J.*, C74(11):3149, 2014. doi: 10.1140/epjc/s10052-014-3149-z.

[97] Marco Cirelli, Nicolao Fornengo, and Alessandro Strumia. Minimal dark matter. *Nucl. Phys.*, B753:178–194, 2006. doi: 10.1016/j.nuclphysb.2006.07.012.

[98] Marco Cirelli and Alessandro Strumia. Minimal Dark Matter: Model and results. *New J. Phys.*, 11:105005, 2009. doi: 10.1088/1367-2630/11/10/105005.

[99] Eugenio Del Nobile, Marco Nardecchia, and Paolo Panci. Millicharge or Decay: A Critical Take on Minimal Dark Matter. *JCAP*, 1604(04):048, 2016. doi: 10.1088/1475-7516/2016/04/048.

[100] Asher Berlin. Diphoton and diboson excesses in a left-right symmetric theory of dark matter. *Phys. Rev.*, D93(5):055015, 2016. doi: 10.1103/PhysRevD.93.055015.

[101] Durmus A. Demir, Mariana Frank, and Ismail Turan. Neutralino dark matter in the left-right supersymmetric model. *Phys. Rev.*, D73:115001, 2006. doi: 10.1103/PhysRevD.73.115001.

[102] Lisa Goodenough and Dan Hooper. Possible Evidence For Dark Matter Annihilation In The Inner Milky Way From The Fermi Gamma Ray Space Telescope. 2009.

[103] Dan Hooper and Lisa Goodenough. Dark Matter Annihilation in The Galactic Center As Seen by the Fermi Gamma Ray Space Telescope. *Phys.Lett.*, B697:412–428, 2011. doi: 10.1016/j.physletb.2011.02.029.

[104] Dan Hooper and Tim Linden. On The Origin Of The Gamma Rays From The Galactic Center. *Phys.Rev.*, D84:123005, 2011. doi: 10.1103/PhysRevD.84.123005.

[105] Tansu Daylan, Douglas P. Finkbeiner, Dan Hooper, Tim Linden, Stephen K. N. Portillo, Nicholas L. Rodd, and Tracy R. Slatyer. The characterization of the gamma-ray signal from the central Milky Way: A case for annihilating dark matter. *Phys. Dark Univ.*, 12:1–23, 2016. doi: 10.1016/j.dark.2015.12.005.

[106] Francesca Calore, Ilias Cholis, and Christoph Weniger. Background model systematics for the Fermi GeV excess. *JCAP*, 1503:038, 2015. doi: 10.1088/1475-7516/2015/03/038.

[107] M. Ajello et al. Fermi-LAT Observations of High-Energy γ-Ray Emission Toward the Galactic Center. *Astrophys. J.*, 819(1):44, 2016. doi: 10.3847/0004-637X/819/1/44.

[108] Seyda Ipek, David McKeen, and Ann E. Nelson. A Renormalizable Model for the Galactic Center Gamma Ray Excess from Dark Matter Annihilation. *Phys. Rev.*, D90(5):055021, 2014. doi: 10.1103/PhysRevD.90.055021.

[109] Asher Berlin, Stefania Gori, Tongyan Lin, and Lian-Tao Wang. Pseudoscalar Portal Dark Matter. *Phys. Rev.*, D92:015005, 2015. doi: 10.1103/PhysRevD.92.015005.

[110] D. S. Akerib et al. Improved Limits on Scattering of Weakly Interacting Massive Particles from Reanalysis of 2013 LUX Data. *Phys. Rev. Lett.*, 116(16):161301, 2016. doi: 10.1103/PhysRevLett.116.161301.

[111] P. Cushman et al. Working Group Report: WIMP Dark Matter Direct Detection. In *Community Summer Study 2013: Snowmass on the Mississippi (CSS2013) Minneapolis, MN, USA, July 29-August 6, 2013*, 2013. URL `http://inspirehep.net/record/1262767/files/arXiv:1310.8327.pdf`.

[112] Richard J. Hill and Mikhail P. Solon. Standard Model anatomy of WIMP dark matter direct detection II: QCD analysis and hadronic matrix elements. *Phys. Rev.*, D91:043505, 2015. doi: 10.1103/PhysRevD.91.043505.

[113] M. Ackermann et al. Searching for Dark Matter Annihilation from Milky Way Dwarf Spheroidal Galaxies with Six Years of Fermi Large Area Telescope Data. *Phys. Rev. Lett.*, 115(23):231301, 2015. doi: 10.1103/PhysRevLett.115.231301.

[114] Dan Hooper, Chris Kelso, and Farinaldo S. Queiroz. Stringent and Robust Constraints on the Dark Matter Annihilation Cross Section From the Region of the Galactic Center. *Astropart. Phys.*, 46:55–70, 2013. doi: 10.1016/j.astropartphys.2013.04.007.

[115] Galle Giesen, Mathieu Boudaud, Yoann Gnolini, Vivian Poulin, Marco Cirelli, Pierre Salati, and Pasquale D. Serpico. AMS-02 antiprotons, at last, Secondary astrophysical component and immediate implications for Dark Matter. *JCAP*, 1509(09):023, 2015. doi: 10.1088/1475-7516/2015/09/023,10.1088/1475-7516/2015/9/023.

[116] Hong-Bo Jin, Yue-Liang Wu, and Yu-Feng Zhou. Upper limits on dark matter annihilation cross sections from the first AMS-02 antiproton data. *Phys. Rev.*, D92(5):055027, 2015. doi: 10.1103/PhysRevD.92.055027.

[117] Dan Hooper, Tim Linden, and Philipp Mertsch. What Does The PAMELA Antiproton Spectrum Tell Us About Dark Matter? *JCAP*, 1503(03):021, 2015. doi: 10.1088/1475-7516/2015/03/021.

[118] Timothy Cohen, Mariangela Lisanti, Aaron Pierce, and Tracy R. Slatyer. Wino Dark Matter Under Siege. *JCAP*, 1310:061, 2013. doi: 10.1088/1475-7516/2013/10/061.

[119] JiJi Fan and Matthew Reece. In Wino Veritas? Indirect Searches Shed Light on Neutralino Dark Matter. *JHEP*, 10:124, 2013. doi: 10.1007/JHEP10(2013)124.

[120] Thomas Appelquist, Hsin-Chia Cheng, and Bogdan A. Dobrescu. Bounds on universal extra dimensions. *Phys. Rev.*, D64:035002, 2001. doi: 10.1103/PhysRevD.64.035002.

[121] Ignatios Antoniadis. A Possible new dimension at a few TeV. *Phys. Lett.*, B246:377–384, 1990. doi: 10.1016/0370-2693(90)90617-F.

[122] Howard Georgi, Aaron K. Grant, and Girma Hailu. Chiral fermions, orbifolds, scalars and fat branes. *Phys. Rev.*, D63:064027, 2001. doi: 10.1103/PhysRevD.63.064027.

[123] Hsin-Chia Cheng, Konstantin T. Matchev, and Martin Schmaltz. Radiative corrections to Kaluza-Klein masses. *Phys. Rev.*, D66:036005, 2002. doi: 10.1103/PhysRevD.66.036005.

[124] Hsin-Chia Cheng, Konstantin T. Matchev, and Martin Schmaltz. Bosonic supersymmetry? Getting fooled at the CERN LHC. *Phys. Rev.*, D66:056006, 2002. doi: 10.1103/PhysRevD.66.056006.

[125] AseshKrishna Datta, Kyoungchul Kong, and Konstantin T. Matchev. Minimal Universal Extra Dimensions in CalcHEP/CompHEP. *New J. Phys.*, 12:075017, 2010. doi: 10.1088/1367-2630/12/7/075017.

[126] AseshKrishna Datta, Kyoungchul Kong, and Konstantin T. Matchev. Discrimination of supersymmetry and universal extra dimensions at hadron colliders. *Phys. Rev.*, D72:096006, 2005. doi: 10.1103/PhysRevD.72.096006,10.1103/PhysRevD.72.119901. [Erratum: Phys. Rev.D72,119901(2005)].

[127] Dan Hooper and Stefano Profumo. Dark matter and collider phenomenology of universal extra dimensions. *Phys. Rept.*, 453:29–115, 2007. doi: 10.1016/j.physrep.2007.09.003.

[128] Geraldine Servant. Status Report on Universal Extra Dimensions After LHC8. *Mod. Phys. Lett.*, A30(15):1540011, 2015. doi: 10.1142/S0217732315400118.

[129] Georges Aad et al. Search for squarks and gluinos in events with isolated leptons, jets and missing transverse momentum at $\sqrt{s} = 8$ TeV with the ATLAS detector. *JHEP*, 04:116, 2015. doi: 10.1007/JHEP04(2015)116.

[130] Nicolas Deutschmann, Thomas Flacke, and Jong Soo Kim. Current LHC Constraints on Minimal Universal Extra Dimensions. 2017.

[131] Jyotiranjan Beuria, AseshKrishna Datta, Dipsikha Debnath, and Konstantin T. Matchev. LHC Collider Phenomenology of Minimal Universal Extra Dimensions. 2017.

[132] Gianfranco Bertone, Kyoungchul Kong, Roberto Ruiz de Austri, and Roberto Trotta. Global fits of the Minimal Universal Extra Dimensions scenario. *Phys. Rev.*, D83:036008, 2011. doi: 10.1103/PhysRevD.83.036008.

[133] Fiona Burnell and Graham D. Kribs. The Abundance of Kaluza-Klein dark matter with coannihilation. *Phys. Rev.*, D73:015001, 2006. doi: 10.1103/PhysRevD.73.015001.

[134] Mitsuru Kakizaki, Shigeki Matsumoto, and Masato Senami. Relic abundance of dark matter in the minimal universal extra dimension model. *Phys. Rev.*, D74:023504, 2006. doi: 10.1103/PhysRevD.74.023504.

[135] G. Belanger, M. Kakizaki, and A. Pukhov. Dark matter in UED: The Role of the second KK level. *JCAP*, 1102:009, 2011. doi: 10.1088/1475-7516/2011/02/009.

[136] Seong Chan Park and Jing Shu. Split Universal Extra Dimensions and Dark Matter. *Phys. Rev.*, D79:091702, 2009. doi: 10.1103/PhysRevD.79.091702.

[137] Chuan-Ren Chen, Mihoko M. Nojiri, Seong Chan Park, Jing Shu, and Michihisa Takeuchi. Dark matter and collider phenomenology of split-UED. *JHEP*, 09:078, 2009. doi: 10.1088/1126-6708/2009/09/078.

[138] Kyoungchul Kong, Seong Chan Park, and Thomas G. Rizzo. A vector-like fourth generation with a discrete symmetry from Split-UED. *JHEP*, 07:059, 2010. doi: 10.1007/JHEP07(2010)059.

[139] Csaba Csaki, Johannes Heinonen, Jay Hubisz, Seong Chan Park, and Jing Shu. 5D UED: Flat and Flavorless. *JHEP*, 01:089, 2011. doi: 10.1007/JHEP01(2011)089.

[140] DongHee Kim, Youngdo Oh, and Seong Chan Park. W' at the LHC with $\sqrt{s}$ = 14 TeV: Split universal extra dimension model. *J. Korean Phys. Soc.*, 67:1137–1141, 2015. doi: 10.3938/jkps.67.1137.

[141] Thomas Flacke and Christian Pasold. Constraints on split-UED from Electroweak Precision Tests. *Phys. Rev.*, D85:126007, 2012. doi: 10.1103/PhysRevD.85.126007.

[142] G. R. Dvali, Gregory Gabadadze, Marko Kolanovic, and F. Nitti. The Power of brane induced gravity. *Phys. Rev.*, D64:084004, 2001. doi: 10.1103/PhysRevD.64.084004.

[143] Marcela Carena, Timothy M. P. Tait, and C. E. M. Wagner. Branes and orbifolds are opaque. *Acta Phys. Polon.*, B33:2355, 2002.

[144] Francisco del Aguila, Manuel Perez-Victoria, and Jose Santiago. Effective description of brane terms in extra dimensions. *JHEP*, 10:056, 2006. doi: 10.1088/1126-6708/2006/10/056.

[145] Yu Gao, Kyoungchul Kong, and Danny Marfatia. AMS-02 and Next-to-Minimal Universal Extra Dimensions. *Phys. Lett.*, B732:269–272, 2014. doi: 10.1016/j.physletb.2014.03.060.

[146] Thomas Flacke, A. Menon, and Daniel J. Phalen. Non-minimal universal extra dimensions. *Phys. Rev.*, D79:056009, 2009. doi: 10.1103/PhysRevD.79.056009.

[147] AseshKrishna Datta, Kenji Nishiwaki, and Saurabh Niyogi. Non-minimal Universal Extra Dimensions: The Strongly Interacting Sector at the Large Hadron Collider. *JHEP*, 11:154, 2012. doi: 10.1007/JHEP11(2012)154.

[148] Ujjal Kumar Dey and Tirtha Sankar Ray. Constraining minimal and nonminimal universal extra dimension models with Higgs couplings. *Phys. Rev.*, D88(5):056016, 2013. doi: 10.1103/PhysRevD.88.056016.

[149] Thomas Flacke, Kyoungchul Kong, and Seong Chan Park. Phenomenology of Universal Extra Dimensions with Bulk-Masses and Brane-Localized Terms. *JHEP*, 05:111, 2013. doi: 10.1007/JHEP05(2013)111.

[150] Thomas Flacke, Arjun Menon, and Zack Sullivan. Constraints on UED from W' searches. *Phys. Rev.*, D86:093006, 2012. doi: 10.1103/PhysRevD.86.093006.

[151] Thomas Flacke, Kyoungchul Kong, and Seong Chan Park. 126 GeV Higgs in Next-to-Minimal Universal Extra Dimensions. *Phys. Lett.*, B728:262–267, 2014. doi: 10.1016/j.physletb.2013.11.046.

[152] Thomas Flacke, Kyoungchul Kong, and Seong Chan Park. A Review on Non-Minimal Universal Extra Dimensions. *Mod. Phys. Lett.*, A30(05):1530003, 2015. doi: 10.1142/S0217732315300037.

[153] Yoshiaki Ishigure, Mitsuru Kakizaki, and Akiteru Santa. Thermal relic abundance of the lightest Kaluza-Klein particle in phenomenological universal extra dimension models. 2016.

[154] Sebastian Arrenberg, Laura Baudis, Kyoungchul Kong, Konstantin T. Matchev, and Jonghee Yoo. Kaluza-Klein Dark Matter: Direct Detection vis-a-vis LHC. *Phys. Rev.*, D78:056002, 2008. doi: 10.1103/PhysRevD.78.056002.

[155] Sebastian Arrenberg, Laura Baudis, Kyoungchul Kong, Konstantin T. Matchev, and Jonghee Yoo. Kaluza-Klein Dark Matter: Direct Detection vis-a-vis LHC (2013 update). 2013.

[156] Thomas Flacke, Arjun Menon, Dan Hooper, and Katherine Freese. Kaluza-Klein Dark Matter And Neutrinos From Annihilation In The Sun. 2009.

[157] Anindya Datta, Ujjal Kumar Dey, Amitava Raychaudhuri, and Avirup Shaw. Boundary Localized Terms in Universal Extra-Dimensional Models through a Dark Matter perspective. *Phys. Rev.*, D88:016011, 2013. doi: 10.1103/PhysRevD.88.016011.

[158] Bogdan A. Dobrescu and Eduardo Ponton. Chiral compactification on a square. *JHEP*, 03:071, 2004. doi: 10.1088/1126-6708/2004/03/071.

[159] Nobuhito Maru, Takaaki Nomura, Joe Sato, and Masato Yamanaka. The Universal Extra Dimensional Model with S**2/Z(2) extra-space. *Nucl. Phys.*, B830:414–433, 2010. doi: 10.1016/j.nuclphysb.2009.11.023.

[160] Giacomo Cacciapaglia, Aldo Deandrea, and Jeremie Llodra-Perez. A Dark Matter candidate from Lorentz Invariance in 6D. *JHEP*, 03:083, 2010. doi: 10.1007/JHEP03(2010)083.

[161] Alexandre Arbey, Giacomo Cacciapaglia, Aldo Deandrea, and Bogna Kubik. Dark Matter in a twisted bottle. *JHEP*, 01:147, 2013. doi: 10.1007/JHEP01(2013)147.

[162] Giacomo Cacciapaglia, Aldo Deandrea, and Nicolas Deutschmann. Dark matter and localised fermions from spherical orbifolds? *JHEP*, 04:083, 2016. doi: 10.1007/JHEP04(2016)083.

[163] David Andriot, Giacomo Cacciapaglia, Aldo Deandrea, Nicolas Deutschmann, and Dimitrios Tsimpis. Towards Kaluza-Klein Dark Matter on Nilmanifolds. *JHEP*, 06:169, 2016. doi: 10.1007/JHEP06(2016)169.

[164] Bogdan A. Dobrescu, Kyoungchul Kong, and Rakhi Mahbubani. Leptons and photons at the LHC: Cascades through spinless adjoints. *JHEP*, 07:006, 2007. doi: 10.1088/1126-6708/2007/07/006.

[165] Anindya Datta, Ujjal Kumar Dey, Avirup Shaw, and Amitava Raychaudhuri. Universal Extra-Dimensional Models with Boundary Localized Kinetic Terms: Probing at the LHC. *Phys. Rev.*, D87(7):076002, 2013. doi: 10.1103/PhysRevD.87.076002.

[166] Anindya Datta, Amitava Raychaudhuri, and Avirup Shaw. LHC limits on KK-parity non-conservation in the strong sector of universal extra-dimension models. *Phys. Lett.*, B730:42–49, 2014. doi: 10.1016/j.physletb.2014.01.027.

[167] Avirup Shaw. KK-parity non-conservation in UED confronts LHC data. *Eur. Phys. J.*, C75(1):33, 2015. doi: 10.1140/epjc/s10052-014-3245-0.

[168] Thomas Appelquist and Ho-Ung Yee. Universal extra dimensions and the Higgs boson mass. *Phys. Rev.*, D67:055002, 2003. doi: 10.1103/PhysRevD.67.055002.

[169] Ilia Gogoladze and Cosmin Macesanu. Precision electroweak constraints on Universal Extra Dimensions revisited. *Phys. Rev.*, D74:093012, 2006. doi: 10.1103/PhysRevD.74.093012.

[170] M. Baak, M. Goebel, J. Haller, A. Hoecker, D. Ludwig, K. Moenig, M. Schott, and J. Stelzer. Updated Status of the Global Electroweak Fit and Constraints on New Physics. *Eur. Phys. J.*, C72:2003, 2012. doi: 10.1140/epjc/s10052-012-2003-4.

[171] Gi-Chol Cho, Kaoru Hagiwara, and Seiji Matsumoto. Constraints on four Fermi contact interactions from low-energy electroweak experiments. *Eur. Phys. J.*, C5:155–165, 1998. doi: 10.1007/s100529800824,10.1007/s100520050257.

[172] C. Patrignani et al. Review of Particle Physics. *Chin. Phys.*, C40(10):100001, 2016. doi: 10.1088/1674-1137/40/10/100001.

[173] Gui-Yu Huang, Kyoungchul Kong, and Seong Chan Park. Bounds on the Fermion-Bulk Masses in Models with Universal Extra Dimensions. *JHEP*, 06:099, 2012. doi: 10.1007/JHEP06(2012)099.

[174] The ATLAS collaboration. Search for new high-mass resonances in the dilepton final state using proton-proton collisions at $\sqrt{s}$ = 13 TeV with the ATLAS detector. 2016.

[175] CMS Collaboration. Search for a high-mass resonance decaying into a dilepton final state in 13 fb^{-1} of pp collisions at $\sqrt{s} = 13$ TeV. 2016.

[176] P. A. R. Ade et al. Planck 2013 results. XVI. Cosmological parameters. *Astron. Astrophys.*, 571:A16, 2014. doi: 10.1051/0004-6361/201321591.

[177] Mihailo Backovic, Antony Martini, Olivier Mattelaer, Kyoungchul Kong, and Gopolang Mohlabeng. Direct Detection of Dark Matter with MadDM v.2.0. *Phys. Dark Univ.*, 9-10:37–50, 2015. doi: 10.1016/j.dark.2015.09.001.

[178] Geraldine Servant and Timothy M. P. Tait. Elastic scattering and direct detection of Kaluza-Klein dark matter. *New J. Phys.*, 4:99, 2002. doi: 10.1088/1367-2630/4/1/399.

[179] Lars Bergstrom, Torsten Bringmann, Martin Eriksson, and Michael Gustafsson. Two photon annihilation of Kaluza-Klein dark matter. *JCAP*, 0504:004, 2005. doi: 10.1088/1475-7516/2005/04/004.

[180] Gianfranco Bertone, C. B. Jackson, Gabe Shaughnessy, Tim M. P. Tait, and Alberto Vallinotto. Gamma Ray Lines from a Universal Extra Dimension. *JCAP*, 1203:020, 2012. doi: 10.1088/1475-7516/2012/03/020.

[181] Johan Bonnevier, Henrik Melbeus, Alexander Merle, and Tommy Ohlsson. Monoenergetic Gamma-Rays from Non-Minimal Kaluza-Klein Dark Matter Annihilations. *Phys. Rev.*, D85:043524, 2012. doi: 10.1103/PhysRevD.85.109902,10.1103/PhysRevD.85.043524. [Erratum: Phys. Rev.D85,109902(2012)].

[182] Henrik Melbeus, Alexander Merle, and Tommy Ohlsson. Continuum photon spectrum from Z^1Z^1 annihilations in universal extra dimensions. *Phys. Lett.*, B706:329–332, 2012. doi: 10.1016/j.physletb.2012.05.059,10.1016/j.physletb.2011.11.018. [Erratum: Phys. Lett.B713,350(2012)].

[183] B. Moore. Evidence against dissipationless dark matter from observations of galaxy haloes. *Nature*, 370:629, 1994. doi: 10.1038/370629a0.

[184] Matthew G. Walker and Jorge Penarrubia. A Method for Measuring (Slopes of) the Mass Profiles of Dwarf Spheroidal Galaxies. *Astrophys. J.*, 742:20, 2011. doi: 10.1088/0004-637X/742/1/20.

[185] Michael Boylan-Kolchin, James S. Bullock, and Manoj Kaplinghat. Too big to fail? The puzzling darkness of massive Milky Way subhaloes. *Mon. Not. Roy. Astron. Soc.*, 415:L40, 2011. doi: 10.1111/j.1745-3933.2011.01074.x.

[186] Mark R. Lovell, Carlos S. Frenk, Vincent R. Eke, Adrian Jenkins, Liang Gao, and Tom Theuns. The properties of warm dark matter haloes. *Mon. Not. Roy. Astron. Soc.*, 439:300–317, 2014. doi: 10.1093/mnras/stt2431.

[187] David N. Spergel and Paul J. Steinhardt. Observational evidence for selfinteracting cold dark matter. *Phys. Rev. Lett.*, 84:3760–3763, 2000. doi: 10.1103/PhysRevLett.84.3760.

[188] Miguel Rocha, Annika H. G. Peter, James S. Bullock, Manoj Kaplinghat, Shea Garrison-Kimmel, Jose Onorbe, and Leonidas A. Moustakas. Cosmological Simulations with Self-Interacting Dark Matter I: Constant Density Cores and Substructure. *Mon. Not. Roy. Astron. Soc.*, 430:81–104, 2013. doi: 10.1093/mnras/sts514.

[189] Scott W. Randall, Maxim Markevitch, Douglas Clowe, Anthony H. Gonzalez, and Marusa Bradac. Constraints on the Self-Interaction Cross-Section of Dark Matter from Numerical Simulations of the Merging Galaxy Cluster 1E 0657-56. *Astrophys. J.*, 679:1173–1180, 2008. doi: 10.1086/587859.

[190] Jesus Zavala, Mark Vogelsberger, and Matthew G. Walker. Constraining Self-Interacting Dark Matter with the Milky Way's dwarf spheroidals. *Monthly Notices of the Royal Astronomical Society: Letters*, 431:L20–L24, 2013. doi: 10.1093/mnrasl/sls053.

[191] Francesco D'Eramo and Jesse Thaler. Semi-annihilation of Dark Matter. *JHEP*, 06:109, 2010. doi: 10.1007/JHEP06(2010)109.

[192] Genevieve Belanger, Kristjan Kannike, Alexander Pukhov, and Martti Raidal. Impact of semi-annihilations on dark matter phenomenology - an example of Z_N symmetric scalar dark matter. *JCAP*, 1204:010, 2012. doi: 10.1088/1475-7516/2012/04/010.

[193] Junwu Huang and Yue Zhao. Dark Matter Induced Nucleon Decay: Model and Signatures. *JHEP*, 02:077, 2014. doi: 10.1007/JHEP02(2014)077.

[194] Kaustubh Agashe, Yanou Cui, Lina Necib, and Jesse Thaler. (In)direct Detection of Boosted Dark Matter. *JCAP*, 1410(10):062, 2014. doi: 10.1088/1475-7516/2014/10/062.

[195] Joshua Berger, Yanou Cui, and Yue Zhao. Detecting Boosted Dark Matter from the Sun with Large Volume Neutrino Detectors. *JCAP*, 1502(02):005, 2015. doi: 10.1088/1475-7516/2015/02/005.

[196] Joachim Kopp, Jia Liu, and Xiao-Ping Wang. Boosted Dark Matter in IceCube and at the Galactic Center. *JHEP*, 04:105, 2015. doi: 10.1007/JHEP04(2015)105.

[197] Atri Bhattacharya, Raj Gandhi, and Aritra Gupta. The Direct Detection of Boosted Dark Matter at High Energies and PeV events at IceCube. *JCAP*, 1503(03):027, 2015. doi: 10.1088/1475-7516/2015/03/027.

[198] Lina Necib, Jarrett Moon, Taritree Wongjirad, and Janet M. Conrad. Boosted Dark Matter at Neutrino Experiments. *Phys. Rev.*, D95(7):075018, 2017. doi: 10.1103/PhysRevD.95.075018.

[199] L. B. Okun. LIMITS OF ELECTRODYNAMICS: PARAPHOTONS? *Sov. Phys. JETP*, 56:502, 1982. [Zh. Eksp. Teor. Fiz.83,892(1982)].

[200] Eung Jin Chun, Jong-Chul Park, and Stefano Scopel. Dark matter and a new gauge boson through kinetic mixing. *JHEP*, 02:100, 2011. doi: 10.1007/JHEP02(2011)100.

[201] Rouven Essig et al. Working Group Report: New Light Weakly Coupled Particles. In *Proceedings, Community Summer Study 2013: Snowmass on the Mississippi (CSS2013): Minneapolis, MN, USA, July 29-August 6, 2013*, 2013. URL https://inspirehep.net/record/1263039/files/arXiv:1311.0029.pdf.

[202] Philip Ilten, Yotam Soreq, Jesse Thaler, Mike Williams, and Wei Xue. Proposed Inclusive Dark Photon Search at LHCb. *Phys. Rev. Lett.*, 116(25):251803, 2016. doi: 10.1103/PhysRevLett.116.251803.

[203] J. R. Batley et al. Search for the dark photon in π^0 decays. *Phys. Lett.*, B746:178–185, 2015. doi: 10.1016/j.physletb.2015.04.068.

[204] Philip Ilten, Jesse Thaler, Mike Williams, and Wei Xue. Dark photons from charm mesons at LHCb. *Phys. Rev.*, D92(11):115017, 2015. doi: 10.1103/PhysRevD.92.115017.

[205] A. Anastasi et al. Limit on the production of a new vector boson in $e^+e^- \to U\gamma$, $U \to \pi^+\pi^-$ with the KLOE experiment. *Phys. Lett.*, B757:356–361, 2016. doi: 10.1016/j.physletb.2016.04.019.

[206] D. Banerjee et al. Search for invisible decays of sub-GeV dark photons in missing-energy events at the CERN SPS. *Phys. Rev. Lett.*, 118(1):011802, 2017. doi: 10.1103/PhysRevLett.118.011802.

[207] Priyotosh Bandyopadhyay, Eung Jin Chun, and Jong-Chul Park. Right-handed sneutrino dark matter in $\mathbf{U}(\mathbf{1})'$ seesaw models and its signatures at the LHC. *JHEP*, 06:129, 2011. doi: 10.1007/JHEP06(2011)129.

[208] M. Fechner et al. Kinematic reconstruction of atmospheric neutrino events in a large water Cherenkov detector with proton identification. *Phys. Rev.*, D79:112010, 2009. doi: 10.1103/PhysRevD.79.112010.

[209] E. Kearns et al. Hyper-Kamiokande Physics Opportunities. In *Proceedings, Community Summer Study 2013: Snowmass on the Mississippi (CSS2013): Minneapolis, MN, USA, July 29-August 6, 2013*, 2013. URL https://inspirehep.net/record/1252067/files/arXiv:1309.0184.pdf.

[210] R. Acciarri et al. Long-Baseline Neutrino Facility (LBNF) and Deep Underground Neutrino Experiment (DUNE). 2015.

[211] M. G. Aartsen et al. Letter of Intent: The Precision IceCube Next Generation Upgrade (PINGU). 2014.

[212] R. Acciarri et al. Long-Baseline Neutrino Facility (LBNF) and Deep Underground Neutrino Experiment (DUNE). 2016.

[213] R. Acciarri et al. Long-Baseline Neutrino Facility (LBNF) and Deep Underground Neutrino Experiment (DUNE). 2016.

[214] James Strait et al. Long-Baseline Neutrino Facility (LBNF) and Deep Underground Neutrino Experiment (DUNE). 2016.

[215] T. K. Gaisser and M. Honda. Flux of atmospheric neutrinos. *Ann. Rev. Nucl. Part. Sci.*, 52:153–199, 2002. doi: 10.1146/annurev.nucl.52.050102.090645.

[216] K. Bays et al. Supernova Relic Neutrino Search at Super-Kamiokande. *Phys. Rev.*, D85:052007, 2012. doi: 10.1103/PhysRevD.85.052007.

[217] K. Abe et al. Solar neutrino results in Super-Kamiokande-III. *Phys. Rev.*, D83:052010, 2011. doi: 10.1103/PhysRevD.83.052010.

[218] Lee Ka Pik. *Study of the neutrino mass hierarchy with the atmospheric neutrino data observed in Super-Kamiokande*. PhD thesis, Tokyo U., 2012. URL `http://www-sk.icrr.u-tokyo.ac.jp/sk/pub/index.html#dthesis`.

[219] Michael R. Dziomba. *A Study of neutrino Oscillation Models with Super-Kamiokande Atmospheric Neutrino Data*. PhD thesis, Washington U., Seattle, 2012. URL `http://www-sk.icrr.u-tokyo.ac.jp/sk/pub/index.html#dthesis`.

[220] E. Richard et al. Measurements of the atmospheric neutrino flux by Super-Kamiokande: energy spectra, geomagnetic effects, and solar modulation. *Phys. Rev.*, D94(5):052001, 2016. doi: 10.1103/PhysRevD.94.052001.

[221] K. Abe et al. Physics Potentials with the Second Hyper-Kamiokande Detector in Korea. 2016.

[222] Julio F. Navarro, Carlos S. Frenk, and Simon D. M. White. The Structure of cold dark matter halos. *Astrophys. J.*, 462:563–575, 1996. doi: 10.1086/177173.

[223] Julio F. Navarro, Carlos S. Frenk, and Simon D. M. White. A Universal density profile from hierarchical clustering. *Astrophys. J.*, 490:493–508, 1997. doi: 10.1086/304888.

[224] Manoj Kaplinghat, Tim Linden, and Hai-Bo Yu. Galactic Center Excess in γ Rays from Annihilation of Self-Interacting Dark Matter. *Phys. Rev. Lett.*, 114(21):211303, 2015. doi: 10.1103/PhysRevLett.114.211303.

[225] Manoj Kaplinghat, Ryan E. Keeley, Tim Linden, and Hai-Bo Yu. Tying Dark Matter to Baryons with Self-interactions. *Phys. Rev. Lett.*, 113:021302, 2014. doi: 10.1103/PhysRevLett.113.021302.

[226] Manoj Kaplinghat, Sean Tulin, and Hai-Bo Yu. Dark Matter Halos as Particle Colliders: Unified Solution to Small-Scale Structure Puzzles from Dwarfs to Clusters. *Phys. Rev. Lett.*, 116(4):041302, 2016. doi: 10.1103/PhysRevLett.116.041302.

[227] Jeong Han Kim, Kyoungchul Kong, Seung J. Lee, and Gopolang Mohlabeng. Probing TeV scale Top-Philic Resonances with Boosted Top-Tagging at the High Luminosity LHC. *Phys. Rev.*, D94(3):035023, 2016. doi: 10.1103/PhysRevD.94.035023.

[228] J. R. T. de Mello Neto et al. The DAMIC dark matter experiment. *PoS*, ICRC2015:1221, 2016.

[229] Rouven Essig, Jeremy Mardon, and Tomer Volansky. Direct Detection of Sub-GeV Dark Matter. *Phys. Rev.*, D85:076007, 2012. doi: 10.1103/PhysRevD.85.076007.

[230] Rouven Essig, Aaron Manalaysay, Jeremy Mardon, Peter Sorensen, and Tomer Volansky. First Direct Detection Limits on sub-GeV Dark Matter from XENON10. *Phys. Rev. Lett.*, 109:021301, 2012. doi: 10.1103/PhysRevLett.109.021301.

[231] G. Steigman, C. L. Sarazin, H. Quintana, and J. Faulkner. Dynamical interactions and astrophysical effects of stable heavy neutrinos. *Astron. J.*, 83:1050–1061, 1978. doi: 10.1086/112290.

[232] K. Griest and D. Seckel. Cosmic Asymmetry, Neutrinos and the Sun. *Nucl. Phys.*, B283:681–705, 1987. doi: 10.1016/0550-3213(87)90293-8,10.1016/0550-3213(88)90409-9. [Erratum: Nucl. Phys.B296,1034(1988)].

[233] Andrew Gould. WIMP Distribution in and Evaporation From the Sun. *Astrophys. J.*, 321:560, 1987. doi: 10.1086/165652.

[234] Giorgio Busoni, Andrea De Simone, and Wei-Chih Huang. On the Minimum Dark Matter Mass Testable by Neutrinos from the Sun. *JCAP*, 1307:010, 2013. doi: 10.1088/1475-7516/2013/07/010.

[235] Andrew R. Zentner. High-Energy Neutrinos From Dark Matter Particle Self-Capture Within the Sun. *Phys. Rev.*, D80:063501, 2009. doi: 10.1103/PhysRevD.80.063501.

[236] Ivone F. M. Albuquerque, Carlos Perez de Los Heros, and Denis S. Robertson. Constraints on self interacting dark matter from IceCube results. *JCAP*, 1402:047, 2014. doi: 10.1088/1475-7516/2014/02/047.

[237] Chian-Shu Chen, Fei-Fan Lee, Guey-Lin Lin, and Yen-Hsun Lin. Probing Dark Matter Self-Interaction in the Sun with IceCube-PINGU. *JCAP*, 1410(10):049, 2014. doi: 10.1088/1475-7516/2014/10/049.

[238] http://www.sns.ias.edu/∼jnb/SNdata/sndata.html. http://www.sns.ias.edu/∼jnb/sndata/sndata.html. for solar data.

[239] Rolf Kappl and Martin Wolfgang Winkler. New Limits on Dark Matter from Super-Kamiokande. *Nucl. Phys.*, B850:505–521, 2011. doi: 10.1016/j.nuclphysb.2011.05.006.

[240] Pietro Baratella, Marco Cirelli, Andi Hektor, Joosep Pata, Morten Piibeleht, and Alessandro Strumia. PPPC 4 DMν: a Poor Particle Physicist Cookbook for Neutrinos from Dark Matter annihilations in the Sun. *JCAP*, 1403:053, 2014. doi: 10.1088/1475-7516/2014/03/053.

[241] Andrew Gould. Cosmological density of WIMPs from solar and terrestrial annihilations. *Astrophys. J.*, 388:338–344, 1992. doi: 10.1086/171156.

[242] K. A. Olive et al. Review of Particle Physics. *Chin. Phys.*, C38:090001, 2014. doi: 10.1088/1674-1137/38/9/090001.

[243] Andrew Gould. Resonant Enhancements in WIMP Capture by the Earth. *Astrophys. J.*, 321:571, 1987. doi: 10.1086/165653.

[244] Anthony DiFranzo, Patrick J. Fox, and Tim M. P. Tait. Vector Dark Matter through a Radiative Higgs Portal. *JHEP*, 04:135, 2016. doi: 10.1007/JHEP04(2016)135.

[245] Thomas Hambye. Hidden vector dark matter. *JHEP*, 01:028, 2009. doi: 10.1088/1126-6708/2009/01/028.

[246] Yasaman Farzan and Amin Rezaei Akbarieh. VDM: A model for Vector Dark Matter. *JCAP*, 1210:026, 2012. doi: 10.1088/1475-7516/2012/10/026.

[247] Seungwon Baek, P. Ko, Wan-Il Park, and Eibun Senaha. Higgs Portal Vector Dark Matter : Revisited. *JHEP*, 05:036, 2013. doi: 10.1007/JHEP05(2013)036.

[248] Seungwon Baek, P. Ko, and Wan-Il Park. Singlet Portal Extensions of the Standard Seesaw Models to a Dark Sector with Local Dark Symmetry. *JHEP*, 07:013, 2013. doi: 10.1007/JHEP07(2013)013.

[249] Seungwon Baek, P. Ko, and Wan-Il Park. Invisible Higgs Decay Width vs. Dark Matter Direct Detection Cross Section in Higgs Portal Dark Matter Models. *Phys.Rev.*, D90(5):055014, 2014. doi: 10.1103/PhysRevD.90.055014.

[250] Seungwon Baek, P. Ko, Wan-Il Park, and Yong Tang. Indirect and direct signatures of Higgs portal decaying vector dark matter for positron excess in cosmic rays. *JCAP*, 1406:046, 2014. doi: 10.1088/1475-7516/2014/06/046.

[251] P. Ko, Wan-Il Park, and Yong Tang. Higgs portal vector dark matter for GeV scale γ-ray excess from galactic center. *JCAP*, 1409:013, 2014. doi: 10.1088/1475-7516/2014/09/013.

[252] Christian Gross, Oleg Lebedev, and Yann Mambrini. Non-Abelian gauge fields as dark matter. *JHEP*, 08:158, 2015. doi: 10.1007/JHEP08(2015)158.

[253] Stefano Di Chiara and Kimmo Tuominen. A minimal model for SU(N) vector dark matter. *JHEP*, 11:188, 2015. doi: 10.1007/JHEP11(2015)188.

[254] Chuan-Hung Chen and Takaaki Nomura. Searching for vector dark matter via Higgs portal at the LHC. *Phys. Rev.*, D93(7):074019, 2016. doi: 10.1103/PhysRevD.93.074019.

[255] Jong Soo Kim, Oleg Lebedev, and Daniel Schmeier. Higgsophilic gauge bosons and monojets at the LHC. *JHEP*, 11:128, 2015. doi: 10.1007/JHEP11(2015)128.

[256] W. H. Furry. A Symmetry Theorem in the Positron Theory. *Phys. Rev.*, 51:125–129, 1937. doi: 10.1103/PhysRev.51.125.

[257] P. Gondolo, J. Edsjo, P. Ullio, L. Bergstrom, Mia Schelke, and E. A. Baltz. DarkSUSY: Computing supersymmetric dark matter properties numerically. *JCAP*, 0407:008, 2004. doi: 10.1088/1475-7516/2004/07/008.

[258] Keith R. Dienes, Jason Kumar, and Brooks Thomas. Direct Detection of Dynamical Dark Matter. *Phys. Rev.*, D86:055016, 2012. doi: 10.1103/PhysRevD.86.055016.

[259] Georges Aad et al. Constraints on new phenomena via Higgs boson couplings and invisible decays with the ATLAS detector. *JHEP*, 11:206, 2015. doi: 10.1007/JHEP11(2015)206.

[260] S. Schael et al. Precision electroweak measurements on the *Z* resonance. *Phys. Rept.*, 427: 257–454, 2006. doi: 10.1016/j.physrep.2005.12.006.

[261] Aria Basirnia, Sebastian Macaluso, and David Shih. Dark Matter and the Higgs in Natural SUSY. *JHEP*, 03:073, 2017. doi: 10.1007/JHEP03(2017)073.

[262] Adam Alloul, Neil D. Christensen, Celine Degrande, Claude Duhr, and Benjamin Fuks. FeynRules 2.0 - A complete toolbox for tree-level phenomenology. *Comput. Phys. Commun.*, 185: 2250–2300, 2014. doi: 10.1016/j.cpc.2014.04.012.

[263] G. Belanger, F. Boudjema, A. Pukhov, and A. Semenov. micrOMEGAs 3: A program for calculating dark matter observables. *Comput. Phys. Commun.*, 185:960–985, 2014. doi: 10.1016/j.cpc.2013.10.016.

[264] Alexander Belyaev, Neil D. Christensen, and Alexander Pukhov. CalcHEP 3.4 for collider physics within and beyond the Standard Model. *Comput.Phys.Commun.*, 184:1729–1769, 2013. doi: 10.1016/j.cpc.2013.01.014.

[265] J. Alwall, R. Frederix, S. Frixione, V. Hirschi, F. Maltoni, O. Mattelaer, H. S. Shao, T. Stelzer, P. Torrielli, and M. Zaro. The automated computation of tree-level and next-to-leading order differential cross sections, and their matching to parton shower simulations. *JHEP*, 07:079, 2014. doi: 10.1007/JHEP07(2014)079.

[266] Thomas Hahn. Generating Feynman diagrams and amplitudes with FeynArts 3. *Comput. Phys. Commun.*, 140:418–431, 2001. doi: 10.1016/S0010-4655(01)00290-9.

[267] Thomas Hahn. Feynman Diagram Calculations with FeynArts, FormCalc, and LoopTools. *PoS*, ACAT2010:078, 2010.

[268] T. Hahn and M. Perez-Victoria. Automatized one loop calculations in four-dimensions and D-dimensions. *Comput. Phys. Commun.*, 118:153–165, 1999. doi: 10.1016/S0010-4655(98)00173-8.